Space Sci Rev (2011) 162:113–171
DOI 10.1007/s11214-011-9845-1

The Induced Magnetospheres of Mars, Venus, and Titan

C. Bertucci · F. Duru · N. Edberg · M. Fraenz · C. Martinecz · K. Szego · O. Vaisberg

Received: 2 March 2011 / Accepted: 22 September 2011 / Published online: 26 November 2011

Abstract This article summarizes and aims at comparing the main features of the induced magnetospheres of Mars, Venus and Titan. All three objects form a well-defined induced magnetosphere (IM) and magnetotail as a consequence of the interaction of an external wind of plasma with the ionosphere and the exosphere of these objects. In all three, photoionization seems to be the most important ionization process. In all three, the IM displays a clear outer boundary characterized by an enhancement of magnetic field draping and massloading, along with a change in the plasma composition, a decrease in the plasma temperature, a deflection of the external flow, and, at least for Mars and Titan, an increase of the total density. Also, their magnetotail geometries follow the orientation of the upstream magnetic field and flow velocity under quasi-steady conditions. Exceptions to this are fossil fields observed at Titan and the near Mars regions where crustal fields dominate the magnetic topology. Magnetotails also concentrate the escaping plasma flux from these three objects and similar acceleration mechanisms are thought to be at work. In the case of Mars and Titan, global reconfiguration of the magnetic field topology (reconnection with the crustal sources and exits into Saturn's magnetosheath, respectively) may lead to important losses of

C. Bertucci (✉)
Institute for Astronomy and Space Physics (IAFE), CONICET/UBA, Buenos Aires, Argentina
e-mail: cbertucci@iafe.uba.ar

F. Duru
Department of Astronomy, The Unversity of Iowa, Iowa City, USA

N. Edberg
Swedish Space Science Institute, Uppsala, Sweden

M. Fraenz · C. Martinecz
Max Planck Institute for Solar System Research, Klatenburg-Lindau, Germany

K. Szego
KFKI-RMKI, Budapest, Hungary

O. Vaisberg
Space Research Institute, Russian Academy of Sciences, Moscow, Russian Federation

plasma. Finally, an ionospheric boundary related to local photoelectron signals may be, in the absence of other sources of pressure (crustal fields) a signature of the ultimate boundary to the external flow.

Keywords Induced magnetospheres · Mars · Venus · Titan · Boundaries · Draping · Massloading

1 Introduction

The presence of an unmagnetized planetary body surrounded by an atmosphere in a flow of collisionless, magnetized plasma generates, via ionizing processes, a perturbation in the upstream plasma and the magnetic field. As the perturbation in the magnetic field is generated from currents induced from the differential motion between the external and the planetary particle populations, these perturbed regions are usually referred to as 'induced magnetospheres', in opposition to 'intrinsic magnetospheres' where the perturbation is originating in the planet's intrinsic magnetic field.

Mars, Venus and Titan are three distinct examples of unmagnetized objects (Acuña et al. 1998; Russell et al. 1979; Wei et al. 2011) possessing an atmosphere. In spite of the differences in their atmospheric composition, size, ionization/flow conditions, and upstream magnetic field variability, the perturbations that they generate in the surrounding plasma (solar wind, Saturn's magnetospheric plasma) display remarkable similarities, indicating that common processes operate in spite of their distinct position in the parameter space.

An induced magnetosphere is the result of the collisionless transfer of energy and momentum from the plasma flow surrounding an unmagnetized body into its induced magnetosphere and atmosphere.

The interaction can start several planetary radii away from these objects, where exospheric particles are ionized, mostly by photoionization. Photoionization adds a small amount of energy to the neutral particles and therefore these 'newborn ions' have the same temperature as their parent neutral (a few eVs). As soon as a newborn ion is formed, it becomes sensitive to the electric fields associated to the incoming flow (convective, electric fields arising from plasma microinstabilities), whose forces intend to restore the thermodynamical equilibrium, accelerating the ion. As the flow approaches the object, an increasing number of cold exospheric newborn ions are picked up in this way and lead to significant massloading which decelerates the flow in agreement with momentum conservation.

In addition to massloading, the presence of an obstacle represented by a current layer (e.g. ionopause), a collision-dominated diffusion region within the body's ionosphere, or the object itself contributes to the diversion of the flow. In regions where the collisionless regime holds, the external magnetic field frozen into the plasma piles up around the flow 'stagnation' region, and drapes around the object as the flow is diverted around the body (Alfven 1957). This defines an induced magnetic tail formed by two lobes of opposite magnetic polarity separated by a neutral sheet.

As a result, a well-defined region filled with perturbed, massloaded external plasma is formed. This region is called 'induced magnetosphere'.

The external plasma loses its momentum and energy to the local plasma both abruptly and gradually. This defines respectively the boundaries and regions within an induced magnetosphere. Several permanent, well-defined regions and boundaries emerge in most observations:

- A collisionless bow shock (BS)
- Magnetosheath
- Induced magnetospheric boundary (IMB)
- Induced magnetosphere (including magnetotail)
- Ionospheric boundary/ionopause

A boundary has to be 'thin' with respect to the regions surrounding it, a measure of its extent being given by local particle lengthscales such as local ion gyroradius or inertial length, where strong current systems, which modify the external magnetic field occur. Conversely, regions have dimensions of several of these lengthscales.

The understanding of the processes occurring in induced magnetospheres requires the characterization of the following parameters: upstream plasma (solar or planetary), local superthermal and cold populations, and magnetic field. Since the beginning of space exploration, spacecraft have measured these quantities. The measurements of these quantities, have dramatically increased in number over the last two decades, enabling not only deeper analyses of the structures at each object, but also, and for the first time, thorough inter-object comparisons.

Limitations on these comparisons will come from two main elements: first, the scarce availability of simultaneous measurements of basic plasma parameters, and second, the absence of multipoint observations. As a result, observations taken at different epochs and locations are usually used assuming steady state interactions.

The present review intends to be an initial effort in summarizing the most relevant results on the study of the induced magnetospheres of Mars, Venus and Titan and comparing their main features in order to identify common physical processes operating at these objects.

The choice of these three bodies follows the topics covered by the rest of the articles in this issue. However, observations around active comets—a special case of an induced magnetosphere entirely created and sustained by massloading—will be included in the comparison section.

Finally, it is the intention of the authors to focus on observations, as the analyses and discussion of numerical simulations are treated in the comprehensive review by Kallio et al. (this issue).

The article is structured as follows: First, a summary of the characteristics of the induced magnetospheres and related structures at Mars, Venus and Titan is given in Sects. 2, 3 and 4 respectively. These results are then discussed and compared in Sect. 5, followed by conclusions.

2 Mars

Since the very beginning of space exploration, several spacecraft visited planet Mars, revealing the properties of its plasma environment. Following the encounters by Mariner 4, 6 and 7, Mars 2, 3, and Mariner 9. Mars 2 and 3 were probably the first spacecraft to enter the Martian induced magnetosphere (Vaisberg and Bogdanov 1974) in the tail sector (i.e. plasma and magnetic tail), although at the time of those observations, the nature (i.e. intrinsic or inteplanetary) of the magnetic field observed close to the planet had not been unveiled (Dolginov et al. 1976; Russell 1978a, 1978b). This issue would not be resolved until the arrival of Mars Global Surveyor (MGS) (Albee et al. 2001), which provided in situ magnetic field measurements below the ionospheric density peak for the first time. These measurements revealed that, aside from the crustal sources of remnant magnetization, there was no global intrinsic magnetic field (Acuña et al. 1992).

The absence of a global intrinsic magnetic field at Mars led to the re-interpretation of part of previous plasma measurements, in particular those obtained by the Phobos-2 mission (see, e.g., special issue of Nature, 341, 1989). A comprehensive review on the comparison between MGS and Phobos-2 plasma observations within the induced magnetosphere of Mars can be found in Nagy et al. (2004). Following a ∼1.5 year phase consisting of elliptical orbits, where the induced magnetosphere was explored at different altitudes and solar zenith angles (except the subsolar region), MGS was set into a 400 km altitude, 2AM-2PM local-time circular orbit (mapping mission phase). Although the magnetic field and the superthermal (mostly solar wind) electron population were efficiently characterized by the magnetometer and electron reflectometer (MAG/ER) (Acuña et al. 1992), MGS did not carry instruments capable of measuring either cold (planetary) ions, cold (planetary) electrons, or superthermal (solar wind/planetary) ions. The MGS MAG/ER investigation comprises a magnetometer (MAG), which provides, wide range, fast (32 Hz) magnetic field vector measurements, and an electron spectrometer used as a reflectometer (ER), which measures the fluxes of electrons in the energy range 10 eV–20 keV with a maximum resolution of 2 s.

With an overlap of a few years with MGS (which stopped taking measurements in late 2006) and while it was on a circular orbit at 400 km altitude, Mars Express (MEX) (Chicarro et al. 2004; Picardi et al. 2004) began its observations around Mars in 2003 from a highly elliptical orbit (∼270 km and ∼10000 km altitude periapsis and apoapsis, respectively), providing the first comprehensive picture of solar wind, and cold and superthermal planetary particle populations around Mars. This was made possible by the ASPERA-3 instrument, which consists of an electron spectrometer (ELS) and an ion mass analyzer (IMA) (Barabash et al. 2006). ELS measures electrons in the energy range 10 eV–20 keV. IMA measures ions in the energy range 10 eV/q–30 keV/q and can resolve the masses of the main ion species (1, 2, 4, 8, 16 and 32 amu/q).

Unfortunately, MEX does not carry a magnetometer. Nevertheless, for some orbits, the magnetic field strength and the electron density within the induced magnetosphere can be deduced from the Mars Advanced Radar for Subsurface and Ionospheric Sounding (MARSIS) measurements (Gurnett et al. 2005). One capability of the ionospheric sounding mode of MARSIS onboard MEX is the measurement of the local plasma frequency in the vicinity of the spacecraft by means of the detection of local plasma oscillations. Summaries of MEX plasma results can be found in review articles by Franz et al. (2006a) and Dubinin et al. (2006a).

More recently, the Rosetta spacecraft performed a flyby around Mars (March 2007), but only the lander magnetometer (Auster et al. 2007) was on while the orbiter, with all its instruments off, flew through the Martian induced magnetosphere (e.g. Edberg et al. 2008).

Apart from the plasma waves generated by the pick up of exospheric ions, the first perturbation generated by Mars in the supermagnetosonic solar wind flow is the bow shock. This bow shock, will decelerate, heat and compress the solar wind plasma which populates the magnetosheath. The end of the turbulent regime of the magnetosheath is the induced magnetosphere boundary or IMB (referred to as the magnetic pileup boundary in Fig. 1), which precedes a region of highly draped magnetic field local plasma-dominated region: the induced magnetosphere (IM). The IMB extends out into the downstream sector where it becomes the outer boundary of the magnetic tail. The IMB has several subregions. On the dayside, the region below the IMB and above the ionospheric boundary is referred to as the magnetic pileup region (MPR). At low magnetic latitudes, the interplanetary magnetic field (IMF) within the MPR is connected to tail lobe fields. The ionospheric boundary marks the lower end of the MPR on the dayside. Usually referred to it as photoelectron boundary (PEB), this boundary is usually associated with the upper limit of the collisional ionosphere.

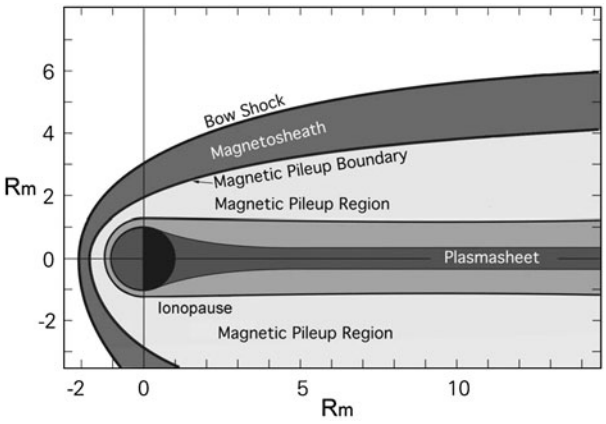

Fig. 1 Approximate locations and shapes of major plasma boundaries found around Mars according to Nagy et al. (2004)

The PEB and to a lesser extent the IMB locations are influenced by the magnetic fields from the crustal sources. In the downstream sector, a tail plasma sheet separating both tail lobes is observed. The plasma structure of the plasma sheet close to the planet is still under scrutiny with a strong effect of the crustal magnetic sources in the nightside.

2.1 The Martian Bow Shock

The most distinctive features of the Martian bow shock are its relatively small size and the signatures produced by pick up of exospheric ions (Moses et al. 1988; Dubinin et al. 1993a).

In opposition to Venus, the small size of Mars combined with a weaker IMF makes the Larmor radius of solar wind protons comparable to the size of the Martian shock, and therefore kinetic effects become important (Lembège and Savoini 2002).

In addition, the large extent of the Martian exosphere (Chaufray et al. 2008) results in the presence of pick up ions that generate low frequency waves (Brain et al. 2002; Mazelle et al. 2004; Wei and Russell 2006) well beyond the shock. These waves are convected downstream by the solar wind and interact with the shock structure, leading to a more disturbed signature.

Initial in situ plasma and magnetic field measurements established the existence of a bow shock at Mars (see e.g. Vaisberg et al. 1973; Slavin et al. 1980). In particular, Phobos-2 explored in detail the structure of the Martian shock in the terminator and post terminator regions and its substructures were investigated. These include a foot, ramp, and overshoot, whose size ranges between 0.5 and 2.5 proton gyroradii (2–8 c/ω_{pi}) and whose amplitude scales with the magnetosonic Mach number (Tatrallyay et al. 1997) as predicted for fast magnetosonic shock waves. A comprehensive review of Phobos-2 shock observations can be found in Mazelle et al. (2004).

The observations by MGS MAG/ER provided a description of the magnetic structure of the Martian shock on the dayside. Figure 2 shows a typical shock crossing by MGS (around 07:10 UT) characterized by an increase in the magnetic field magnitude and variability, followed by a compression of the plasma related to the increase in the superthermal electron fluxes. In MEX/ASPERA-3 data the BS is observed inbound as a sudden increase in fluxes of both electrons and ions in the ELS and IMA data sets.

As mentioned above, the Martian bow shock is also characterized by the presence of a strong wave activity regardless of shock angle. Figure 3 shows MGS MAG profiles of the magnetic field strength for a quasi-perpendicular crossing (top), an intermediate case,

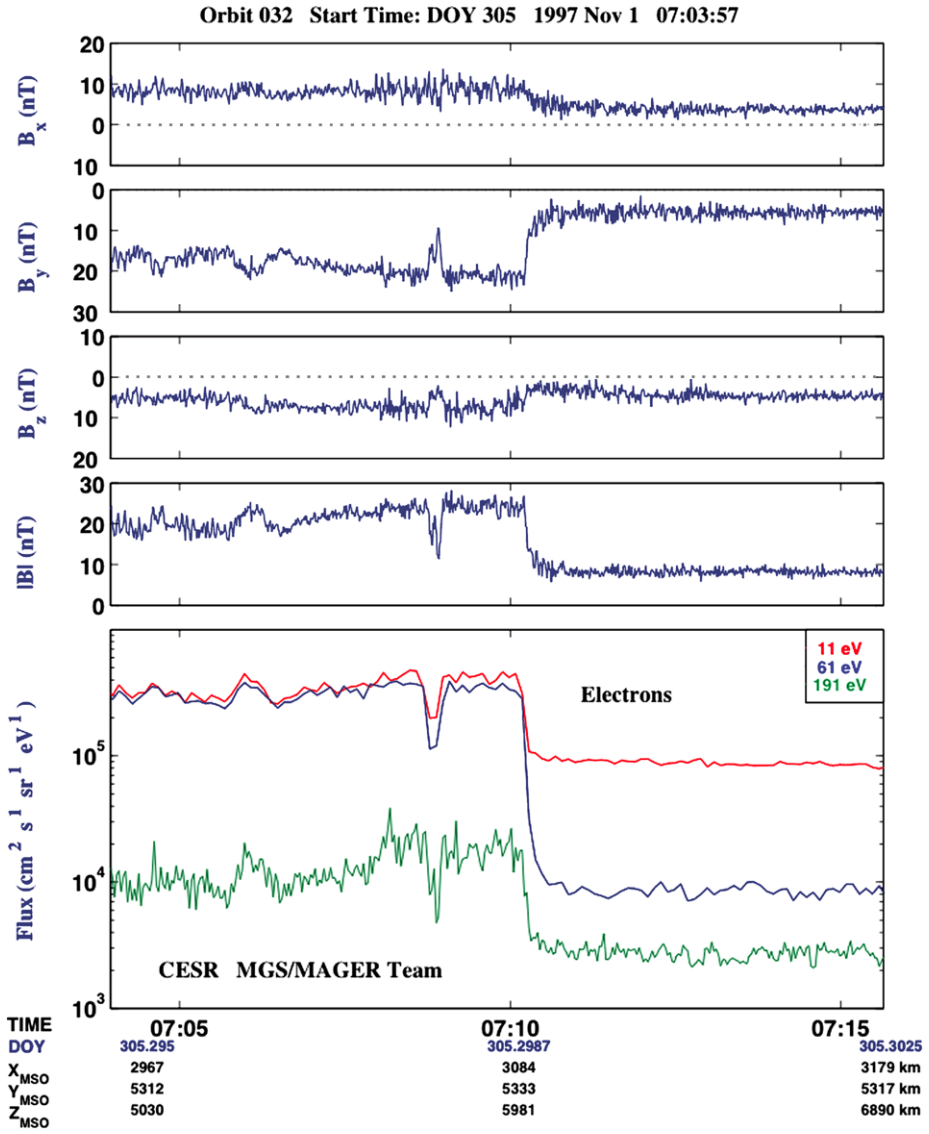

Fig. 2 Magnetic field in MSO coordinates and electron fluxes between 10 and 190 eV measured by MGS MAG/ER during a Martian bow shock crossing (Bertucci et al. 2005b)

and a quasi-parallel-like shock crossing (bottom). In the upper panel, the shock ramp and overshoot are clearly visible. In the middle panel an important wave activity precludes the identification of the ramp. The bottom panel shows a quasi-parallel shock crossing extended over a very large region (12:30–13:00 UT) where no steep ramp can be identified because of the presence of high amplitude, non-linear waves (Bertucci et al. 2005b). Bow shock's averaged shape, size and controlling factors are covered in Sect. 2.3.2, where they are compared with the IMB.

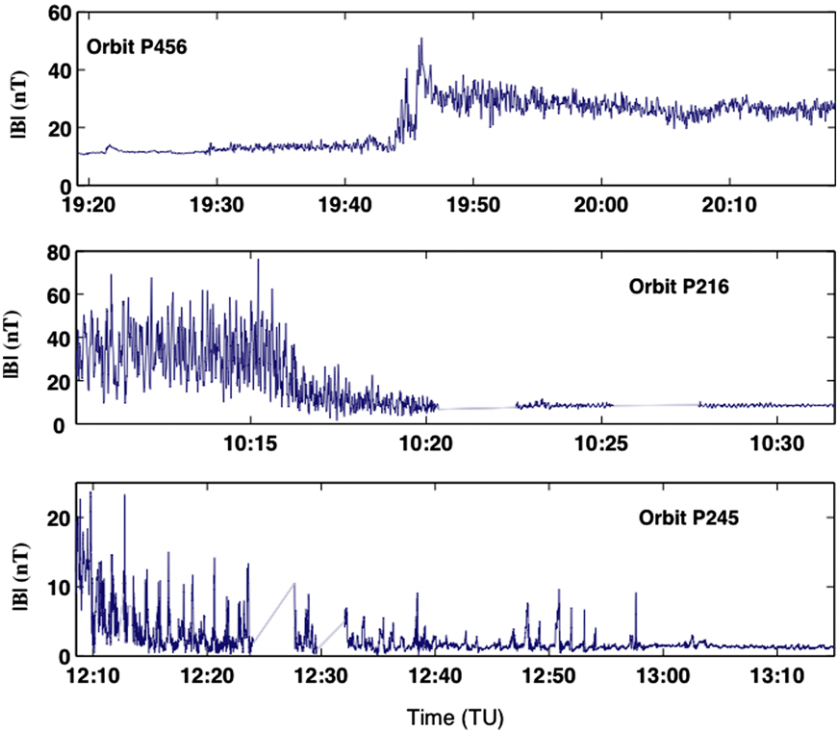

Fig. 3 MGS/MAG magnetic field strength profiles of the Martian bow shock for three different types of bow shock geometries (Bertucci et al. 2005b)

2.2 Magnetosheath

As for the shock, the distinct characteristic of the Marian magnetosheath is its exiguous extent. Moses et al. (1988) pointed out that the distance between the Martian bow shock and the so-called obstacle is of the order of a solar wind proton gyroradius and therefore there is no room for solar wind thermalization. Dubinin et al. (1993a) indicate that not only solar wind but also planetary proton thermalization would require a region extending from the shock including the induced magnetosphere.

The Martian magnetosheath is also filled with ultra low frequency plasma waves which are observed up to the induced magnetosphere boundary. In a study comprising 282 MGS magnetosheath passes, Bertucci et al. (2004) reported linearly polarized ultra low frequency magnetic field and superthermal electron fluctuations within the Martian magnetosheath in 48% of the time. These compressive magnetic field oscillations were found to be anticorrelated to the superthermal electron density suggesting that they are mirror mode waves. This purely kinetic mode is stationary in the plasma frame ($\omega_r = 0$) for a homogeneous media and is generated from temperature anisotropies in the particle distribution function in a high beta plasma (Hasegawa 1975). Possible sources for these anisotropies are the heating of the ion population downstream from quasi-perpendicular shocks and/or distributions (likely non-gyrotropic) of heavy (O^+) pickup ions. Another possibility is that these waves be related to the occurrence of the IMB itself. Similar observations were reported against the IMB at comets P/Halley (Mazelle et al. 1991), and P/Giacobini–Zinner (Tsurutani et al. 1999) seem

to support this idea. A global study by Espley et al. (2004) confirmed the observations by Bertucci et al. (2004).

2.3 The Induced Magnetosphere Boundary (IMB)

At Mars, the outer edge of the induced magnetosphere revealed itself as a distinct, sharp discontinuity, of which one of the most predominant signatures is the increase in the magnetic field strength by a factor of 2 to 3 (Acuña et al. 1998). This feature appeared so evident in the first in situ magnetic field measurements well above the collisional ionosphere that it was interpreted as an intrinsic magnetopause (e.g., Dolginov et al. 1976). However, contemporary interpretations also suggested its atmospheric origin (e.g., Russell 1978a, 1978b).

2.3.1 Identification and Structure

Mars' IMB was first unambiguously detected by spacecraft Mars-5 (Vaisberg 1976) and systematically studied by spacecraft Phobos 2 (Yeroshenko et al. 1990; Grard et al. 1989; Trotignon et al. 1996, 2006; Sauer et al. 1992), followed by MGS (Vignes et al. 2000; Bertucci et al. 2003a, 2004, 2005a, 2005b) and Mars Express (Dubinin et al. 2006a, 2008a, 2008b; Fränz et al. 2006a). The features that usually characterize the dayside IMB and its surrounding on the dayside are:

(a) Sharp increase in the magnetic field strength by a factor of 2–3.
(b) Sharp Decrease in the magnetic field fluctuations.
(c) Sharp enhancement of the magnetic field draping.
(d) Decrease in the temperature of electrons.
(e) Increase in the total electron density.
(f) Decrease in the solar wind ion (H^+ and He^{++}) densities.

The sudden increase in the IMF strength followed by the reduction of magnetic field fluctuations is the most noticeable signature of the IMB. Figure 4a shows MAGER magnetic field orientation in MSO spherical coordinates, magnetic field strength, altitude and electron fluxes for energies between 40 and 120 eV for the outbound leg of a MGS orbit. From right to left, MGS crosses the shock around 0732 UTC, and stays in the magnetosheath until 0703. The shocked plasma there is characterized by highly fluctuating, weak magnetic fields and enhanced and, also variable, electron fluxes. The IMB is crossed around 0702 UTC where $|B|$ varies from around 15 to 30 nT in less than a minute and the fluctuations in the magnetic field strength and direction fade out. At the same time, 40 eV electron fluxes fall from 2×10^6 to 2×10^5 s^{-1} cm^{-2} sr^{-1} eV^{-1}. This decrease is smaller but still noticeable for higher energies in agreement with the predicted cross section for electron impact ionization (Crider et al. 2000). As it will be shown later, this does not imply a decrease of the total electron density but an increase, followed by a decrease of the fluxes of superthermal electrons. At times earlier than 0702, MGS explores the magnetic pileup region or induced magnetosphere, where fields remain strong and quiet.

Figure 4b shows Phobos-2 solar wind proton density, their velocity vector MSO X and Y components, and the magnetic field strength, MSO elevation and azimuth (after Sauer et al. 1992). In the Mars Solar Orbital (MSO) system, the x-axis is directed toward the Sun, the z-axis is directed along the Mars orbital angular momentum vector and the y-axis completes the right-handed system. As observed in MGS data, the magnetic field fluctuations are strongly damped inside the IMB. However, the increase in the magnetic field strength is gradual. This can be interpreted as a spatial effect as Phobos-2 (whose periapsis was at

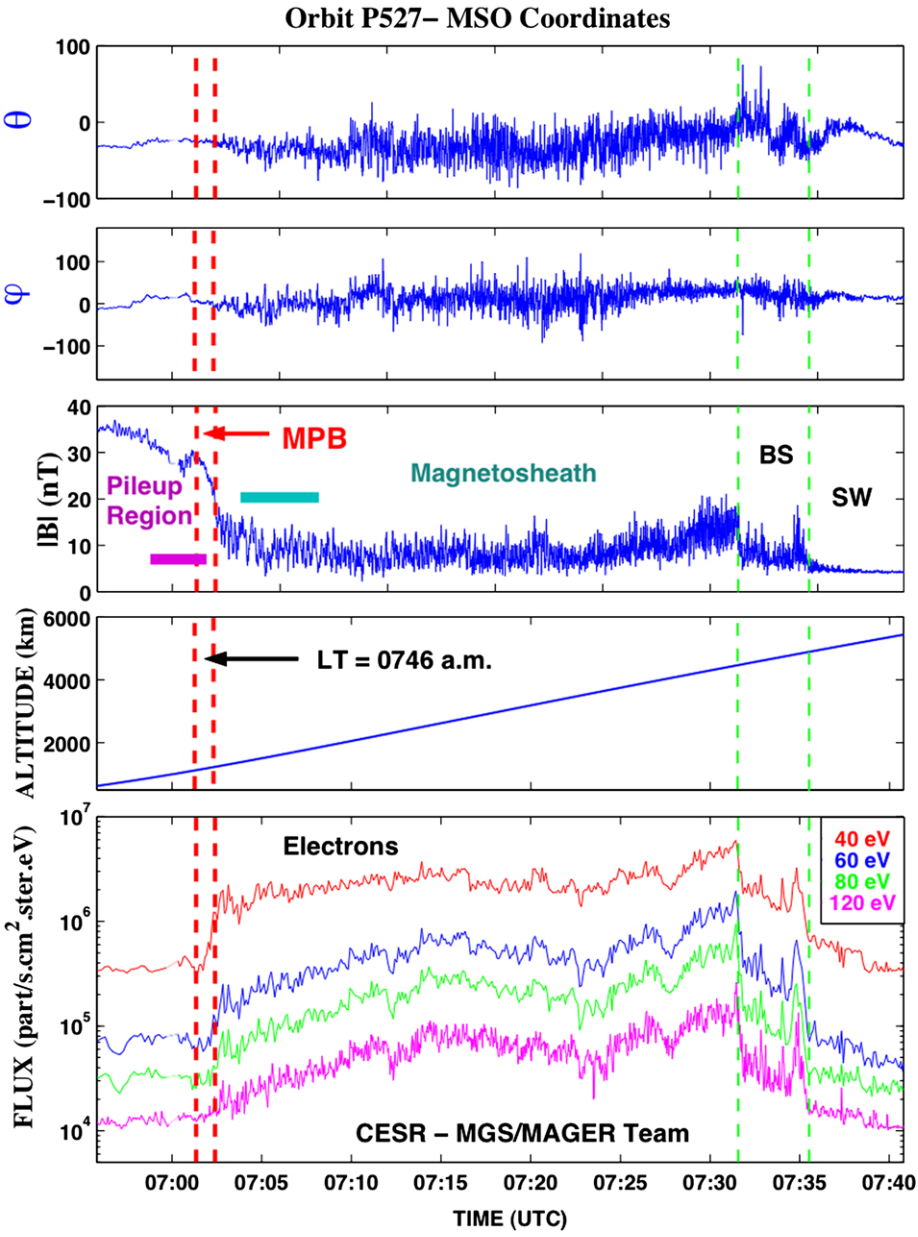

Fig. 4a From top to bottom, MGS Magnetic field in MSO spherical coordinates: elevation ($\theta = 0$ means ecliptic), azimuth ($\varphi = 0$ means noon) (Adapted from Bertucci et al. 2003a)

865 km, very close to the IMB location) orbital velocity near the IMB was rather horizontal. The upper panel shows the decrease in the solar wind proton density as Phobos 2 passes from the magnetosheath into the induced magnetosphere (from $\sim$2.5 cm^{-3} to near-zero values). This behavior was confirmed by ASPERA measurements not only for solar wind protons but also for alpha particles (Fränz et al. 2006a).

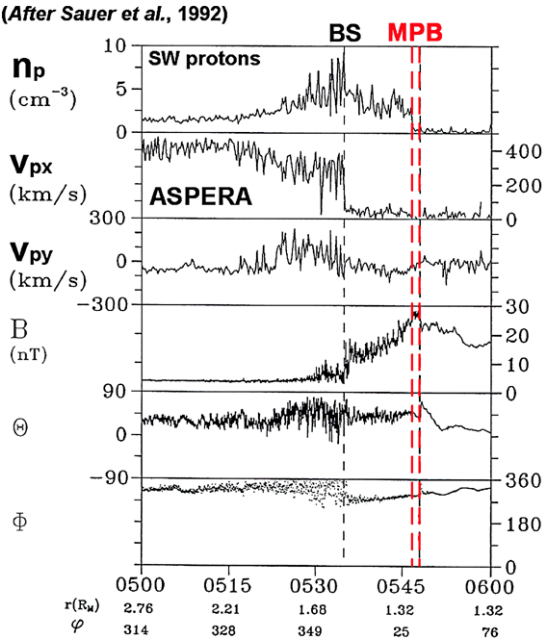

Fig. 4b From top to bottom, Phobos-2 proton density, proton velocity components XMSO and YMSO and magnetic field in MSO spherical coordinates (Adapted from Sauer et al. 1992)

Figure 5 shows MEX ASPERA/MARSIS measurements along the outbound leg of an orbit on July 9, 2007 as the spacecraft emerges from the Martian ionosphere into the unshocked solar wind (Dubinin et al. 2008a, 2008b). On the left end of the figure panels, the ionosphere is well recognized from the appearance of the energy peaks in the range between 20 and 30 eV on the electron spectrograms (Frahm et al. 2006), followed and the ∼20–30 eV O^+ and O_2^+ with energies also recorded by ASPERA-3. The superimposed curves of solar wind ($E_e > 5$ eV) electron density measured by ASPERA-3 (white) and the total electron density measured by MARSIS (black) begin to diverge at the IMB in coincidence with the decrease in the fluxes of superthermal electrons observed on MGS/ER data. As anticipated earlier, this indicates an increase in the total plasma density driven by the increase in the planetary cold electron density, as the solar wind electrons fade out. The IMB is indeed a thin layer (∼25 km ∼0.4 c/ω_{pi}) where there is also a sudden jump of the magnetic field strength. It is noteworthy, however, the fact that this abrupt increase in the magnetic field pileup is not always present (e.g. Bertucci et al. 2003a; Dubinin et al. 2008a, 2008b). In such cases, the IMB is still well identified by the drop in solar wind electrons and the increase of draping. The IMB is also the place where the thermal pressure in the magnetosheath balances the magnetic pressure in the induced magnetosphere (Dubinin et al. 2008a, 2008b).

Another characteristic of the IMB is the enhancement observed in the magnetic field draping (Bertucci et al. 2003a). This enhancement was detected from the correlation between the MSO aberrated (4°) flow-aligned and cross flow components of the magnetic field: $B_{x'} = B_{XMSO'}$ and $B_r = (B^2_{YMSO'} + B^2_{ZMSO'})^{1/2}$. Whereas outside the IMB, inside the magnetosheath, both components are poorly correlated, this correlation significantly improves inside the IMB.

The IMB comprises a layer where the magnetic field rotates defining a directional discontinuity. The structure of such discontinuity was studied by Bertucci et al. (2005a), who applied minimum variance analysis (MVA, Sonnerup and Scheible (1998)) on Martian IMB crossings by MGS. The study showed that the normal component of the magnetic field

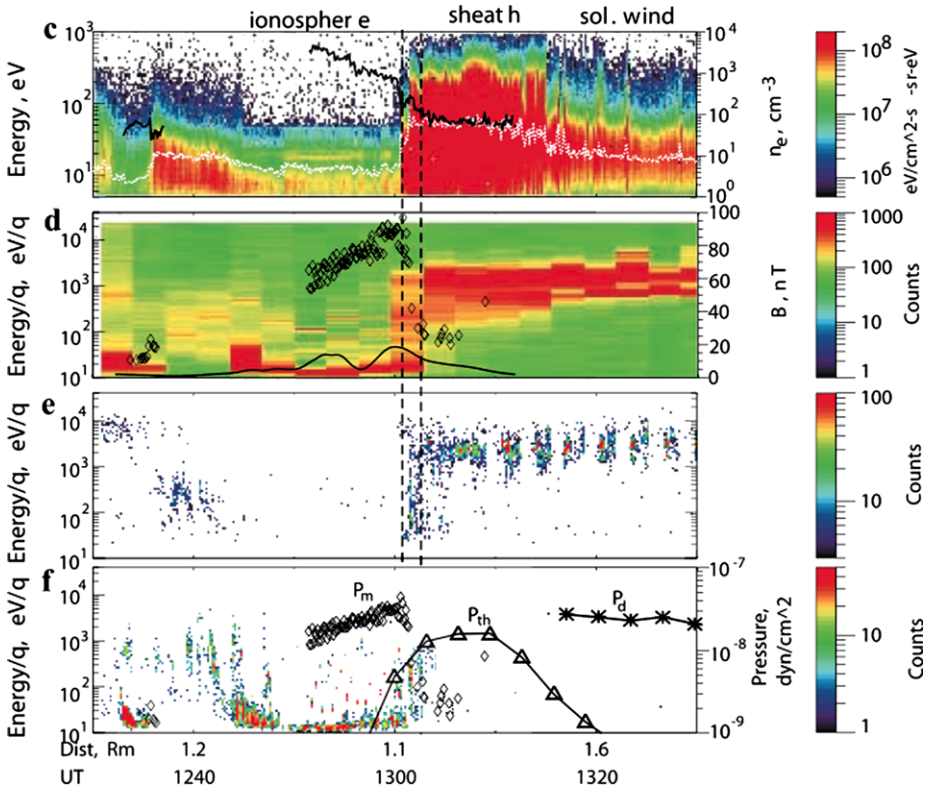

Fig. 5 MEX ASPERA/MARSIS measurements on July 9, 2007 from Dubinin et al. (2008a). The *dashed curve* corresponds to the averaged position of the IMB. Energy-time spectrograms of the (**c**) electrons with the imposed curves of ne from ASPERA (*white*) and MARSIS (*black*) and (**d**) all ion species, (**e**) He++, and (**f**) heavy ($m/q > 16$) ions. Imposed curves are: the magnetic field value from the MARSIS observations (*diamonds*) and Cain et al. (2003) crustal field model (*solid*) (**d**), the magnetic pressure P_m (*diamonds*), the thermal proton pressure P_{th} (*triangles*), and the solar wind ram pressure P_d (*asterisks*)

at the IMB is usually negligible (Fig. 6), as in a MHD tangential discontinuity. However, the changes in the dominant population occurring at the IMB make the comparison with single fluid plasma theory discontinuity properties a simplification. In agreement with ASPERA measurements mentioned above, Bertucci et al. (2005a) find a thickness of 80 km for the current layer within the IMB along which an estimated volume current density $|J_V| = 81$ nA m^{-2} flows. The IMB extends into the downstream sector where it becomes the magnetotail boundary and similar criteria are used to identify it Vignes et al. (2000), Edberg et al. (2009a).

2.3.2 Comparison of Martian IMB and Bow Shock Sizes, Shapes and Controlling Factors

The shape and location of the Martian BS and IMB have been studied in the past by e.g. Slavin and Holzer (1981), Vignes et al. (2000), Bertucci et al. (2005b), Trotignon et al. (2006) and Edberg et al. (2008). During the Phobos 2 mission the number of bow shock and IMB crossings were 127 and 41, whereas during the MGS mission, 573 (Trotignon et al. 2006) and 1149 (Bertucci et al. 2005b), respectively. In the data set of MEX/ASPERA-3 from 2004 until 2008 have 5014 IMB crossings and 3277 BS crossings been identified

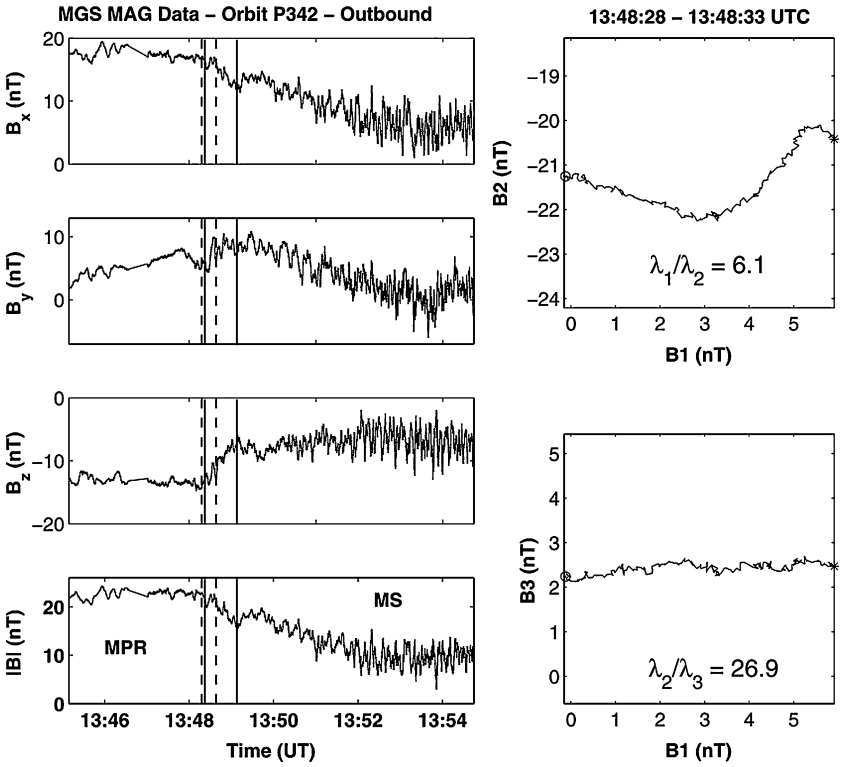

Fig. 6 High-resolution (32 s^{-1}) MGS MAG data (MSO coordinates) for a Martian MPB crossing (*solid lines*) on orbit P342 around 63° SZA. MVA is applied between 1348:18 and 1348:38 UTC (*dashed lines*). Magnetosheath (MS) and the magnetic pileup region (MPR) are indicated for reference. On the right, two hodograms show the magnetic field projection on the minimum variance planes (e1, e2) and (e1, e3) between 1348:28 and 1348:33 UTC. Start and the end of the hodograms are marked with *circles* and *stars*, respectively. Eigenvalue ratios are also indicated

(Edberg et al. 2009b). The number of crossings during the overlapping mission time between MGS and MEX (Feb 2004–Nov 2006) is 2500 and 1840, respectively.

Figure 7 shows the position of all BS (red dots) and IMB (green dots) crossings from MEX 2004–2008 and MGS-derived fits to the boundaries from Edberg et al. (2008). The shape of both the BS and the IMB have been shown to be well represented by conic sections $r = L/(1 + \varepsilon \cos(\theta))$, where r and ε are polar coordinates with origin at X_0 referenced to the MSO x-axis and θ and L are the eccentricity and semi-latus rectum, respectively. This particular shape has been determined from statistical studies using single-spacecraft measurements and recently confirmed through two-spacecraft study using near-simultaneous MEX and Rosetta measurements during the Rosetta Mars flyby in February 2007 (Edberg et al. 2009a). The BS is on average located at an altitude of $0.58R_M$ (∼2000 km) and the IMB at an altitude of $0.33R_M$ (∼1100 km) at the subsolar point. On the terminator plane, the BS is on average at an altitude of $1.6R_M$ (∼5400 km) and the IMB at $0.45R_M$ (∼1500 km).

The factors that have been studied for possible effects on the location of these boundaries include the IMF direction (Vignes et al. 2002; Brain et al. 2005), the crustal magnetic fields (Crider et al. 2002; Dubinin et al. 2006a; Fränz et al. 2006a; Edberg et al. 2008, 2009b), the solar wind dynamic pressure (Crider et al. 2002; Brain et al. 2005; Edberg et al. 2009b), the

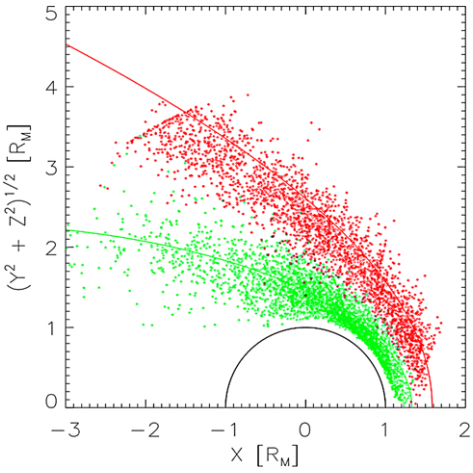

Fig. 7 The position of all BS (*red dots*) and MPB (*green dots*) crossings by MEX from 2004 until 2008. The *red* and *green lines* are previously obtained best fits to the boundaries derived from MGS measurements from Edberg et al. (2008)

EUV flux and solar cycle (Vignes et al. 2000; Edberg et al. 2009b), and the magnetosonic Mach number (Edberg et al. 2010).

Measurements of and Proxies for the Controlling Factors The instruments and orbits of three spacecraft have been relevant for describing which factors that control the location of plasma boundaries at Mars: MGS, MEX and the ACE spacecraft. ACE is in orbit around the L1 Lagrange point upstream of Earth and continuously measures the solar wind proton density, temperature and velocity as well as the vector magnetic field.

Crider et al. (2002) and Brain et al. (2005) have developed proxies for both the solar wind dynamic pressure and the IMF direction from MGS/MAG measurements. The proxies have been formulated in terms of measurements of the average magnetic field strength and draping azimuth at 400 km altitude. The field strength is assumed to balance, and therefore be a proxy for, the solar wind dynamic pressure. The pressure proxy is given by the magnetic field strength B_{proxy} which can be converted to magnetic pressure $P_B = B^2_{\text{proxy}}/2\mu_0$.

The solar EUV flux proxy has been determined from the F10.7 radio flux at 2–200 nm measurements at Earth extrapolated to Mars (Mitchell 2001).

The solar wind (proton) velocity v and density n moments can be calculated from MEX/IMA measurements outside of the BS which is a more direct measurement of the solar wind dynamic pressure $P_{\text{dyn}} = m_p n v^2$, where m_p is the proton mass. For details regarding the moment calculations from MEX/ASPERA-3, see Fränz et al. (2006b). The pressure determined from MEX that is described here is calculated as a mean over 10 min of measurements exterior to a BS crossing.

Influence of the Solar Wind Dynamic Pressure Figure 8, panel (a), shows the extrapolated (Vignes et al. 2002; Crider et al. 2002) terminator distances R_T of the BS crossings as a function of upstream solar wind dynamic pressure $P_{\text{dyn,IMA}}$ as measured by MEX/IMA (Edberg et al. 2009b). The crossings are binned into $0.05 R_M$ bins and the mean values of the dynamic pressure upstream of all crossings in each bin are calculated. The error bars show standard error on the mean (standard deviation divided by number of samples in each bin). There is a trend to smaller radial distance for higher dynamic pressure, with a correlation coefficient of -0.51. An exponential curve (solid line) is fitted to the data points. Panel (b) shows the terminator radius of the IMB as a function of $P_{\text{dyn,IMA}}$. Again, there is a clear trend

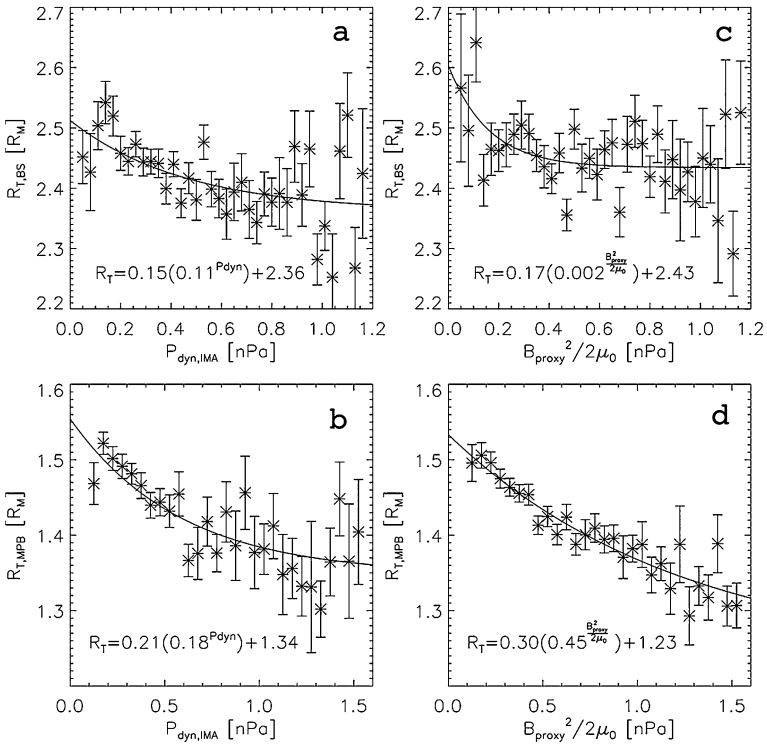

Fig. 8 The influence of the dynamic pressure on the BS and MPB. The panels show (**a**) the altitude of the BS extrapolated to the terminator plane as a function of the dynamic pressure measured by IMA on MEX, (**b**) the terminator altitude of the MPB as a function of $P_{\mathrm{dyn,IMA}}$, (**c**) the terminator altitude of the BS as function of the MGS pressure proxy and (**d**) the terminator altitude of the MPB as a function of the MGS pressure proxy. Reproduced from Edberg et al. (2009b)

to smaller radial distances for higher $P_{\mathrm{dyn,IMA}}$ with a correlation coefficient of -0.74, and the same type of exponential curve is fitted to the data points. The error bars at low radial distance tend to increase which could be an effect of the stronger influence of the crustal fields at lower altitudes. However, it could also be an effect of fewer data points in these bins. The results visualized in these two panels clearly show that the solar wind dynamic pressure has an influence on the location of the boundaries.

These results were also compared to those obtained when the MGS pressure proxy is used, rather than $P_{\mathrm{dyn,IMA}}$. Panel (c) and (d) show the terminator radius of the BS and IMB, respectively, as a function of the MGS pressure proxy $P_B = B^2_{\mathrm{proxy}}/2\mu_0$. The pressure proxy values are linearly interpolated to the time of the boundary crossings. Surprisingly, there is no obvious trend for the variation of the BS radius (correlation coefficient of -0.41) whereas the trend for the IMB is very similar to that in panel (b) (correlation coefficient of -0.93). The lack of a trend for the BS crossings could be explained by the time difference between the time of the pressure proxy measurement and the BS crossings, which can be as long as 1 hour. The BS is expected to move on time scales much shorter than that. For the IMB the same problem with the time difference should arise but the results in panel (b) and (d) are still very similar, which rather disproves the argument above, if the BS and IMB move on the same timescales. It is also likely that the IMB and the BS can simply

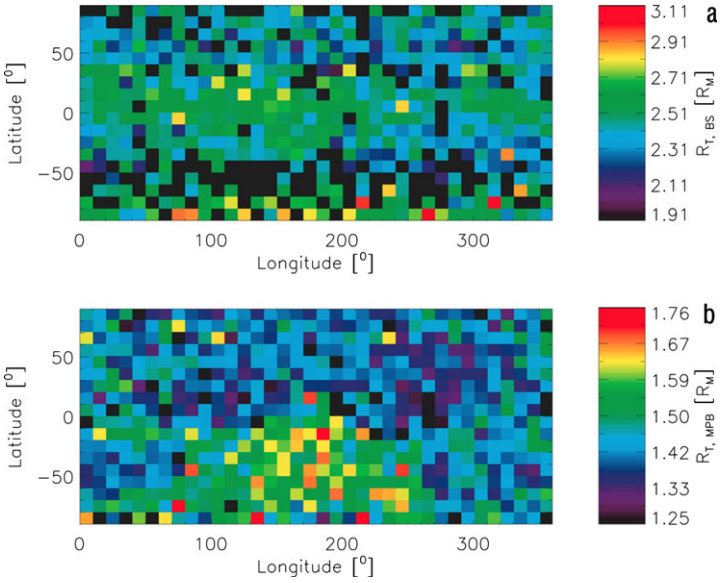

Fig. 9 The influence of the crustal magnetic field on the BS and MPB. The panels show color-coded the mean extrapolated terminator altitude of the (**a**) BS and the (**b**) (MPB) in longitude-latitude bins. Reproduced from Edberg et al. (2009b)

respond differently to changes in the solar wind dynamic pressure. The pressure proxy and the measured pressure values do not match up perfectly and this could be an indication of an unknown compression factor between the solar wind dynamic pressure outside the BS/IMB and the magnetic pressure inside the IMB.

It is also possible that when the BS is at very low radial distances the crustal magnetic fields become more important while at the same time the dynamic pressure becomes less important. The dynamic pressure can only push the boundary down to a certain altitude before the magnetic pressure from the crustal fields together with the plasma pressure inside of the BS become too high and the trend of a lower radial distance for a higher dynamic pressure vanishes. Similarly, when the BS is at very high radial distances the IMF direction could become more important while at the same time the dynamic pressure becomes less important.

Influence of the Crustal Magnetic Fields The crustal fields have been shown to influence the boundaries by using MGS and MEX measurements (Crider et al. 2002; Brain et al. 2005; Fränz et al. 2006a; Edberg et al. 2008, 2009b). Panel (a) and (b) in Fig. 9 (from Edberg et al. 2009b) show two global $10° \times 10°$ longitude-latitude maps color coded by the radial distance of the BS and IMB, respectively. All crossings from 2004 until 2008 from the dayside of Mars are used and the mean of the radial distance of all crossings within each bin are shown. Bins with less than two crossings are colored black. The strongest crustal fields are located in the southern hemisphere at longitudes between 90° and 270° (Connerney et al. 2005). The map of the BS crossings, panel (a), shows no distinct influence of the crustal magnetic fields on the altitude of BS, i.e. there is no specific region where the boundary is at larger radial distance than elsewhere and which also corresponds to a region of strong crustal fields. There are, unfortunately, many empty bins at southern latitudes where the crustal fields are strongest. However, the mean value of RT of all the dayside BS crossings in the northern

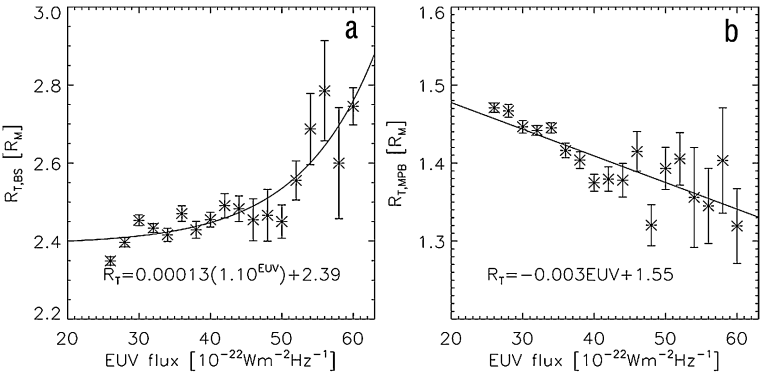

Fig. 10 The influence of the EUV flux on the (**a**) BS and (**b**) MPB. The EUV flux is determined through a proxy using the F10.7 measurements at Earth and then extrapolated to Mars. Reproduced from Edberg et al. (2009b)

hemisphere is $2.45R_M$ compared to $2.49R_M$ in the southern hemisphere and in the bottom rows of panel (a), at southern latitudes, there is a weak tendency that the crossings are at higher distances. The difference is statistically significant according to a Student's t-test at 95% confidence level. This difference is smaller than the difference presented in Edberg et al. (2008) where MGS crossings where used. The accuracy in this study should, however, be better due to the much larger data set.

The influence of the crustal magnetic fields on the IMB is much clearer. In panel (b) of Fig. 9 there is a large area at southern latitudes between longitudes from ∼90° to ∼270°, where the IMB occurs at larger radial distances than elsewhere. This region corresponds very closely to the region where the strongest crustal fields are located. Also, at latitudes above −30° and at longitudes between 0° and 90° there is a less prominent but still visible area of higher IMB which corresponds to a region of intermediately strong crustal fields.

Results show that the IMB is strongly affected by the crustal fields, but the BS to a much lesser extent. The influence on the BS is still somewhat ambiguous due to a lack of sufficiently many BS crossings over the southern crustal magnetic anomalies. Vignes et al. (2002) found that the BS was not influenced while Edberg et al. (2008) found evidence that it was indeed influenced, both using MGS measurements.

Influence of the Solar EUV Flux Figure 10 from the study by Edberg et al. (2009b) depicts the results on the dependence of BS and IMB with respect to the solar EUV flux. The crossings are divided into 2.0×10^{-22} W m^{-2} Hz^{-1} bins and the mean of the radial distance for all crossings within each bin is calculated. There is a clear trend of a larger BS radius for a higher EUV flux and it seems to increase exponentially. For the BS an exponential curve is fitted to the data points. The IMB on the other hand clearly decreases in radius when the solar EUV flux increases and it seems to decrease linearly as the fit in panel (b) shows. Modolo et al. (2006) used a hybrid simulations to study the influence of the EUV flux on the plasma boundary and found that the BS was pushed outward at the subsolar point but moved in at the terminator plane when going from solar minimum to maximum conditions, while the IMB only moved inward at the terminator, in agreement with this study. The data used in this study are all taken during the declining phase of the solar cycle and during solar minimum (2004–2008) and therefore it cannot be yet determined how the EUV flux at solar maximum will affect the boundaries. However, comparisons between the BS and IMB fits

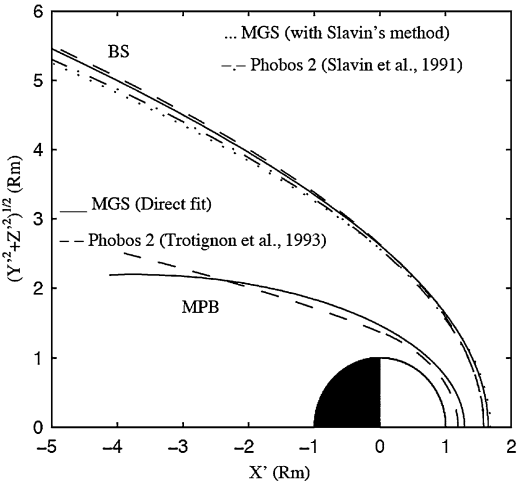

Fig. 11 Martian BS and IMB fits from MGS and Phobos 2 (Vignes et al. 2000)

from Phobos-2 (Slavin et al. 1991; Trotignon et al. 1993) and MGS observations (Fig. 11) suggest that the position of both boundaries is not sensitive to solar cycle phase (Vignes et al. 2000).

Influence of Magnetosonic Mach Number Vennerstrom et al. (2003) extrapolated Earth upstream conditions to Mars by studying the magnetic field measured by ACE and compared that to the MGS measured fields at Mars during an interval in 1999 when Mars and Earth were close to being aligned on a Parker spiral. To perform such an extrapolation a time shift had to be applied to the ACE measurements which took into account the radial distance as well as the longitudinal distance between the two planets (Vennerstrom et al. 2003).

Two intervals when Mars and Earth are in the same solar wind sector have occurred since MEX arrived at Mars, starting in 2005 and in 2007, and were used by Edberg et al. (2010) for studying the effect of the magnetosonic Mach number.

In Fig. 12 the terminator distances of the BS crossings from these two intervals are plotted as a function of the magnetosonic Mach number, as measured by ACE and extrapolated to Mars. The mean distance is calculated in Mach number bins of 0.25, ranging from Mach number 6.1 to 10.5. Outside of this interval there are too few data points in each bin (<10). Crossings that take place outside the SZA range 40°–110° are removed in order to avoid any orbital bias. A linear curve is fitted to the mean values and there is a clear trend of a lower BS altitude for an increasing Mach number. Clearly, when the Mach number is higher than average, the BS becomes compressed. When the Mach number drops, the BS moves to higher altitudes.

Edberg et al. (2010) results show that the Martian BS altitude decreases near-linearly with increasing Mach number calculated from ACE, which is similar to results obtained for the Venus BS by the Pioneer Venus Orbiter mission (Slavin et al. 1980). The IMB on the other hand does not seem to be affected by the Mach number.

Influence of IMF Direction/Upstream Convective Electric Field Edberg et al. (2009b) also studied how the boundaries reacted to different directions of the convective electric field. It was, however, found that the IMF direction had a very weak influence on the boundaries if compared the other factors. This is not to say that the IMF direction is unimportant but rather that the method of using the MGS derived proxy for the IMF direction is not sufficiently

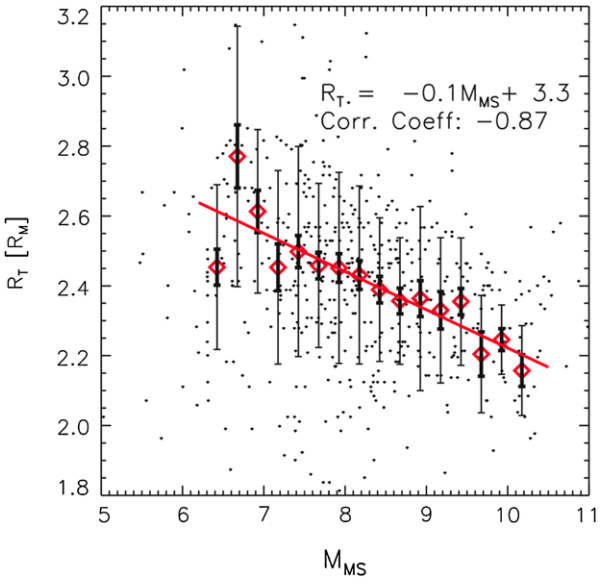

Fig. 12 The influence of the magnetosonic Mach number on the BS. The Mach number is determined from ACE measurements of the solar wind parameters at Earth and then extrapolated to Mars (Edberg et al. 2010)

good or accurate. Vignes et al. (2002) showed that the IMF does have an influence on the boundary locations. This is also observed in simulations (see e.g. Modolo et al. 2006).

2.4 The Induced Magnetosphere

The induced magnetosphere is the region populated by draped external field lines and largely dominated by planetary plasma (especially O^+ and O_2^+). But also, the induced magnetosphere is the place where most of the transfer of energy and momentum from the solar wind to the Martian plasma occurs (Dubinin et al. 2006a, 2006b). Several authors point at the boundary layer and the tail rays as the substructures where escaping local plasma are concentrated (Lundin et al. 1991; Lundin and Dubinin 1992, Dubinin et al. 2006b, 2006c).

On the dayside, the induced magnetosphere is a region of a few hundred kilometers thick with highly piled up fields which form a more or less efficient barrier against the protrusion of the external plasma. In spite of the low beta that characterizes the dayside induced magnetosphere (referred to it as magnetic pileup region, MPR), compressive (i.e. correlated with plasma density oscillations), quasi-monochromatic, linearly polarized waves were observed by MGS (Bertucci et al. 2004). The oscillations also display a wave vector normal to the background magnetic field. All these signatures suggest that these oscillations are fast magnetosonic waves. As mentioned above, these waves are sometimes accompanied by mirror-mode waves in the magnetosheath (Fig. 13) where the magnetic oscillations are anti-correlated to the plasma density. A survey of 282 IMB crossings by MGS shows that fast magnetosonic waves occur at least 27%. Fast magnetosonic (IMB) and mirror mode (magnetosheath) waves coincide in at least 18% of the observations. Finally, at least 11% of the observations show neither of them.

Far from regions where crustal magnetic fields dominate, the IMF clock angle seems to play an important role in spatially defining the subregions where escaping plasma channels are located. Near the terminator, the strongest magnetic stresses will be observed in the magnetic polar regions (where field lines try to slip over the planet into the nightside), and

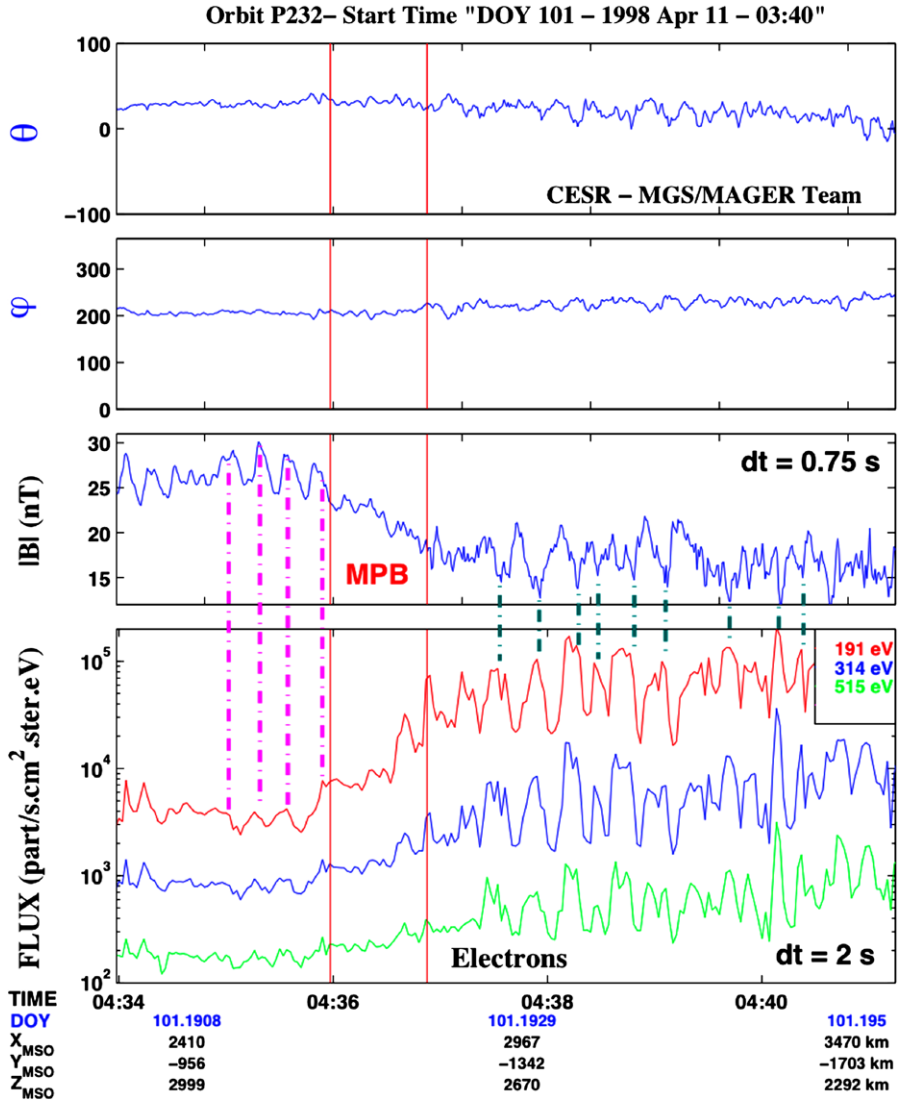

Fig. 13 MGS MAG data in spherical MSO coordinates and ER electron fluxes for 191, 314 and 515 eV during orbit 232. Compressive, magnetic field oscillations occur on either side of the IMB (here identified as MPB): in the IMB (*point-dash lines on the left*) they correlate with the electron fluxes, whereas in the magnetosheath the magnetic field strength is anti-correlated to the electron fluxes (Bertucci et al. 2004)

planetary plasma will be more susceptible to be efficiently accelerated (Fig. 14). This could be the case of the observations reported by Dubinin et al. (2006b, 2006c) where narrow, energetic magnetosheath-like electron events were observed by ASPERA 3 in coincidence with planetary ions (O^+, and O_2^+). In such a scenario, these polar plasma channels would be associated with the gradual formation of a plasma sheet separating the lobes of the magnetotail. The authors also mentioned the reconnection between the IMF and the crustal magnetic fields as an alternative mechanism.

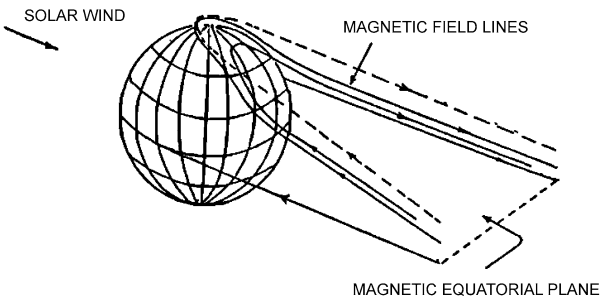

Fig. 14 Schematic of magnetic field lines draping around the ionosphere indicating their entry into the wake over the magnetic polar regions where magnetic stresses become maximum (from Pérez-de-Tejada 1986)

The narrow structures found at Mars could be similar to the tail rays observed around Venus (Brace et al. 1987) and explained as a result of the penetration of the convective electric field into the ionosphere near the terminator (Luhmann 1993). This possibility was mentioned by Dubinin et al. (2006a) for ASPERA-3 ion beams detected near the Martian terminator.

In the nightside, the induced magnetosphere becomes the magnetotail. It consists of two lobes opposite polarity separated by a neutral sheet. The Martian magnetotail has not been extensively explored. However, mid and short-range observations by Phobos-2 and MGS respectively have provided some basic properties about its magnetic structure. Using Phobos-2 observations at $2.86R_M$, Yeroshenko et al. (1990) and Schwingenschuh et al. (1992), reported that the mid range magnetotail field geometry depends on the IMF clock angle. Halekas et al. (2006) obtained a similar result at 400 km altitude, far from the magnetic crustal sources. Rosenbauer et al. (1994) found a dependence of the magnetic pressure within the magnetotail on the solar wind ram pressure from which they obtained an average flaring angle of $\sim$13°. Zhang et al. (1994) found a similar result. In a work based on MGS data, Crider et al. (2004) found that the short-range magnetotail flares out from the Mars–Sun direction by 21°.

The Martian crustal sources play an important role in altering the magnetic topology in the low altitude induced magnetosphere at certain latitudes. Brain et al. (2002) found that the influence of crustal sources can be perceived up to 1300–1400 km altitude, depending on the local time, and latitude. They also mention that IMF/Crustal field reconnection may occur. More recently, Eastwood et al. (2008) claims that noncollisional reconnection occurs in the magnetotail. Halekas et al. (2008) on the other hand, suggest that IMF/Crustal field reconnection, if regular, could have important consequences on atmospheric escape, while Brain et al. (2010a) reports evidence of bulk atmospheric escape following reconnection.

The Martian magnetotail plasma inventory was studied in detail by MEX. Following the detection of planetary heavy ions (O^+ and O_2^+) confined inside the IMB (Lundin et al. 2004), a characterization of the different populations of planetary ions within the magnetotail was covered in several works. Fedorov et al. (2006) found that the planetary ion energies above 300 eV decrease from the IMB to the plasma sheet in the center of the magnetotail. In the neutral sheet, Fedorov et al. (2008) reported 1-keV energy heavy ions (Fig. 15). This is in agreement with Phobos-2 observations by Dubinin et al. (1993b) who found that this energy is of the order of that of the solar wind ions, an argument in favor of an efficient transfer of linear momentum and energy from external plasma to the planetary plasma via electrostatic fields. In particular, Dubinin et al. (1993b) estimated the energy gained by the planetary ions within the plasma sheet assuming a $j_e \times B$ force where j_e is the electron current density and found that these estimations are of the same order as those measured by Phobos-2/ASPERA.

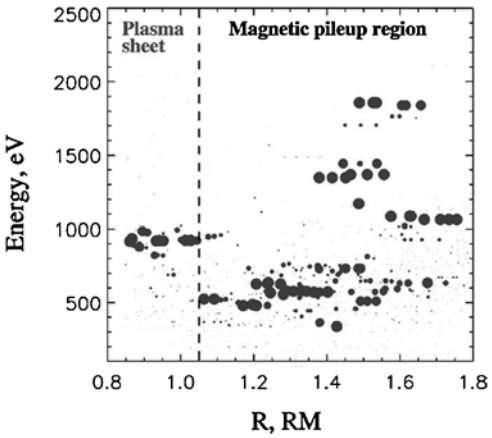

Fig. 15 Scatterplot of the planetary ions energy versus $(Y^2_{MSO} + Z^2_{MSO})^{(1/2)}$. *Each circle* corresponds to the one complete IMA energy-angular spectrum. The diameter of the circle shows the total count rate of the event. The *vertical dashed line* separates the tail lobes from the plasmasheet (Fedorov et al. 2006)

The influence of the convective electric field in the IM plasma morphology was also studied from ASPERA-3 measurements. Fedorov et al. (2008) found a slight asymmetry in the distribution of planetary ions within the plasma sheet, and Dubinin et al. (2008b), reported that the ion fluxes within the IM display asymmetries due to the IMF and the crustal fields.

However, the planetary plasma escape is dominated by the 'cold' ion population (Lundin et al. 2009). This includes not only H^+ but also heavier species, such as molecular ions (e.g. CO_2^+). An interesting conclusion of Lundin et al. (2009) is that there is no appreciable latitude or local time asymmetry in the escaping flux.

2.5 The Ionospheric Boundary

2.5.1 The Photoelectron Boundary (PEB)

In addition to bow shock and IMB, an additional boundary related to the upper limit of the collisional ionosphere was reported at lower altitudes. However, whether this boundary is similar to the Venusian ionopause (Elphic et al. 1981), is still under debate.

Initial observations by MGS well below the IMB and over regions where crustal field influence was negligible displayed a decrease in the magnetic field (Acuña et al. 1998). This led to think that a Venus-type ionopause was indeed present at Mars. However, until a reliable estimation of the thermal pressure within the collisional ionosphere was made, a real comparison with the Pioneer Venus Orbiter observations would be impossible.

In MGS electron reflectometer ER (Mitchell 2001) and more clearly in the ASPERA-3 electron spectrometer (ELS) data (Lundin et al. 2004; Frahm et al. 2006), ionospheric plasma is well traced by the characteristic energy spectrum of photoelectrons. Photoelectron lines are attributed to both carbon dioxide and atomic oxygen, and are theoretically located in energy between 21 eV and 24 eV, and 27 eV (Mantas and Hanson 1979; Fox and Dalgarno 1979). The relevant photoelectron peaks in the energy spectrum are mainly due to ionization by solar 30.4 nm photons.

Photoelectrons are often observed not only near the planet, but also near the IMB, as shown in Fig. 16, where the photoelectron line is observed from periapsis until an altitude of ~900 km, close to the outbound IMB crossing at ~0408 UT (Dubinin et al. 2006a). On the inbound leg photoelectrons are also observed near the IMB, but at much higher altitudes (up

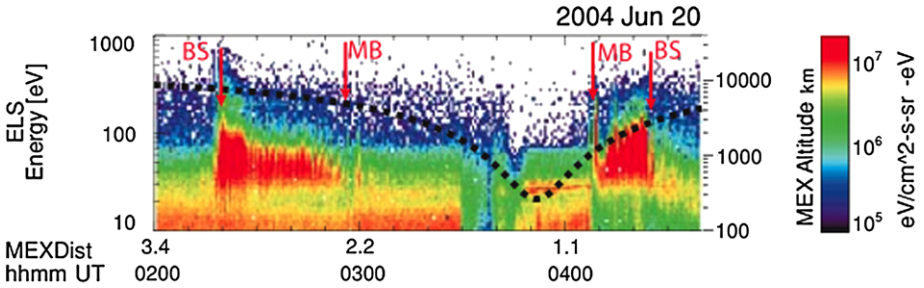

Fig. 16 Electron spectrogram measured by MEX ASPERA-3 ELS on June 20, 2004. The *dotted curve* shows the spacecraft altitude. Crossings of the bow shock, and the IMB (here indicated as MB) (from Dubinin et al. 2006a)

to ∼5000 km ∼0300 UT). However, photoelectrons observed close to Mars on the dayside might be locally produced whereas those in the downstream sector, far from Mars might likely photoelectrons travelling along draped field lines connected to the ionosphere (Frahm et al. 2006). Unfortunately ASPERA-3 ELS cannot discriminate between locally produced and transported photoelectrons (Frahm et al. 2010).

The point in the near Mars space (mostly dayside) where the photoelectron signature sets in defines the photoelectron boundary (PEB). In most MGS and MEX orbits a distinct gap (small or large) exists between the IMB identified by a drop of the sheath electrons and the start of the photoelectron boundary (PEB). The presence of this gap clearly shows that IMB and PEB are indeed two distinct boundaries (Dubinin et al. 2006a).

Finally, it is worth mentioning that the PEB altitude is extremely sensitive to the location of the Martian crustal sources (Brain et al. 2003; Nagy et al. 2004).

2.5.2 MARSIS Ionospheric Electron Density Gradients: Possible Venus-Like Ionopause

Analysis of MARSIS electron density measurements in the ionosphere of Mars revealed the existence of steep gradients similar to the Venusian ionopause. MARSIS ionospheric sounding mode provides electron density measurements from the ionosphere of Mars using two techniques. The remote sounding technique, which provides electron density measurements in the altitude range between 130 and 400 km, involves sending a short radio pulse of frequency f, and measuring the time delay of the returning echo (Gurnett et al. 2005). The second method, which provides electron densities from much higher altitudes, between 275 and 1300 km, is from the excitation of local electron plasma oscillations.

In the ionospheric sounding mode, when the transmitter frequency is near the local electron plasma frequency, electron plasma oscillations are excited at that frequency. Since these oscillations are usually very intense, harmonics of the basic oscillation frequency are introduced in the detector. Ionograms, which are plots of echo intensity as a function of frequency and time delay, then used to display MARSIS data. Electron plasma oscillation harmonics are seen as equally spaced vertical lines at low frequencies. When the plasma frequency is below 100 kHz, the fundamental of the electron plasma frequency cannot be observed. However, the electron plasma frequency can still be determined by measuring the spacing between the harmonics. Once the electron plasma frequencies are obtained, corresponding electron densities can be calculated using the formula $n_e = (f_p/8980)^2$, where the electron density, n_e, is in cm^{-3} and electron plasma frequency, f_p, is in Hz (Gurnett and Bhattacharjee 2005).

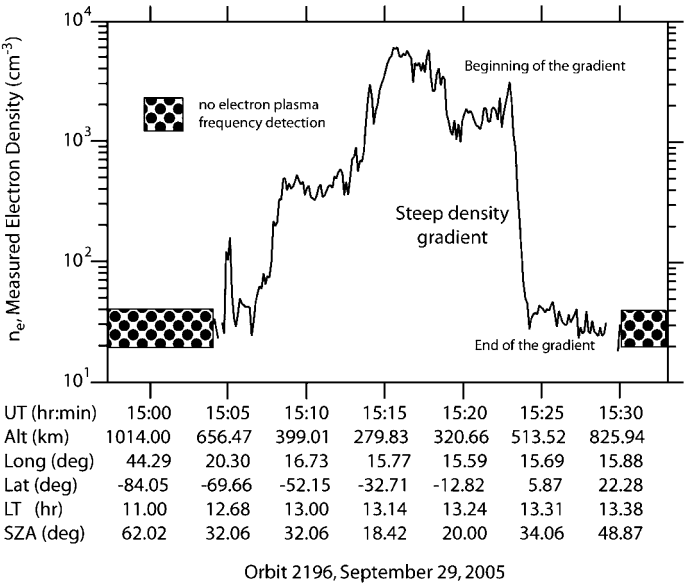

Fig. 17 Pass from September 29, 2005, the electron density in cm^{-3} is presented on the *vertical axis* and *horizontal axis* shows the universal time (UT), altitude (Alt), longitude (Long), latitude (Lat), local time (LT), and solar zenith angle (SZA) (Duru et al. 2009)

Observations Through Excitation of Local Electron Plasma An example of a steep density gradient similar to the ionopause of Venus is shown in Fig. 17 (Duru et al. 2009). The pass starts at around 14:57 UT and ends around 15:33 UT. For the first seven minutes electron plasma oscillations are not detected. The same situation occurs after 15:30 UT. Possible reasons for the disappearance of the electron plasma oscillations are studied extensively by Duru et al. (2009, 2010). After the first detection of the electron plasma oscillations at around 15:04 UT, the electron density increases with decreasing altitude up to about 15:15 UT, where the altitude starts to decrease. A very sharp drop in the electron density is observed at about 15:23 UT. These sharp drops in the ionospheric thermal plasma density are commonly seen at Venus and are identified as the ionopause (Schunk and Nagy 2000; Brace et al. 1980). In this case, the electron density which is 3087 cm^{-3}, decreases to 27 cm^{-3} in about a minute. The beginning of this steep gradient feature is located at an altitude of 419 km and at a SZA of 28°.

In the ionosphere of Venus, steep density gradients are seen very often and are usually observed on both the inbound and the outbound legs of a given pass (Brace et al. 1980). At Mars it was possible to identify only a few MEX passes in which a steep gradient was observed on both legs. In contrast to Venus, Martian steep density gradients occur in only about 18% of the samples studied. This percentage is found by excluding all of the half-passes.

Remote Sounding Observations Remote sounding provides a much better spatial resolution than local plasma density measurements. In an MARSIS ionogram the signature of a Venus-like ionopause is a horizontal line at low frequencies. Out of 132 passes, density drops were detected from remote sounding in 40.

Figure 18 shows four consecutive ionograms from an orbit on November 14, 2005 (Duru et al. 2009). They are separated by 7.54 s, which is the repetition time of the ionospheric sounding. As expected, the steep gradient in n_e is represented by a horizontal line at low frequencies (<0.5 MHz in this case) indicating a rapid increase in density over a short time range. The longer horizontal line seen at around 2.5 ms time delay is the reflection from the horizontally stratified ionosphere. For this pass, the time delay of the steep gradient does not change significantly from one ionogram to the next.

Density Gradient Thickness Drop apparent thickness is calculated by using two methods. In the first method, the local electron density profiles are used and the thickness is defined as the altitude difference between the beginning and the end of the sharp electron density drop. The histogram showing the thicknesses obtained this way is displayed in the top panel of Fig. 19. The mean thickness is calculated to be 37.5 km, with a standard deviation of 20 km.

In the second method, the equation $\Delta h = 1/2\ \Delta t_i\ c$, where $\Delta t_i = t_e - t_b$ is the difference between the time delay at the end of the steep density gradient (t_e) and the time delay at the beginning of the steep density gradient (t_b) (see Fig. 18), and c is the speed of light, is used to calculate the thickness from the remote sounding data. The $1/2$ factor accounts for the fact that the time delay is the time required for the pulse to go and come back from the reflection point. This method should provide a more precise determination of thickness than the method using local plasma oscillations since an ionogram presents data obtained over only 1.26 s, which is the time it takes to complete scan of all the frequencies, between 0.1 MHz and 5.5 MHz, as opposed to the 7.54 s resolution of local plasma frequency data. Spatial and temporal effects are therefore much less likely to affect the results in this method. The altitude resolution of the ionograms is about 14 km with the upper limit of the thickness taken at the calculated value. This method was applied to 55 ionograms. The results are shown in the histogram shown in the bottom panel of Fig. 19. The mean value is about 22 km, with a standard deviation of 8.8 km. The thicknesses obtained from using remote sounding measurements are smaller than those obtained using local electron density measurements. This difference can be attributed to the improved resolution of the remote sounding data eliminating the effect of temporal variations involved in the local density measurements.

It is expected that the thickness of the ionopause boundary should scale with the ion gyroradius (Elphic et al. 1981). The thickness of the crossings and ion cyclotron radius are expected to scale with each other. The ion cyclotron radius varies between 3 km and 22 km with a mean value of 10.31 km and a standard deviation of 4.02 km. The fact that the thickness is usually greater than one ion gyroradius may be due to the ambipolar potential created by the large temperature difference across the regions and layers separating the ionosphere from the magnetosheath.

Spatial Distribution of Density Gradients At Venus, the ionopause altitude changes drastically with changing solar wind conditions (Brace et al. 1980). At Mars, Duru et al. (2009, 2010) reported that ionopause crossings are detected in a large range of altitudes changing between 302 and 979 km. However, most of the crossings lie between about 300 and 600 km. and increase in altitude with increasing solar zenith angle.

The crustal magnetic fields add greatly to the complexity of the ionosphere of Mars and its ionopause (Nagy et al. 2004). Earlier studies show that the crustal magnetic fields can contribute to irregularities in the ionosphere of Mars (Gurnett et al. 2005; Duru et al. 2006). They can also affect the electron distribution and have the effect of raising the boundary between Mars' ionosphere and solar wind. Crider et al. (2002) and Brain et al. (2005) showed that the strong crustal magnetic fields raise the altitude of magnetic pile-up

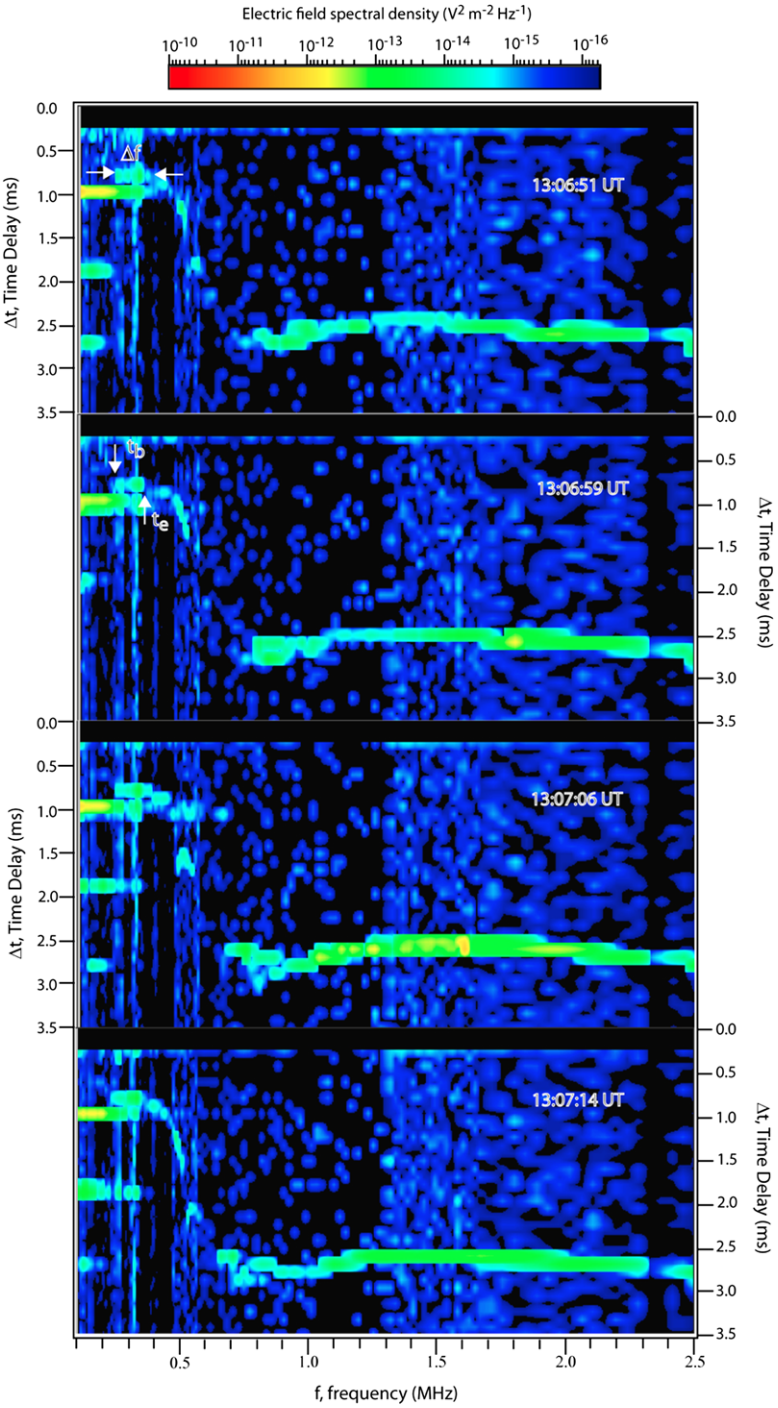

Fig. 18 Ionograms around an ionopause-like signature (Duru et al. 2009)

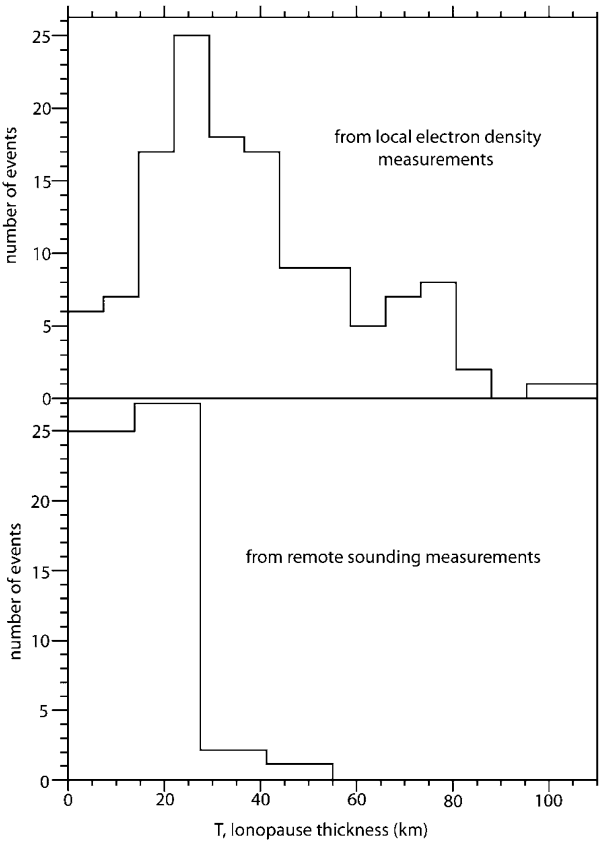

Fig. 19 Distribution of density drop thickness calculated from local n_e measurements (*above*), and remote sounding (*below*) (Duru et al. 2009)

boundary (MPB). Duru et al. (2009) studied the influence of the magnetic crustal sources on the n_e drop location and found that drop altitudes are higher over crustal field regions.

3 Venus

Current knowledge of the solar wind interaction with Venus comes from Venera-9 and Venera-10 measurements (Gringauz et al. 1976; Dolginov et al. 1981; Vaisberg et al. 1976; Zelenyi and Vaisberg 1985), and in much broader extent from the long lasting Pioneer Venus Orbiter (1978–1992) which provided a data set that extended over a complete solar cycle (Russell et al. 2006a). The plasma boundaries at Venus were analyzed using data measured by the PVO magnetometer OMAG (Russell et al. 1980) and plasma analyzers, notably, Orbiter Retarding Potential Analyzer ORPA (Knudsen et al. 1979) because of its higher time resolution.

However, compared with the magnetometer MAG (Zhang et al. 2006) and the ASPERA-4 plasma analyzer Barabash et al. (2007) onboard the Venus Express (VEX) spacecraft PVO had much lower temporal, energy and angular resolution.

Although PVO made observations over the entire solar cycle, no direct measurements of the near Venus plasma environment during solar minimum were possible due to the high PVO orbital altitude (>2000 km) at that time. The VEX spacecraft has a constant periapsis

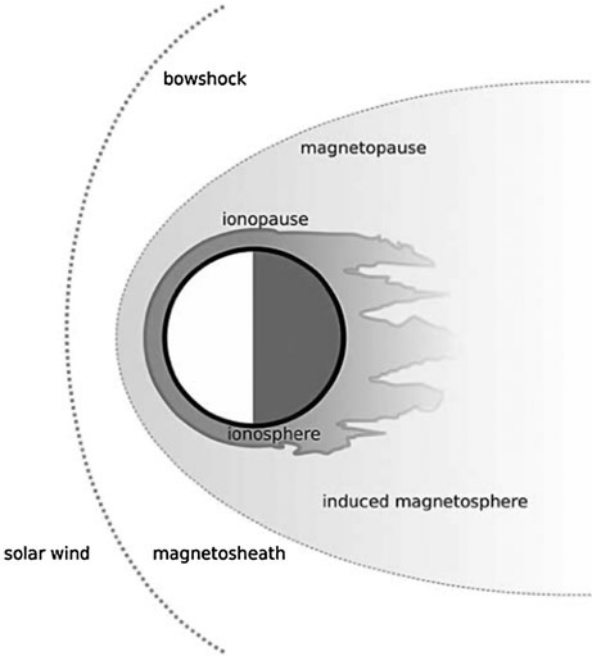

Fig. 20 Schematic of Venus induced magnetosphere and its boundaries (Zhang et al. 2008b)

altitude of about 250 km and thus can sample this region during solar minimum. Just prior to PVO arrival, the Russian Venera 9 and 10 orbiters (1975–1976) observed the Venus solar wind interaction, including the bow shock and tail during solar minimum (Verigin et al. 1978).

Venus' magnetosphere is comparatively smaller than Mars' and proven to be strongly dependent on the Solar cycle phase. It is preceded by a collisionless bow shock that heats, decelerates and compresses the solar wind flow (Fig. 20). Inside the shock, the magnetosheath is characterized by a magnetic field and plasma variability that depends on the IMF cone angle. At the bottom of the magnetosheath, on the dayside, the magnetic field pileup increases (usually gradually) and a magnetic barrier forms. A boundary similar to the Martian IMB marks the entry into the induced magnetosphere, where strong, draped fields coexist with an electron population which is significantly colder than that within the magnetosheath (the plasma mantle). The IMB extends to at least 11 planetary radii downstream and encircles the induced tail where planetary plasma escape is concentrated. The ionospheric boundary is the ionopause, where the thermal ionospheric pressure balances the induced magnetosphere's magnetic pressure. During periods of high solar wind dynamic pressure the shielding effect of the ionopause is diminished and the ionosphere gets magnetized.

3.1 Bow Shock

In the same way as Mars, the interaction between the supermagnetosonic solar wind and the Venusian atmosphere generates a bow shock. Unlike Mars, however, the Venusian bow shock has been investigated over several years by PVO and VEX, leading to an understanding of the influence of the solar wind parameters (depending on the solar cycle phase) on its structure and variability.

As for Mars, ultra low frequency waves at the proton cyclotron frequency in the spacecraft rest frame are also present in the solar wind upstream from the Venusian bow shock (see

companion paper by Delva et al. for more details). However, the smaller extent of Venus' exosphere might lead to a pick up wave corona less extended than the Martian one. In addition, waves related to solar wind backstreaming ions within the planet's foreshock are also present (Wei et al. 2011).

The Venusian bow shock has been systematically observed by all missions so far. Figure 21 shows five crossings of the Venusian bow shock as seen by PVO magnetometer ordered according to increasing plasma beta from top. As shown in the figure, the bow shock is characterized by a strong jump in the magnetic field strength and variability. These features are confirmed by VEX magnetometer (Zhang et al. 2008a). In general, Venus bow shock ramp is more clearly detected than at Mars. This might be a result—at least—of a less important role of the exospheric massloading in the case of more massive Venus. Also, the relatively higher size of the Venusian obstacle and the smaller gyroradii due to a stronger IMF attenuates the kinetic effects believed to be dominant at Mars.

Most of the crossings shown in the figure are quasi-perpendicular and depict the typical substructures arising in supercritical cases: a shock foot, ramp and overshoot. However, well-developed overshoots as the ones in panel 2 and 3 from bottom are rare in PVO measurements. As observed in other planets, the overshoot magnitude seems to increase with increasing M_{MS} (Russell and Vaisberg 1983).

More recently, VEX ASPERA-4 (Barabash et al. 2007) provided high time resolution plasma observations which confirmed the characteristics of a fast shock. Figure 22 displays data obtained on July 15, 2006 showing the main plasma features of the solar wind interaction with Venus about one hour before and after the closest approach of orbit No. 85. The top panel shows an energy spectrogram of measured electrons in the energy range of 0.1 eV–20 keV obtained by ELS. But electrons below 5 eV are reflected to avoid saturation of the counters. The sensor has 16 anodes covering a total field of view of $4° \times 360°$. Shown are counts obtained during 4 s sampling intervals integrated over anodes 5–15 of the sensor because anodes 0–4 are noisier. The data shown in the next two panels represent protons and heavy ions, respectively, measured by IMA, integrated over all 16 anodes and separated into 8 spatial sectors covering a total field of view of $90° \times 360°$. Note that signatures above 50 eV energy in the bottom panel in the solar wind and magnetosheath regions are not caused by heavy ions but by saturation of the proton channels. A spatial scan during 192 s by electrostatic deflection produces the repeatable pattern visible in the spectrogram. The x-axis shows the distance, position and time of the spacecraft along the orbit. First, VEX is located inside the solar wind before crossing the bow shock (BS) at 01:15 UT, identified by an increase in counts of energetic electrons ($E > 35$ eV) in the magnetosheath with respect to the solar wind. Passing the BS, the spacecraft enters the magnetosheath, characterized by the shocked, slowed down and heated solar wind. These signatures are concurrent with an increase in the magnetic field strength (Zhang et al. 2008a). Bow shock's averaged shape, size and controlling factors are covered in Sect. 3.4.2, where they are compared with the IMB.

3.2 Magnetosheath

Venus magnetosheath's size is comparatively larger in terms of gyroradii than that of Mars. Therefore, the solar wind and planetary plasma has more room to properly thermalize within the shock. This thermalization is achieved among other processes via the action of plasma waves which are usually observed in this region.

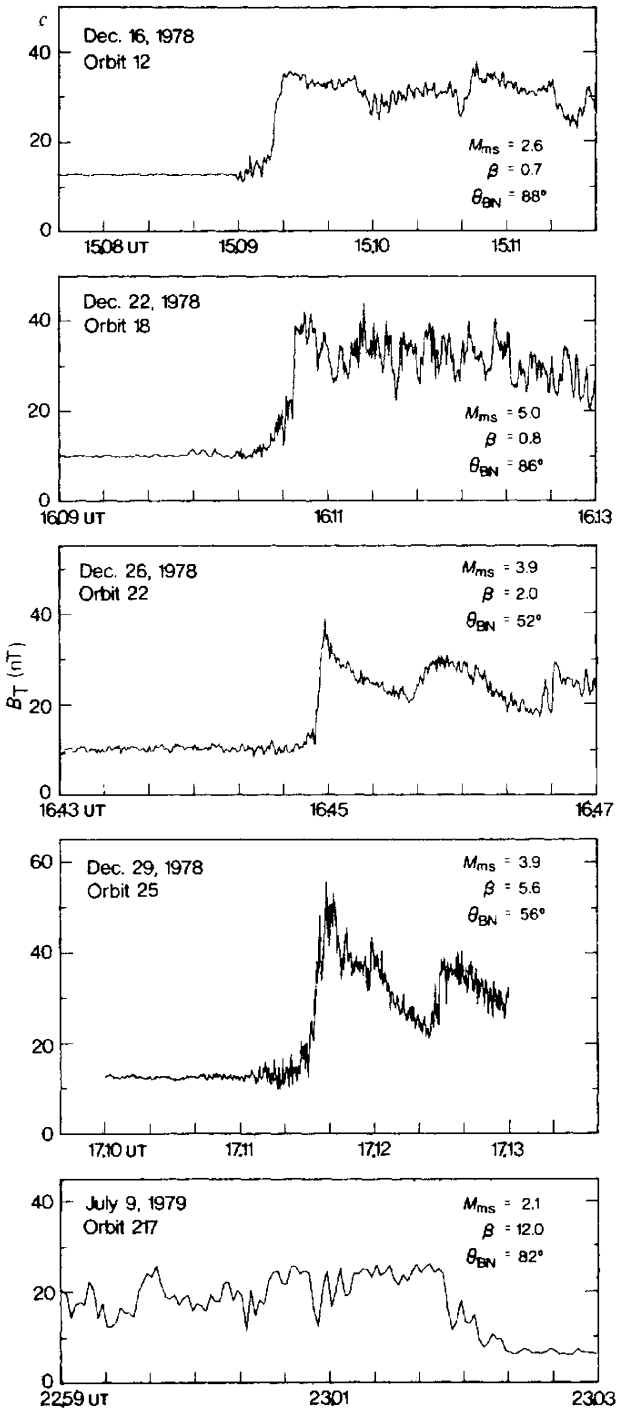

Fig. 21 Magnetic field strength profiles of the Venusian shock for different magnetosonic Mach numbers, shock normal angles, and plasma beta (Russell and Vaisberg 1983)

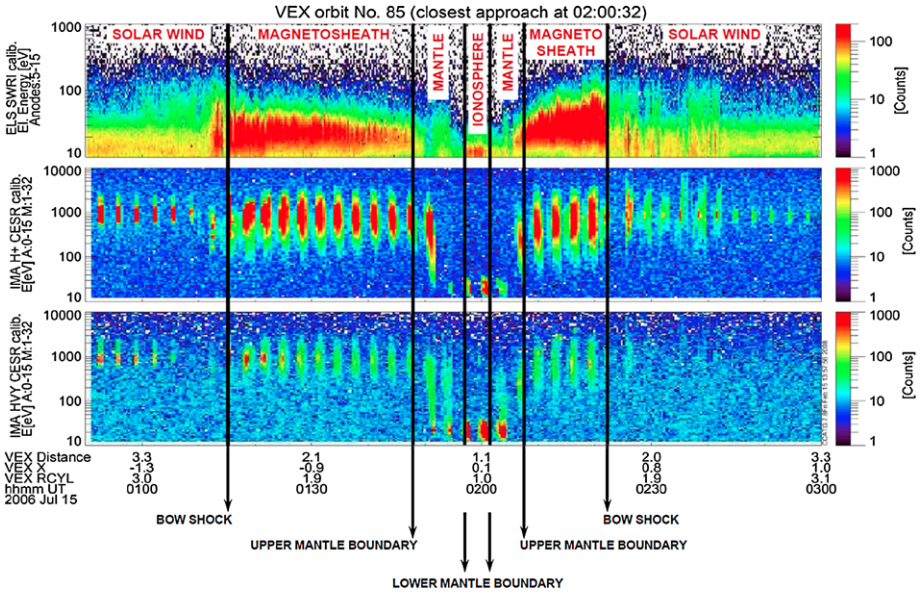

Fig. 22 ASPERA-4 data recorded on July 15, 2006—about an hour before and after the pericenter of that orbit. The *top panel* shows the total counts of energetic electrons measured by the ELS sensor and the two panels below presents the total counts of the proton and heavy ion channels of the IMA sensor, respectively. The heavy ion channel contains proton counts whenever the proton channel saturates. The *black vertical arrows* mark the plasma boundaries separating the different interaction regions (solar wind, magnetosheath, mantle and ionosphere)

The Venusian magnetosheath has been explored in the past by spacecraft Venera 9, 10, and PVO leading to several works on its properties. In particular, a complete review on these observations can be found in Phillips and McComas (1991). Important results obtained by these missions include the dependence of the magnetic field fluctuation level upon the shock normal angle. Luhmann et al. (1983) reported that the magnetic field downstream from a quasi-parallel bow shock fluctuated more intensively. Oscillations with a frequency of 0.05 Hz observed in the magnetosheath were believed to be foreshock waves convected through quasi-parallel shocks (Hoppe and Russell 1982). Also, waves at the proton cyclotron frequency (locally generated, likely) were reported by Russell et al. (2006b).

More recently, VEX identified mirror mode waves in the Venusian magnetosheath (Volwerk et al. 2008), an observation similar to that reported in other magnetospheres, notably Mars (Bertucci et al. 2004). Wavelet analysis also revealed Vörös et al. (2008) found $1/f$ fluctuations, large-scale structures near the terminator and more developed turbulence further downstream in the wake.

The nature of the waves observed within the magnetosheath depending on the shock angle was revisited by Du et al. (2009), who reported that the strength and properties of the fluctuations are strongly controlled by the IMF cone angle: whereas there fluctuations behind a quasi-parallel bow shock are quite strong and turbulent (probably convected foreshock waves), those behind a quasi-perpendicular shock are more coherent, and probably locally generated.

3.3 The Induced Magnetosphere Boundary

3.3.1 Identification and Structure

The existence of a boundary marking the entry into Venus' induced magnetosphere has been under discussion, the main reason being the absence of simultaneous three-dimensional magnetic field measurements and high resolution superthermal and cold plasma measurements. The availability of those measurements combined led to the identification of its main features, which are somehow similar to those listed in the Martian case:

(a) A (sometimes sharp) increase in the magnetic field strength by a factor of 2–3.
(b) Decrease in the magnetic field fluctuations.
(c) Enhancement of the magnetic field draping.
(d) Decrease in the temperature of electrons.
(e) Decrease in the solar wind ion (H^+ and He^{++}) densities.

The increase in the total density reported at Mars is likely to occur at Venus too, but has not been measured so far.

At Venus, the increase in the magnetic field strength that ultimately forms the so-called magnetic barrier is usually gradual. The apparent lack of a sharp jump in the magnetic field strength in PVO OMAG measurements then led to 'ad hoc' IMB definitions based on magnetic pressure (Zhang et al. 1991) which were extremely useful to provide a first estimation of its location on the dayside.

However, more recent analyses of PVO data report that sharp jumps are often observed on the magnetic field strength. Figure 23 shows magnetic field profiles in VSO coordinates in the vicinity of the Venusian IMB. In the Venus-Sun-Orbital (VSO) coordinate system, the positive X_{VSO}-axis points from the center of Venus to the Sun (opposite to the solar wind bulk velocity), the positive Y_{VSO}-axis points opposite to the heliocentric orbital motion of Venus, and the Z_{VSO}-axis completes the right-handed system pointing towards the ecliptic north. Figure 23a shows a profile obtained by PVO OMAG displaying a factor 2–3 jump on $|B|$ similar to the Martian IMB (Bertucci et al. 2003b). Figure 23b shows magnetic field measurements obtained by VEX MAG, revealing a gradual pileup (Zhang et al. 2010). In the second example, the IMB is identified from the stoppage of the magnetic field variability.

In the downstream sector, the IMB as the magnetic tail boundary was easily identified from the onset of a nonzero value for $|B_{\mathrm{XVSO}}|$ (Saunders and Russell 1986). However at the time of PVO it was unclear weather the magnetic tail boundary had a dayside counterpart—although certain works like Vaisberg and Zeleny (1984) postulated it. More recently, and following the identification criteria of the Martian IMB by MGS (Bertucci et al. 2003a), Bertucci et al. (2003b) found that the dayside Venusian IMB could be detected from the enhancement of the IMF draping. In a follow-up work Bertucci et al. (2005a) reported that at also at Venus, the IMB structure can manifest itself a boundary with properties comparable to a tangential or a rotational discontinuity depending on the magnitude of the magnetic field component along the minimum variance direction. With the arrival of VEX, Zhang et al. (2008b) systematically identified the Venusian IMB (which is referred to it as 'Magnetopause') as the place where the magnetosheath oscillations stop. The crossings identified in this way were also analyzed using minimum variance analysis and an influence of the direction of the IMB on the normal component of the magnetic field at the boundary location was found.

Induced magnetosphere boundary in downstream region was identified in Venera-9 and Venera-10 data by change of mean ion energy and ion temperature accompanied by change

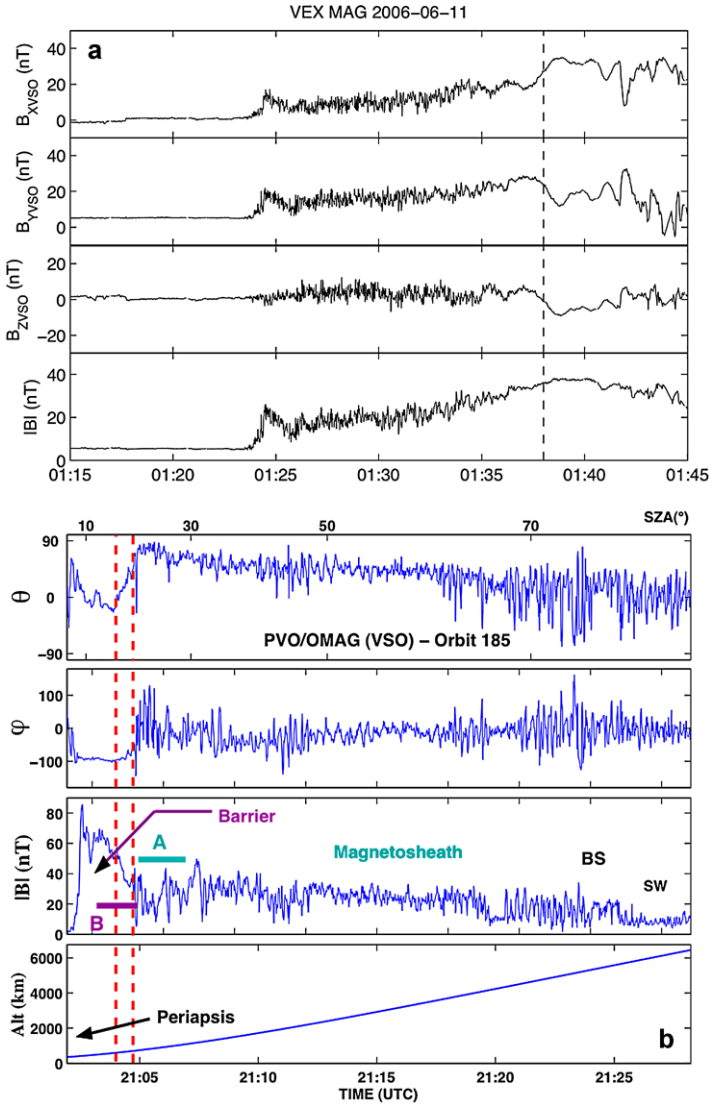

Fig. 23 Magnetic field measurements around Venus in VSO coordinates during an inbound VEX pass (*left*) and an outbound PVO orbit leg (*right*) showing, respectively, a gradual and an abrupt magnetic field pileup. In the first case the IM's (*shaded area*) outer boundary (around 0138 UT) is defined from the stoppage in magnetic field fluctuations (Zhang et al. 2008a), the jump observed in the PVO magnetic field strength a few minutes around 2105 UTC (*red dash lines*) coincides with the stoppage of the fluctuations in the magnetic field direction (Bertucci et al. 2003b)

of magnetic field fluctuations frequency (Vaisberg et al. 1976, 1995). The changes in the spectra of superthermal electrons at the IMB were studied by Spenner et al. (1980), who defined, in the downstream sector a very broad transition zone called 'mantle' where the spectra shape was between that of the magnetosheath (referred to it as ionosheath) and that of the ionosphere. As a result, the so called 'ionosheath boundary' would be the place where

the superthermal electron spectra of the magnetosheath starts to cool down, i.e., a typical signature of the IMB. As a result, the mantle would be co-located with the induced magnetosphere proper.

More recently, Martinecz (2008) and Martinecz et al. (2008, 2009) using VEX ASPERA-4 data and following Spenner et al. (1980) criteria, identified the upper and the lower limits of the Venusian mantle (UMB and LMB), which correspond to the IMB and the ionopause, respectively.

Figure 20 also shows the boundaries and regions inside the Venusian bow shock. At 01:48 UT, VEX crosses the upper mantle boundary (UMB), identified by a strong decrease in electron counts ($E > 35$ eV), and is located in a so-called mantle region or transition zone, where a mixture of solar wind protons and planetary ions is observed. The LMB, crossed at 01:57 UT, is also called Ion Composition Boundary (ICB), because at this boundary the solar wind protons disappear and the planetary ions become the main population. The LMB is identified in ELS by the appearance of ionospheric photoelectrons ($E > 10$ eV). Below the LMB, the spacecraft is located in the ionosphere between 01:57 UT and 02:01 UT. On the outbound pass, VEX crosses again all the mentioned plasma regions and boundaries, but in reverse order, i.e., at 02:01 the LMB, and at 02:08 UT the UMB.

3.3.2 Comparison of Venusian IMB and Bow Shock Sizes, Shapes and Controlling Factors

Russell et al. (1988) and Zhang et al. (1990) investigated the Venus bow shock based on nearly 2000 PVO shock crossings and found that the shock location is modulated by the solar cycle and solar EUV flux, the upstream solar wind parameters and the orientation of the IMF (see also Phillips and McComas (1991) and Russell et al. (2006a)). For modeling the bow shock they have used a simple conic section with its focus at the center of the planet based on PVO data.

More recently, Martinecz et al. (2008) used a 3-parameter fit based on ASPERA-4 measurements to achieve a more realistic shape of this boundary. The same technique, i.e., a conic fit with conic focus along the Sun-planet line as a third free parameter, has already been used by Slavin et al. (1980) based on PVO data and was later applied to Mars by Vignes et al. (2000). From 14 May 2006 to 31 December 2007, 817 Venusian BS crossings, 842 UMB crossings and 798 LMB (ICB) crossings were identified in ELS and IMA data as described above. For the bow shock the curve fitting technique developed by Slavin and Holzer (1981) was applied. This technique has also been used by Trotignon et al. (2006) for modeling the plasma boundaries at Mars. The observed shock locations have first to be transformed into an aberrated solar ecliptic system (X_0, Y_0, Z_0; VSO), assuming a 5° aberration. Then, a conic function in polar coordinates, assuming cylindrical symmetry along the X_0-axis, is least-square fitted to the observed BS positions. In order to get the best fit to the observations an offset of the conic focus along the symmetry axis was used (Slavin et al. 1980). Thus, the shock surface is represented by the following equation where the polar coordinates (r, θ) are measured with respect to a focus located at $(x_0, 0, 0)$. L is the semi-latus rectum and is the eccentricity (see Table 1).

For modeling the positions of UMB and LMB Martinecz et al. (2008) used a somewhat different approach, as the observations on the dayside and on the nightside cannot be represented by single conic functions. This was also noted in the case of the magnetic pile-up boundary (MPB) at Mars (Trotignon et al. 2006). Thus, circular fits for the dayside observations ($X_0 > 0$) and linear regressions ($y = k \cdot x + d$) for the nightside measurements ($X_0 < 0$) were used in order to model the mantle boundaries (see Table 2). The absence of data for the mantle region below about 50° SZA results in boundary fits which are too far

Table 1 Venusian BS fit parameters from ASPERA-4/VEX in comparison with Venera 9/10 (Slavin et al. 1984), PVO (Russell et al. 1988; Zhang et al. 1990) and MAG/VEX (Zhang et al. 2008a) results at solar minimum. L, x_0, ε and r_{tsd} are the semi-latus rectum, eccentricity, conic focus and terminator shock distance, respectively (Martinecz et al. 2008)

	$L\ [R_V]$	ε	$x_0\ [R_V]$	$r_{\mathrm{tsd}}\ [R_V]$
Martinecz et al. (2008)	1.515	1.018	0.664	2.088
Slavin et al. (1984)	1.68	1.03	0.45	2.096
Russell et al. (1988)	2.14	0.609	0.0	2.14
Zhang et al. (1990)	2.131	0.66	0.0	2.131
Zhang et al. (2008a)	2.14	0.621	0.0	2.14

Table 2 UMB and LMB fit parameters from ASPERA-4/VEX at solar minimum (Martinecz et al. 2008)

	Upper mantle boundary	Lower mantle boundary
Circular fit	$r_{\mathrm{UMB}} = 1.130 R_V$	$r_{\mathrm{LMB}} = 1.076 R_V$
Linear regression	$k_{\mathrm{UMB}} = -0.101 R_V$	$k_{\mathrm{LMB}} = 0.122 R_V$
	$d_{\mathrm{UMB}} = 1.130 R_V$	$d_{\mathrm{LMB}} = 1.076 R_V$

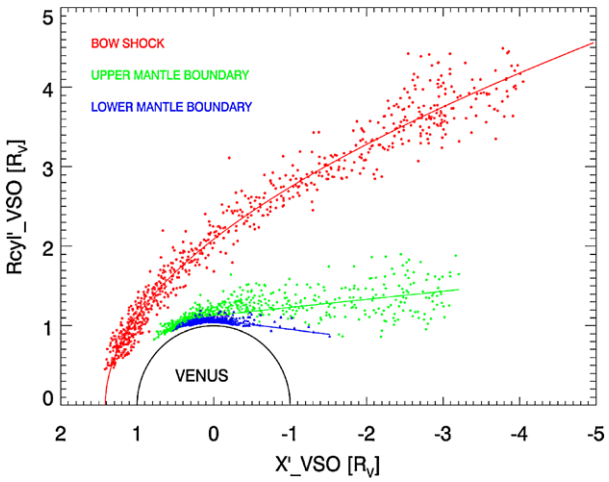

Fig. 24 Axisymmetric bow shock (BS), upper (UMB) and lower (LMB) mantle boundary fits derived using the first 19 months of ASPERA-4 observations in an aberrated VSO coordinate system. The BS crossings (*red circles*) were fitted to a conic function. The UMB (*green diamonds*) and LMB (*blue triangles*) crossings were fitted by a circle on the dayside and by linear regression on the nightside (from Martinecz et al. 2008)

away from the planet on the dayside. More realistic mantle fits will require crossings in the subsolar region, expected later during the VEX mission.

Figure 24 displays the axisymmetric BS, UMB and LMB (ICB) fits derived using the first 19 months of ELS and IMA observations in aberrated VSO coordinates (Martinecz et al. 2008).

Influence of the Solar Wind Dynamic Pressure Martinecz et al. (2008) also studied the variation of the BS position at the terminator as a function of the solar wind dynamic pressure (Fig. 25). All BS crossings (blue plus signs) were extrapolated to the terminator plane

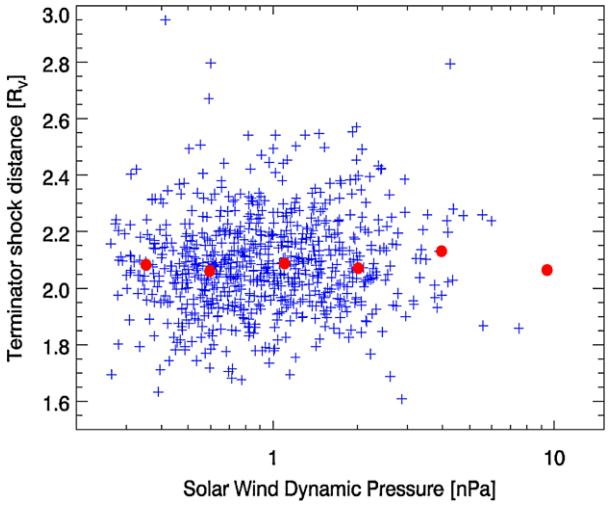

Fig. 25 The dependence of the bow shock position at the terminator on the dynamic pressure of the solar wind derived from ASPERA-4 measurements. All bow shock crossings (*blue plus signs*) were extrapolated to the terminator plane using a conic section curve with a fixed eccentricity ($\varepsilon = 1.018$) and a fixed focus ($x_0 = 0.664$) and with a variable semi-latus rectum. No normalization has been applied to the data. The *red points* represent median values over pressure bins (from Martinecz et al. 2008)

using a conic section curve with a fixed focus ($x_0 = 0.664$) and eccentricity ($\varepsilon = 1.018$) and a variable L value as follows:

$$L = \sqrt{(X' - x_0)^2 + Y'^2 + Z'^2 + \varepsilon \cdot (X' - x_0)}$$

Then the terminator shock distance is given by

$$r_{\text{tsd}} = \sqrt{(L \cdot (L + 2 \cdot \varepsilon \cdot x_0) + x_0^2 \cdot (\varepsilon^2 - 1))}$$

The red points in Fig. 25 represent median values over pressure bins and demonstrate clearly the independence of the BS position from the ram pressure during solar minimum conditions. This finding is in agreement with results obtained by Russell et al. (1988) and by Zhang et al. (2004) based on PVO observations.

Influence of the EUV Flux/Solar Cycle PVO observations revealed that the solar wind interaction with Venus is very dependent on the phase of the solar cycle (Russell et al. 2006a). During solar minimum the BS is found to be closer to the planet than during solar maximum due to lower ionization and ion pickup rates caused by EUV flux changes over the 11-year solar cycle. A comparison between the terminator BS position r_{tsd} and solar EUV flux (F50 index: 0.1–50 nm integrated photons $\text{cm}^{-2}\,\text{s}^{-1}$ and shifted to Venus) derived from SOHO SEM observations shows no apparent dependence (Martinecz et al. 2008). This is probably due to the fact that the EUV flux variation is small over the period of observation, as expected for solar minimum.

Figure 26 shows Martinecz et al. (2008) VEX BS fit in comparison with other shock models based on different data sets at solar minimum. The VEX fit is in good agreement with the BS model of Slavin et al. (1984) based on Mariner 5,10 and Venera 4, 6, 9, 10 observations. They also used a 3-parameter conic section for modeling the upstream and downstream shock location which results in a hyperbola since $\varepsilon > 1$. Russell et al. (1988) investigated the Venusian BS by means of magnetic field measurements on board PVO. They fitted the dayside shock crossings by using a 2-parameter conic function where its focus is fixed at the center of the planet resulting in an ellipse since $\varepsilon < 1$. The dayside BS model from Zhang et al. (2008a), based on Magnetometer data made onboard VEX, is also obtained by using a 2-parameter conic section with a fixed focus at the center of Venus. However,

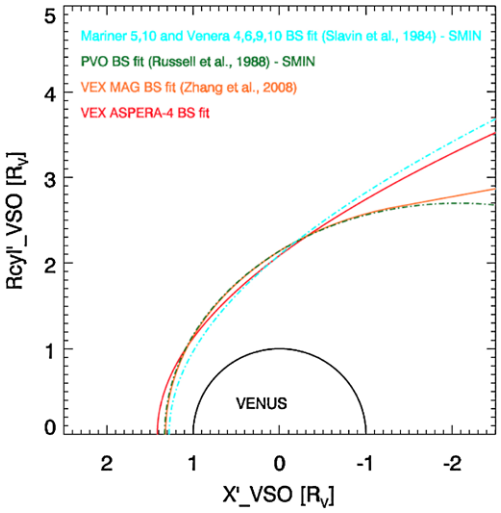

Fig. 26 This plot shows the terminator bow shock position as a function of solar EUV flux (F50 index: 0.1–50 nm integrated photons $cm^{-2}\ s^{-1}$) derived from SOHO SEM observations and shifted to Venus. All bow shock crossings (*orange asterisk signs*) were extrapolated to the terminator plane by means of the conic function

only shock crossings between and 117° solar zenith angle (SZA) were fitted, whereas the distant BS (SZA > 117°) is represented by an asymptotic shock cone determined by an average magnetosonic Mach number of 5.5 at solar minimum. Theoretically, the distant BS should be a Mach cone, but in-situ measurements made by ASPERA-4/VEX provide the counterevidence that this is not the case for the Venusian BS. The same result was found by Trotignon et al. (2006) investigating the location and shape of the Martian BS based on Phobos 2 and Mars Global Surveyor (MGS) data sets. These observations demonstrated that the far downstream BS at Mars does also not meet a Mach cone.

As for the IMB, and the ionopause, the upper and lower boundary positions of the magnetic barrier determined by Zhang et al. (2008b) based on the magnetometer observations on board VEX are only partly in agreement with Martinecz (2008) determination of UMB and LMB locations. At the terminator, the average thickness of the mantle region is around 500 km and hence, 300 km less thick than the magnetic barrier. The thickness of the magnetic barrier in the subsolar region is around 200 km (Zhang et al. 2008b) but currently it is not possible to estimate this thickness for the mantle region due to the lack of mantle crossings below around 50° SZA.

3.4 The Induced Magnetosphere

The magnetic structure of the induced magnetosphere and magnetotail of Venus was exhaustively explored by PVO (Zhang et al. 1991; Phillips and McComas 1991, and references therein) and more recently by VEX (Zhang et al. 2008b, 2010).

On the dayside, the magnetic pressure accumulates gradually inside the induced magnetosphere and generates a magnetic barrier where the plasma is progressively colder and slower as more and more planetary, recently-ionized particles join the flow. As a result, the magnetic pressure term is likely to be dominant in this region. It is still uncertain, however, if the increase in magnetic pressure is associated with a plasma depletion of the piled up flux tubes, as postulated by Zwan and Wolf (1976). High-resolution thermal plasma density measurements within the IM at Mars and Titan (and not available around Venus so far) indicate that flux tubes might be filled with cold planetary plasma and therefore the depletion effect would only be applicable to solar wind plasma.

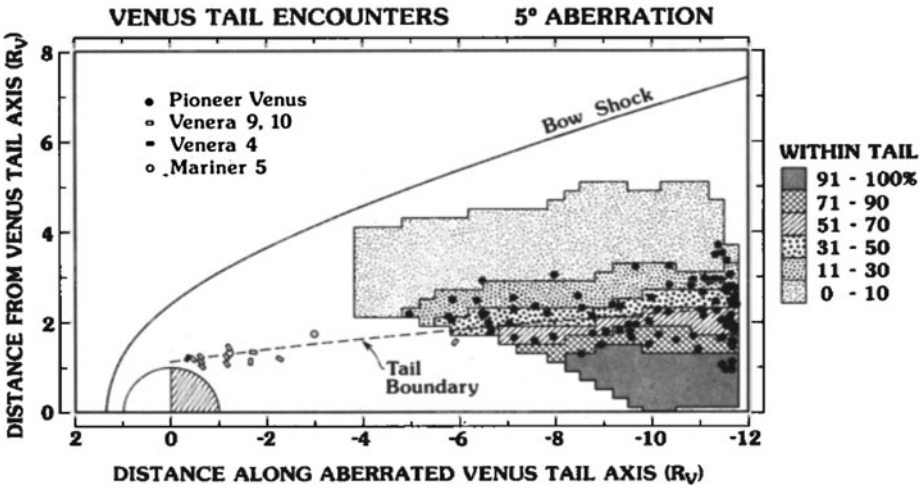

Fig. 27 The average size of Venus magnetotail in aberrated cylindrical VSO coordinates (Saunders and Russell 1986). Note that no dayside counterpart is assumed for the tail boundary (IMB) as such counterpart had not been identified from magnetic field data

Fig. 28 Magnetic field polarity in magnetic coordinates (cross tail component points in the $+y$ direction) in the distant magnetic tail of Venus (Saunders and Russell 1986). The *ellipse* marks the average tail boundary

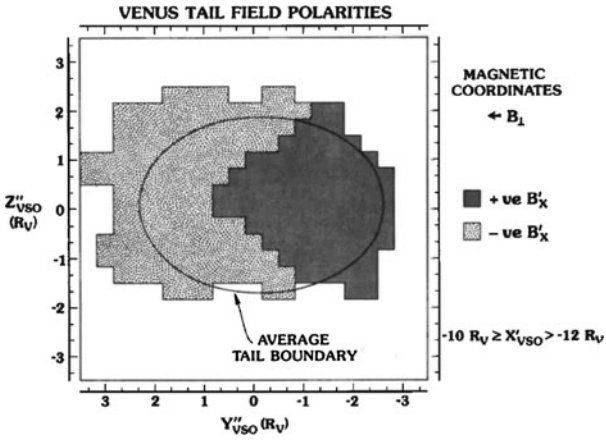

In the post terminator region, pressure balance is replaced by a stress balance as field lines become draped. This stress becomes important near the magnetic poles, where $\mathbf{J} \times \mathbf{B}$ force can be efficient in transporting the local plasma across the terminator (Pérez-de-Tejada 1986).

PVO and VEX explored Venus magnetotail in a complementary way. Whereas VEX explored the short-mid ($1.3 > R > 3R_V$) range tail (Zhang et al. 2010), PVO characterized its topology close ($R < 3R_V$) and far ($5 < R < 12R_V$) from the planet (Saunders and Russell 1986; Phillips and McComas 1991).

PVO measurements showed that the although its location is deduced statistically, the IMB/Tail boundary is well defined up to $12R_V$ (Fig. 27) and displays properties of a rotational discontinuity, which may allow the exchange of plasma with the magnetosheath (Saunders and Russell 1986). On the other hand, the cross section of Venus far tail is elongated along the cross-tail component of the background magnetic field ($\mathbf{B}_\perp$) (Fig. 28).

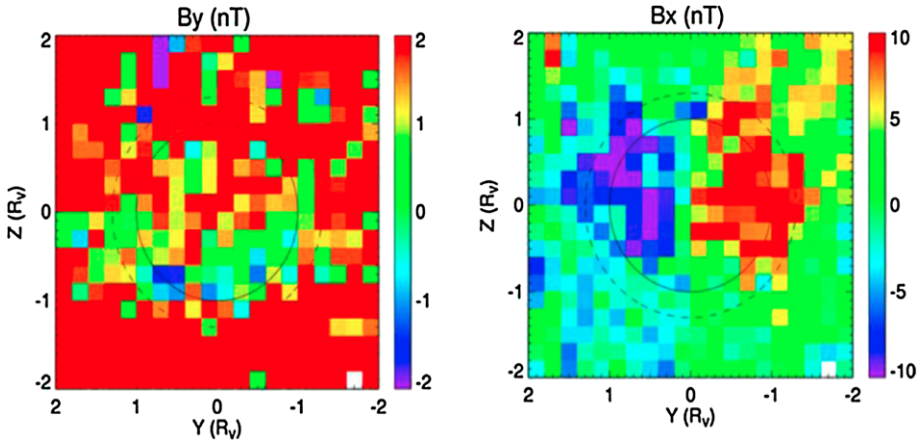

Fig. 29 (*Left*) Cross tail magnetic field component in the near Venusian tail. (*Right*) Sunward component of the magnetic field in the near Venus magnetotail. Upstream IMF points in the $+y$ direction. The view is toward the planet from the tail. The inner circle is the limb of Venus and the outer circle is the approximate magnetotail section deduced by Zhang et al. (2010). In both figures the nominal convective electric field points in the $+z$ direction (Zhang et al. 2010)

Estimates of the cross tail component $\mathbf{B}_\perp$ yielded between 2 nT (Saunders and Russell 1986) and to 4 nT (McComas et al. 1986), and more predominant on the hemisphere where the upstream convective electric field $\mathbf{E}_c = -\mathbf{V} \times \mathbf{B}$ points away from the planet. Tail fluxes were found to be of at least 3 MWb (Saunders and Russell 1986). These high values were interpreted as an indication that most of the magnetotail field lines must close across the tail rather than on the dayside, and that the induced tail is replenished with new IMF lines in only a few minutes, leading to similar transit times for field lines across the interaction region (Phillips and McComas 1991). A more recent work based on VEX MAG data (Zhang et al. 2010) also found an influence of the nominal convective electric field at lower altitudes. Figure 29 shows the cross tail and the sunward magnetic field component distributions in the near Venusian tail (Zhang et al. 2010) revealing more streamlined field lines on the outward pointing convective electric field hemisphere ($Z > 0$).

The planetary ion species dominating Venus IM include H^+, He^+, O^+, and O_2^+ (Fedorov et al. 2008). Figure 30 shows the distributions of protons (above) and heavies ($m/q > 14$, below) for energies larger than 300 eV as measured by VEX ASPERA-4 (Fedorov et al. 2008). The almost mutually exclusive contours shows the differentiation in species within the induced magnetic tail. Also, the protons at the IMB (region called boundary layer) are more energetic than those closer to closer to the magnetotail's neutral sheet. The energy of heavy planetary ions behaves similarly.

Finally, the neutral sheet hosts a thin layer of 500–1000 eV heavy ions surrounded by an envelope of H^+ and He^+ ions (Fedorov et al. 2008).

No recent attempts have been done to study the acceleration mechanisms responsible for the formation of the neutral sheet and the dynamic properties of the planetary ions inside the Venusian tail. McComas et al. (1986) used the average magnetic tail configuration to obtain plasma parameters (velocity and acceleration along the tail axis, density and temperature) from MHD and assuming conservation of the parallel component of the electric field. As a result, the authors find evidence of acceleration compatible with $\mathbf{J} \times \mathbf{B}$ force.

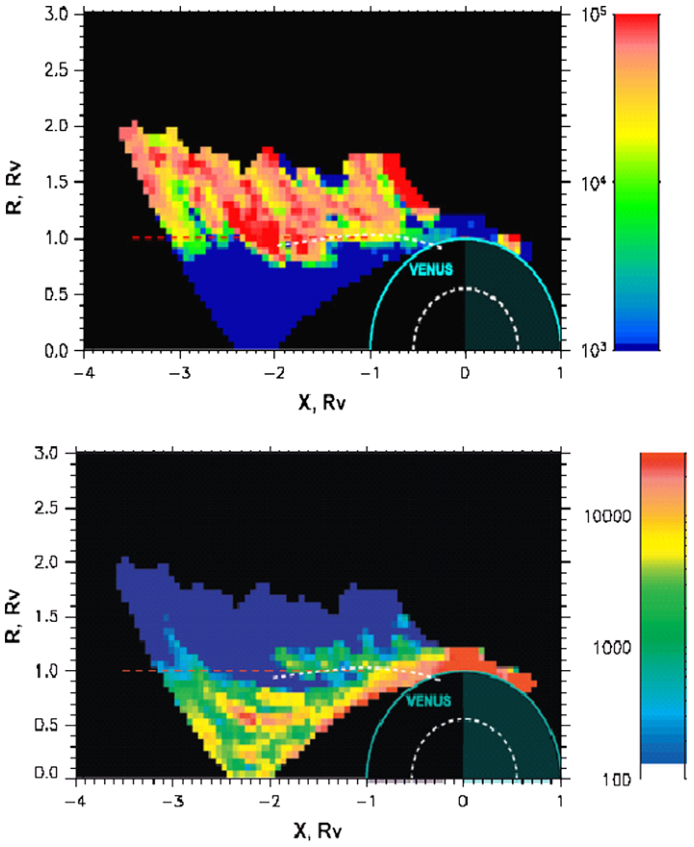

Fig. 30 (*Top*) Spatial distribution of the proton flux with energy greater than 300 eV in VSO cylindrical coordinates. The *color scale* is in arbitrary units. *Blue color* indicates zero flux. *Red dashed line* in the right panel shows the wake boundary at Venus. (*Below*) Same for planetary ions with mass per charge ratio >14 (Fedorov et al. 2008)

Finally, evidence for substorm-type tail reconfiguration likely associated with bulk plasma loss processes was recently presented from VEX data (Volwerk et al. 2009). Unlike Mars, reconfigurations at Venus occur in response to changes in the IMF.

3.5 The Ionospheric Boundary: Ionopause, Photoelectron Boundary

The Venusian ionopause is a well-defined boundary that marks the upper limit of the ionosphere—defined as the region inaccessible for external plasma (Brace et al. 1980).

The Venusian dayside ionopause is characterized by an abrupt change on the plasma density. The thermal plasma measurements required to measure such density changes were provided by the PVO Electron Temperature Probe and ORPA (Brace et al. 1980; Knudsen et al. 1982), but similar measurements are unfortunately not available on VEX.

PVO measurements reveal that during solar maximum, the altitude of the dayside ionopause and increases with SZA, from ~300 km near the subsolar point to ~900–1000 km at the terminator. The variability of its altitude also displays similar trend with respect to SZA.

The ionopause is also defined as the boundary where the magnetic pressure in the magnetic barrier is balanced against the thermal pressure within the ionosphere. As a result, it is also characterized by a strong drop in the magnetic field strength. In particular, the altitude of the dayside ionopause was found to increase with decreasing solar wind pressure (Elphic et al. 1980). Also, during periods of high solar wind pressure, the ionospheric thermal pressure is not able to withstand the magnetic pressure at higher altitudes and then the IMF diffuses within the ionosphere.

The solar cycle phase has strong effects on the ionopause location. Comparisons between in situ and remote density measurements at a fixed SZA revealed that the altitude of the ionopause strongly reduced during solar minimum (e.g. Knudsen 1988) likely as a result of the reduction in the peak thermal pressure in the ionosphere.

The ionopause structure is also affected by the solar cycle. Knudsen et al. (1987) reported that at solar maximum, the ionopause density signature is rather sharp, whereas during solar minimum the density gradient is not so clearly defined.

Finally, the nightside ionopause displays a more filamentary structure (Brace et al. 1987) including features such as tail rays and plasma holes (Phillips and McComas 1991).

Local ionospheric photoelectrons were also detected around Venus (Coates et al. 2008). Although PVO Orbiter Retarding Potential Analyzer (ORPA) provided measurements of the integrated electron flux for energies below 50 eV, it did not reproduce the sharp, characteristic spectral peaks of photoelectrons (Knudsen et al. 1980). Energy photoelectron peaks are obtained from models (McCormick et al. 1976; Cravens et al. 1980). In particular, recent models (Gan et al. 1990) predicted multiple photoelectron peaks in the 20–35 eV region, which were compared with data (Spenner et al. 1997).

According to models based on data (Mantas and Hanson 1979) photoelectron signatures at Mars are originated from the ionization of O and CO_2. The presence of O and CO_2 in the Venus atmosphere results in similar ionization potentials. However, at Venus, photoelectrons are primarily produced by ionization of O, due to the lower altitude of the transition region between CO_2 and O at Venus (Schunk and Nagy 2000).

VEX ASPERA-4 electron spectrometer (ELS) detected electrons due to photo-ionization of atomic oxygen and carbon dioxide in the Venus atmosphere by solar helium 30.4 nm photons. Due to its high energy resolution ($\Delta E/E = 7\%$) ELS has been able to improve the detection of these predicted peaks (Coates et al. 2008). Figure 31 shows a time-energy spectrogram showing the counts of electrons measured by ELS for a VEX inbound pass (Coates et al. 2008). Ionospheric photoelectrons start to be observed around 0130 until 0135 UT as a horizontal line around 18 eV. During that interval, VEX altitude varied from 700 to 250 km over the north pole. The photoelectron signatures are on average located below the ionopause (Coates et al. 2008). Coates et al. (2008) also suggest that photoelectrons are likely to be observed far from Venus as a result of their transport along draped IMF lines.

4 Titan

Titan is perhaps the most complex example of the interaction between an atmospheric unmagnetized object and its plasma environment in our solar system. This is due to Titan's orbital location in the confines of Saturn's magnetosphere what makes it prone to excursions into the shocked solar wind of the Kronian magnetosheath, the variability of Saturn's multi species outer magnetospheric plasma, and the moon's complex atmospheric and ionospheric chemistry.

Measurements by Voyager and Cassini (Neubauer et al. 1984; Wei et al. 2011), confirm the absence of a permanent intrinsic magnetic field relevant to the interaction According to

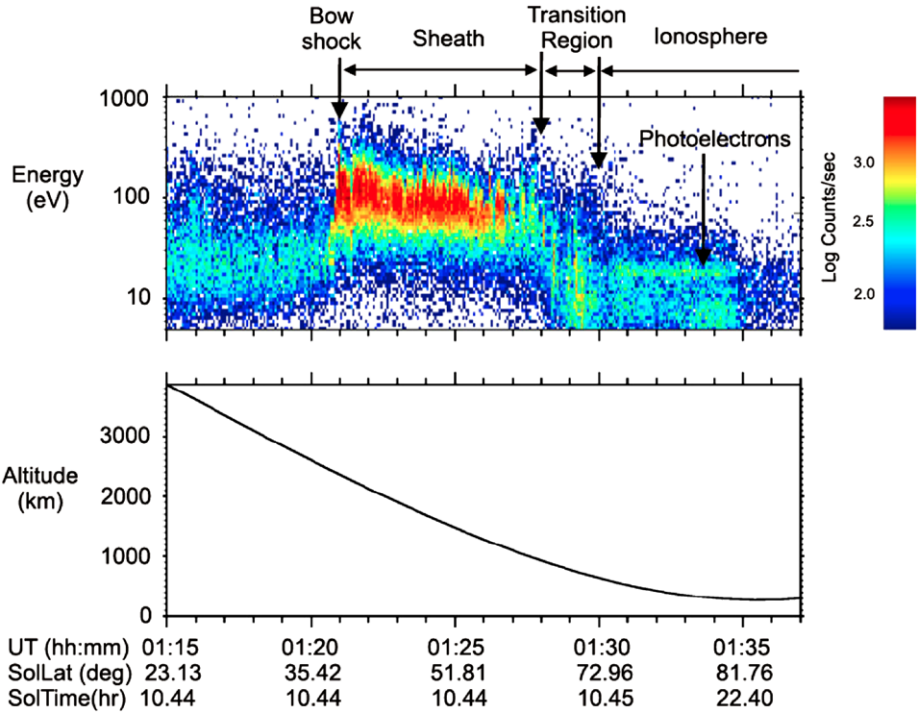

Fig. 31 VEX ELS spectrogram of electron count rate for instrument sector 11. Altitude is shown in the *bottom panel*. The photoelectron peaks are located around 18 eV between 01:30 and 01:35 UT (Coates et al. 2008)

Wei et al. (2011), the upper limit of the permanent dipole moment is 0.78 nT $\times R_T^3$. However, the possible presence of conducting layers on the surface of or within the moon (Beghin et al. 2009) and the ionosphere (Rosenqvist et al. 2009; Cravens et al. 2010b) suggest that the influence of an induced field of variable lifetime might not be negligible in the lower layers of Titan's induced magnetosphere (Wei et al. 2011).

In spite of its heliocentric distance, Titan's obstacle to the incoming plasma strongly depends on photoionization (Ågren et al. 2007). As a result, the angle between the incoming flow (i.e. Saturn's) and the EUV flux from the Sun largely controls the plasma interaction. In the ideal scenario of a magnetospheric plasma co-rotating with Saturn, the plasma flow velocity is tangent to Titan's orbit and therefore the moon's local time with respect to Saturn (Saturn Local Time or SLT) is a reliable parameter to measure the departure of the flow direction from the EUX flux. As a result, these two directions will be parallel around 18:00 SLT (a configuration similar to Mars, Venus and comets), and anti-parallel around 0600.

The first in situ observations of Titan's plasma environment were obtained by Voyager 1 spacecraft during its only flyby on November 12, 1980. The flyby occurred downstream from Titan while the moon was located at a Saturn Local Time (SLT) of 13 hs, with a closest approach distance of 2.71R_T (1R_T = 1 Titan radius = 2575 km) Voyager 1 magnetometer measurements (Ness et al. 1982) detected a well-defined induced magnetosphere with two lobes of opposite magnetic field polarity with and no influence of a significant intrinsic magnetic field. The induced magnetosphere as observed by the magnetometer coincided with a superthermal electron 'bite out' region (Hartle et al. 1982) and populated with cold

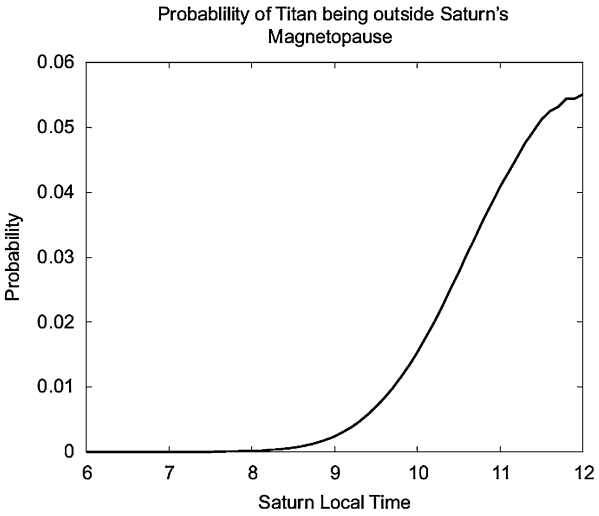

Fig. 32 Probability of Titan's orbit being outside Saturn's magnetopause as a function of SLT (Bertucci et al. 2009)

ions. These results and others are summarized in Neubauer et al. (1984). Cassini is the second spacecraft to provide in situ measurements of Titan's plasma environment. Since its arrival to the Saturnian system, Cassini performed more than 70 Titan flybys exploring Titan's induced magnetosphere at different SLT and local times with respect to the Kronian plasma flow. The latter allowed the exploration of the upstream, flank and tail sectors of the induced magnetosphere.

4.1 Titan's Plasma Context

Titan orbits Saturn at an average distance of $20.2 R_S$ ($1 R_S$ = Saturnian radius = 60330 km). Following pioneering studies on the variability of Titan's plasma environment as a result of the proximity of the Kronian magnetopause (Wolf and Neubauer 1982), a recent empirical model of Saturn's magnetopause (Arridge et al. 2006) led to a statistical study on its standoff distance based on Cassini data, which displays a bimodal stand-off distance (R_{MP}) distribution with means at 22 and $27 R_S$ (Achilleos et al. 2008). Figure 32 from Bertucci et al. (2009) shows the probability of Titan's orbit being outside Saturn's magnetopause as a function of Saturn local time based on the magnetopause stand-off distance probability function inferred in Achilleos et al. (2008). According to these results, Titan is only rarely in the shocked solar wind, however, when this happens it is exposed to a total solar wind pressure of at least 0.0345 nPa, that is approximately more than two times the average (Bertucci et al. 2008).

When inside Saturn's asymmetric disk-shaped outer magnetosphere (Arridge et al. 2008a; Khurana et al. 2009), Titan is exposed to a magnetic plasma flow displaying significant degree of non-uniformity. This results in Titan's induced magnetosphere probably rarely reaching a steady state.

Several works have addressed the variability of Titan's plasma environment. Bertucci (2009) and Bertucci et al. (2009) analyzed the strength and orientation of the magnetic field within Saturn's magnetosphere around $20 R_S$, while Arridge et al. (2008b) did a similar study from Cassini superthermal electron data. These works suggest that Titan's plasma environment is strongly shaped by the proximity of Saturn's magnetodisk. During Saturn's southern summer, the Kronian magnetodisk's central current sheet is systematically pushed

north of Titan's orbit by the solar wind. The dynamics of the disk and ultimately of Titan's plasma environment are then controlled by the solar wind pressure and the effect produced by a rotating magnetic anomaly whose phase is locked to the that of the Saturn kilometric radiation (SKR) emission. The influence of the solar wind is present at all SLT (although dominant in the noon sector), whereas the SKR modulation seems to affect the magnetic field to first-order at least in the dawn sector. Near dawn local times, Titan tends to be farther from the disk at SKR longitudes (Kurth et al. 2008) around 140° and closer to it for longitudes around 320°. Depending on these factors, Titan is exposed to either: a 'magnetodisk lobe' regime where the plasma beta and electron density are low and fields are radially 'stretched' and usually stronger, or a 'current sheet' regime characterized by quasi-dipolar, relatively weak fields and a high-beta plasma and electron density. More recently, Rymer et al. (2009) analyzed CAPS and MIMI electron spectra around Titan for all Cassini flybys until May 2009. They characterized these flybys into four categories: Plasma-sheet, Lobe-like, Magnetosheath and Bimodal. Where as bimodal spectra are associated with local water group products, an additional hot lobe-like environment is also occasionally observed and linked to increased local pick-up. Out of 54 encounters, 34 are associated with one of these groups, while the remaining ones display a combination of them. Simon et al. (2010a, 2010b) investigated the variability of Saturn's magnetic around $20.3 R_S$ and confirmed that it is strongly affected by the presence of Saturn's bowl-shaped and highly dynamic magnetodisk current sheet, In particular, Simon et al. (2010b) discriminated between real (observed by Cassini), and virtual (defined as Cassini passages within $1 R_S$ distance from Titan's orbit) flybys Among the 141 (62 real + 79 virtual) crossings of Titan's orbit between July 2004 and December 2009, only 17 encounters (9 real + 8 virtual) took place within quiet, magnetodisk lobe-type fields. During another 50 encounters (21 real + 29 virtual), rapid transitions between current sheet and lobe fields were observed around the moon's orbital plane. Most of the encounters ($54 = 22$ real + 32 virtual) occurred when Titan's orbit was within the current sheet.

Regardless of its location with respect to Saturn's magnetodisk, no bow shock has been detected around it so far. This is in agreement with the estimations of the magnetosonic Mach number (Neubauer et al. 1984, 2006).

Plasma moments also display properties different than initially expected. Cassini CAPS estimations of Saturn's magnetospheric flow velocity vector near Titan's orbit show important departures for the co-rotation direction (i.e., tangent to Titan's orbit), especially in the pre-dawn sector of Saturn's magnetosphere (Szego et al. 2007; McAndrews et al. 2009), where a significant anti-Saturn radial component is systematically found. More details on Titan's upstream plasma can be found in Sittler et al. (2010a) and Arridge et al. (this issue)

4.2 The Induced Magnetosphere Boundary

As shown by Voyager 1 and Cassini, Titan's induced magnetosphere is clearly identifiable from plasma instruments. Given the variety of plasma regimes in which Titan can be found, and the limited number of flybys for the entry into the induced magnetosphere is characterized by the following signatures:

(a) A strong change (usually an increase, especially on ram side) in the magnetic field strength.
(b) Enhancement of the magnetic field draping.
(c) Decrease in the temperature of electrons.
(d) Decrease in the external ion density and energy.
(e) Increase in the total plasma density.

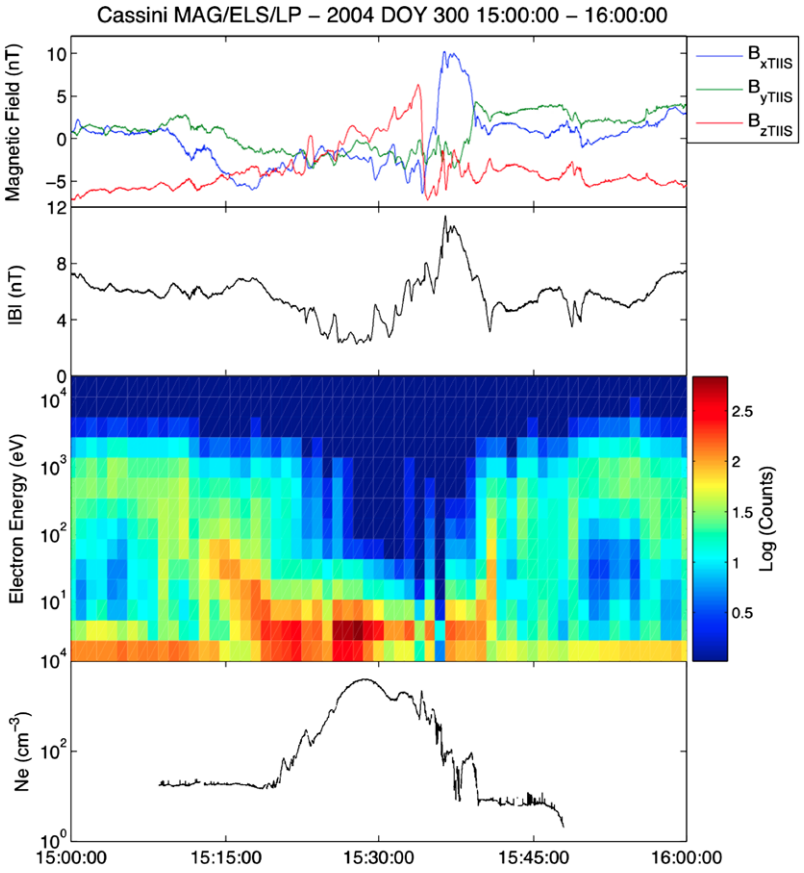

Fig. 33 From top to bottom. Magnetic field vector in TIIS coordinates and strength from MAG, 1 eV–20 KeV electron counts from CAPS/ELS (Anode 5), and electron density (n_e) from RPWS/LP during Cassini's TA encounter. Note that n_e measurements are valid only from ∼1520–1540 (Bertucci et al. 2005c)

Figure 33 shows Cassini magnetometer (Dougherty et al. 2004), CAPS/ELS electron spectrometer (Young et al. 2004), and Langmuir probe (Gurnett et al. 2004) electron density measurements during Cassini's first close encounter (TA flyby). The TA flyby occurred shortly after Cassini entered Saturn's magnetosphere (around 10.6 SLT) and as the spacecraft explored Titan's close magnetic tail from the dayside into the nightside. Cassini TA measurements have been extensively studied in several articles (special issue of Science, 308, 2005; Neubauer et al. 2006; Cravens et al. 2010b; Sittler et al. 2010a). Magnetometer (MAG) data is represented in the Titan Ionospheric Interaction coordinates (TIIS), where the X_{TIIS} axis points in the direction of the co-rotational flow, Y_{TIIS} points towards Saturn, and Z_{TIIS} points north. Closest approach occurs at 1530 UTC, downstream from the moon at an altitude of 1174 km. At both ends of the time interval, the electron distribution is unimodal centered around ∼100 and several hundred eV and the orientation of the magnetic field is mainly southward, suggesting that Titan is within Saturn's magnetodisk current sheet (Rymer et al. 2009; Simon et al. 2010a).

The inbound crossing of Titan's induced magnetosphere occurs around 1513 UTC. First, the magnetic field rotates and becomes anti-parallel to the flow as Cassini enters the 'to-

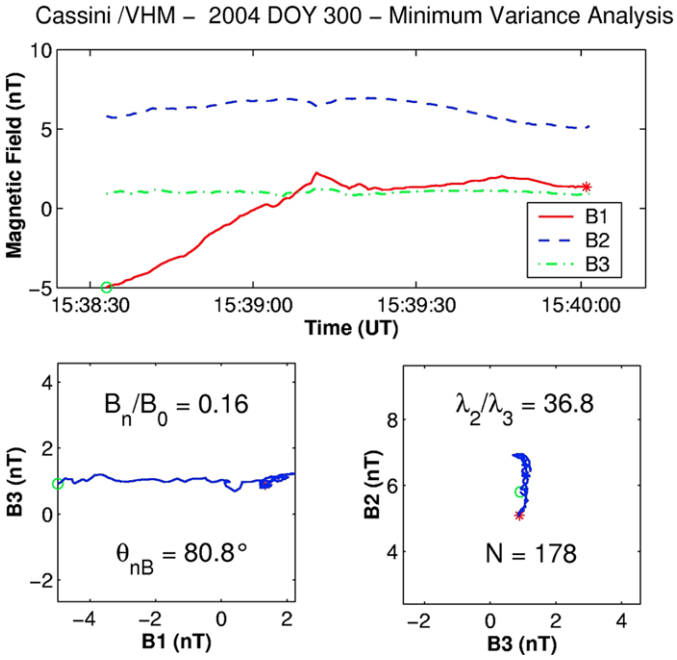

Fig. 34 *Top*: Magnetic field in along maximum (B1), intermediate (B2), and minimum (B3) variance directions across the outbound IMB crossing for TA. *Below*: hodograms indicating magnetic field trajectory on the (B1, B3) and (B3, B2) planes (left and right respectively). Also, the ratio between the normal component and the mean magnetic field strength (B_n/B_0) and the angle between the normal and the mean magnetic field vectors (θ_{Bn}) are indicated (Bertucci et al. 2005c)

ward' lobe of the induced magnetotail. Almost simultaneously, CAPS detects strong electron fluxes at decreasing energies, a signature usually associated with massloading. At the same time, locally produced photoelectrons likely start populating energy ranges inaccessible to CAPS or veiled behind the spacecraft's own photoelectron signal. The increase in the total density due to this added population is not accurately measured in the Langmuir probe data until a few minutes after the IMB crossing (around 1520), where a steep gradient is observed. Also around 1520, locally produced photoelectrons (Coates et al. 2011) start to be observed. On the outbound portion of the flyby, the IMB signatures (around 1539) are sharper. The magnetic field pileup ($|B|$ varies from ∼11 nT in the magnetic barrier to ∼5 nT after 1542) and the draping are pronounced just inside the IMB. In some flybys, the increase in pileup and draping is just inside a drop in the magnetic field magnitude (Neubauer et al. 2006). For TA this drop is evident on the outbound leg, around 1541. These drops are indeed a unique characteristic of Titan's IMB and are observed in the flanks, but not in the upstream region. As shown in Fig. 34, the rotation in the magnetic field direction from around 1539:12 is such that the component of the magnetic field normal to the minimum variance plane is negligible, suggesting that the plasma flow across the IMB might be small as for tangential discontinuities (Knetter et al. 2004). The thickness of the boundary along the normal vector is of the order of the proton inertial length (∼300 km for this flyby) (Bertucci et al. 2005c).

The signature in the superthermal electron counts is similar to that observed in the inbound leg, but sharper, and the increase in the plasma density due to the addition of cold, planetary plasma is clearly visible on the Langmuir probe data above the instrumental noise.

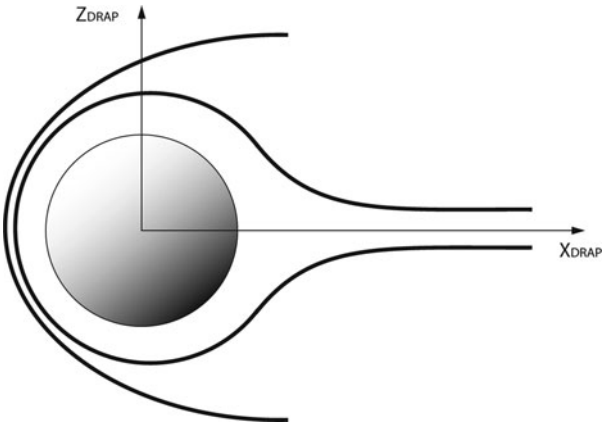

Fig. 35 Schematic illustrating reverse draped field line compared to a weakly draped one. At the flanks of the interaction, a reverse in the Z_{DRAP} component might be related to vertical plasma motion

The mean location and shape of the IMB is difficult to infer due to the variable upstream conditions. In order to compare magnetic field measurements obtained during different upstream conditions, Neubauer et al. (2006) defined the 'draping' coordinate system as follows: X_{DRAP} is along the flow direction (assumed to be perpendicular to the background magnetic field B_0), Z_{DRAP} is anti-parallel to B_0, and Y_{DRAP} completes the right-handed Cartesian system. Based on flybys Cassini MAG data for flybys TA, TB and T3, and an advanced MHD model (Backes et al. 2005), Neubauer et al. (2006) find that the IMB is much more extended on the sunward side than on the opposite side. As this effect is observed in MHD models, this might not be due to finite gyro radius effects of pick up ions (Hartle et al. 1982) but as a direct consequence of the EUV-induced ion production pattern, at least for altitudes inside the IMB. As a result, a study of the average size and shape of the IMB will have to be done from sets of flybys with similar upstream conditions including SLT, SKR phase, and Kronian season.

4.3 The Induced Magnetosphere

Titan's induced magnetosphere is characterized by draped and piled up fields whose geometry is compatible with the direction of the upstream magnetic field and velocity vectors (Ness et al. 1982; Backes et al. 2005; Neubauer et al. 2006; Bertucci et al. 2007). On the upstream side, the magnetic field displays a clear pileup of the field (Simon et al. 2008). On the downstream side, the induced magnetic tail consists of two lobes with field lines parallel and anti-parallel to the flow direction, separated by a neutral sheet theoretically lying on the (X_{DRAP}, Y_{DRAP}) plane. In the case of a Kronian north south field and flow aligned with corotation the DRAP and the TIIS coordinate system coincide.

Contrary to Neubauer et al. (2006), and in agreement with the definition for solar wind interaction, the magnetic equatorial plane will be the plane containing the upstream magnetic field and flow velocity, the (X_{DRAP}, Y_{DRAP}) plane. In general, B_x and B_y change sign when passing through this plane. It is also noted that the onset of nonzero B_y components points at nonzero Y_{DRAP} components of the flow velocity vector, as the external plasma tries to go around the obstacle. Similarly, a change in sign of B_z requires nonzero Z_{DRAP} velocity components. An interesting observation in the flanks of the interaction is the occurrence of "reverse draping" (Neubauer et al. 2006) in the case of positive components B_z in the DRAP system. In reverse draping a drop in the magnetic field strength may occur as draped field

lines become farther apart in the flanks (Fig. 35). Reverse draping is certainly an important piece in understanding the formation of Titan magnetotail's neutral sheet.

Cassini CAPS measurements reported clear signatures of massloading associated with Titan's induced magnetosphere. In a comparison between Voyager 1 and Cassini TA flybys, Hartle et al. (2006) reported a gradual decrease in the 14–16 amu ion energies above the inbound IMB crossing for TA, while energies drop by a factor of 125 in these ions. The authors point out that such a decrease is attributed to the increase in the density—actually observed by RPWS/LP (Wahlund et al. 2005)—and the onset of a strong ion massloading by heavy ions (especially 28 amu ion N_2^+), as exospheric densities start to be dominated by CH_4 and N_2. Other locally pick up species are H^+, H_2^+, probably responsible for the light massloading outside the IMB.

An interesting aspect of Titan's heavy massloading is the low plasma velocities within the IM—Hartle et al. (2006) during TA reports values of the order of 10–15 km/s. Extraordinary evidence of this effect on the transport of draped magnetic flux tubes is provided by the detection of draped magnetic field lines within the IM which correspond to background conditions the moon was exposed to long before the encounter. These fields were named 'fossil fields' because of the analogy to fossil records (Neubauer et al. 2006). Confirmation of the existence and timing of fossil fields were obtained in Titan's first observed excursion into the Kronian magnetosheath during the T32 encounter (Bertucci et al. 2008). Figure 36a shows Cassini MAG data in spherical Kronian magnetic coordinates for the day of the encounter (13 June, 2007). The angle λ is the magnetic latitude and the azimuth ϕ is measured on the magnetic equatorial plane from the sunward direction. Prior to the encounter and as it travels outbound from Saturn, Cassini experiences a nearly 10-hour excursion into the magnetosheath followed by a $\sim$3 hour period within the magnetosphere. Since before the encounter, Cassini's Kronocentric distance is smaller than Titan's, it is reasonable to think that Titan was respectively in the solar wind and the magnetosphere for a similar amount of time. The T32 encounter takes place within the magnetosheath 20 minutes after the third magnetopause crossing (c). Figure 36b shows the magnetic field in spherical TIIS coordinates, RPWS/LP and CAPS/ELS measurements in the vicinity of the encounter, which takes place around 13.6 hours SLT as Cassini flies over the moon's north pole at a minimum altitude of 975 km. The direction of the interplanetary magnetic field surrounding Titan's induced magnetosphere is clearly northward. The IMB is clearly detected around 17:41 and 17:53 (altitudes of 1400 and 1740 km, respectively), where the 100–1000-eV electron count rates suddenly drop showing a strong acceleration of the external flow is strongly decelerated. Around those times, the cold plasma starts to dominate as the plasma density increases above 100 cm^{-3}. As a result of this increase, the ion-neutral collision frequency becomes comparable to the ion gyroradius and therefore the transport of the magnetic field is achieved via the electrons. However, electrons within the IMB are only a few eV and therefore it is expected that the magnetic flux tube convection time is extremely long as compared to that at higher altitudes. It is within the IMB precisely that the draped magnetic flux tubes point in a direction which is not compatible with the draping of the IMF but the Kronian magnetic field Titan was exposed to 20 minutes before closest approach. As a result, the sudden increase in the massloading at the IMB, makes the IM the spatial place where the magnetic history of Titan's environment is stored, in the same way as comets (Raeder et al. 1987). The lifetime of this 'magnetic memory' would range from a few tens of minutes up to 3 hours (Bertucci et al. 2008). This result led to a few theoretical studies based on MHD-Hall (Ma et al. 2009), and hybrid (Simon et al. 2009) simulations with simplified geometry, which gave fossil field lifetimes compatible with the observations.

The removal of fossil fields from Titan's induced magnetosphere can be achieved via diffusion driven processes—such as reconnection between these and new field lines with strong

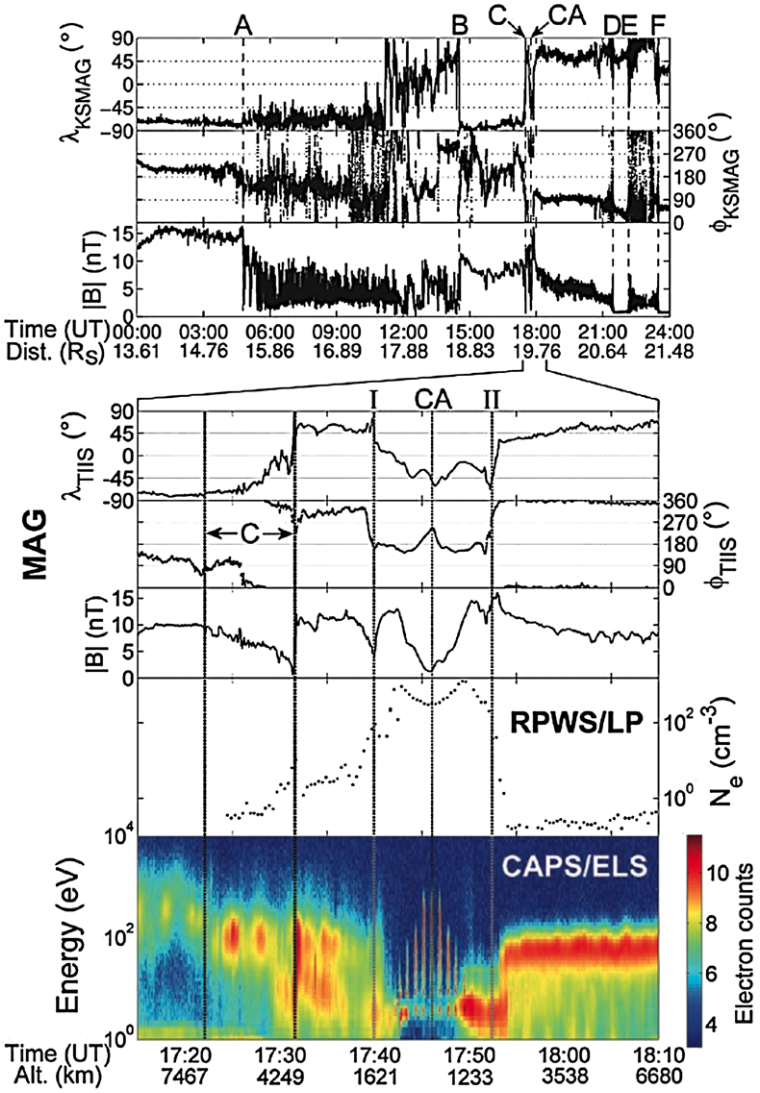

Fig. 36 *Above*: Cassini MAG measurements on 13 June 2007 in spherical KSMAG coordinates. The encounters with the Saturn's magnetopause and bow shock are indicated with the letters *A* to *C* and *D* to *F*, respectively. $|B|$ is the magnetic field strength. Cassini's kronocentric distance is indicated beneath the plots. *Below*: MAG data in spherical TIIS coordinates, plasma density (from RPWS/LP), and electron count rate per energy channel (from CAPS/ELS) during the T32 flyby. Magnetopause crossing C, CA, and the entry (I) and exit (II) of the fossil field region are indicated. Cassini's altitude above Titan is also indicated (from Bertucci et al. 2008)

magnetic shear or diffusion into the ionosphere—or processes involving plasma transport across the magnetic poles of the induced magnetosphere. However, the efficiency of these processes is not well known yet.

Cassini's coverage of Titan's magnetotail at altitudes above $2R_T$ is rather scarce. During the nominal mission, only one flyby covered the mid range tail (around $4R_T$): the

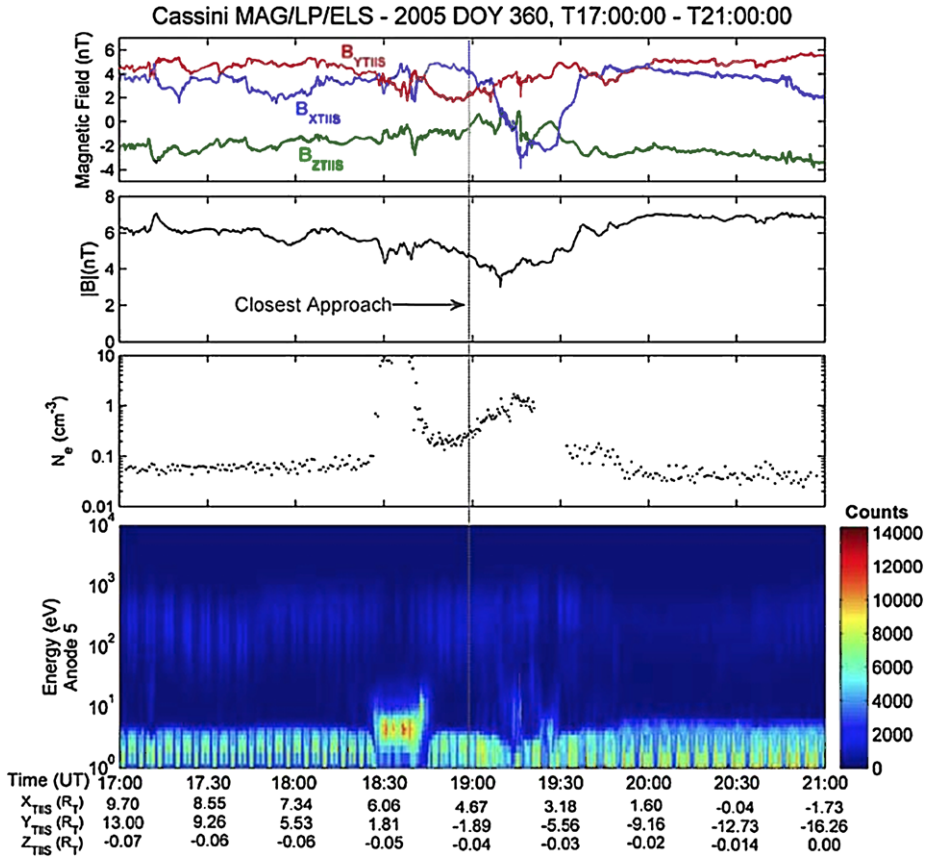

Fig. 37 Magnetic field vector in TIIS coordinates and magnitude (Cassini MAG), electron density (RPWS/LP), and 1 eV–10 KeV electron counts (anode 5) from CAPS/ELS during the T9 flyby (December 26, 2005). Spacecraft position in TIIS coordinates is indicated below the lower panel. Closest approach time is indicated with a *grey line*. The 1832–1838 and 1921–1932 UTC RPWS/LP data gaps are due to a change of mode of the instrument (Bertucci et al. 2007)

T9 flyby. T9 (December 26, 2005) is an outbound, equatorial flyby in Saturn magnetosphere's pre-dawn sector (3.1 hours SLT) at an altitude of 10409.6 km at the time of closest approach (1859 UTC). In the hours leading to the flyby, Cassini has periodic encounters with a probably flapping magnetodisk current sheet (Bertucci 2009). As a result, T9 is likely to have occurred under non-stationary conditions, while Titan and Cassini were temporarily in the magnetodisk's southern lobe (Bertucci et al. 2007; Sittler et al. 2010b). Cassini MAG (TIIS coordinates), RPWS and CAPS/ELS data around T9 are shown in Fig. 37. The first element to note is that the background magnetic field lies almost on the $(X_{\mathrm{TIIS}}, Y_{\mathrm{TIIS}})$ plane with B_{YTIIS} the strongest component. This places the tail's neutral sheet on a plane almost parallel to the B_{ZTIIS} and the flow velocity vector, where Cassini can cross it. A second important aspect of this flyby is that the peak of the upstream distribution function is outside the field of view of the CAPS instrument, implying a significant ($>40°$) displacement of the flow direction from co-rotation (Szego et al. 2007). The resulting geometry is such that Cassini first explores the away lobe (i.e. field lines pointing away from Titan) while it is located downstream from the dayside hemisphere, followed by

the 'toward' lobe, located downstream from the nightside hemisphere. According to MAG data, the IMB/Tail boundary inbound crossing takes place a few minutes before 1830. This coincides with the peak electron energy decrease observed by CAPS/ELS around 1825 and the increase in electron density observed by RPWS/LP. The plasma density reaches a peak value of 10 cm^{-3}, where 16–19 and 28–40 amu ions (Szego et al. 2007), and ∼20 eV ionospheric photoelectrons are observed (Coates et al. 2007). An abrupt change in B_{XTIIS} takes place a few minutes after CA (∼1906) suggesting the crossing of the tail's polarity reversal layer. This signature is immediately followed by a minimum in the magnetic field magnitude (3 nT at 1909:31) after which B_{XTIIS} remains negative until 1935 (magnetotail's toward lobe). During that interval, CAPS and LP data reveal a second region populated with cold plasma from Titan but with a different composition (1–2 amu ions Szego et al. (2007)).

In the light of the difficulties to obtain the upstream flow velocity vector direction from plasma measurements, Bertucci et al. (2007) provided an approximate estimation assuming that Cassini crossed the center of Titan's magnetic tail when the magnetic field strength was the lowest. That led to a unit vector with TIIS components $v = (0.81,\ -0.59,\ -0.01)$, i.e., 36.05° away from the ideal co-rotation towards Saturn, on the equatorial (X_{TIIS}, Y_{TIIS}) plane. This is consistent with the Kronian plasma velocity vectors reported around $20R_S$ in the pre-dawn sector by McAndrews et al. (2009). The outbound crossing of the IMB occurs around 1936. This signature coincides with the change in the electron temperature around 1930.

Cassini measurements during the T9 flyby represent the first evidence of local plasma escape in the mid-range tail. In particular, clear evidence of escaping heavy plasma along Kronian magnetic field lines draped around Titan (Bertucci et al. 2007; Wei et al. 2007) is observed during the inbound leg. The local plasma signature on the outbound leg, however, is explained as light pick up ions from Titan's exosphere (Sittler et al. 2010b). In the latter, the absence of photoelectron signature suggests that the field lines there are connected to Titan's nightside.

4.4 The Ionospheric Boundary

In spite of its long heliocentric distance, photoionization is largely responsible for the formation of Titan's ionosphere (Ågren et al. 2007). However, unlike Mars and Venus, the EUV flux at Titan is in general not aligned with the upstream flow. As a result, Titan's ionosphere has a varying efficiency in preventing external magnetic fields from accessing the neutral atmosphere.

Nevertheless, Titan's ionosphere is usually associated with attenuated magnetic fields and surrounded by clear drops in the magnetic field strength. These drops are observed for different configurations (Neubauer et al. 2006; Simon et al. 2008; Bertucci et al. 2008), but MAG data hardly ever shows a field free ionosphere (Wei et al. 2011).

It is still uncertain if these magnetic field drops reveal a Venus-like ionopause. Rosenqvist et al. (2009) reports that the magnetic field strength drops coincide with the lowest (∼1000 km altitude) of the two peaks in the altitude profile of the Pedersen conductivity within Titan's ionosphere. However, the electron density is rather constant across the field drop.

During the T32 flyby, both Bertucci et al. (2008) and Garnier (2009) report a gradual increase in the electron density in coincidence with the magnetic field strength drops observed in the collisional ionosphere. However, it is still unclear if pressure balance is satisfied across the field drop.

Signatures of photoelectrons (Coates et al. 2011) have been observed in all sunlit portions of Titan's ionosphere (Hartle et al. 2006), but also in remote locations, indicating transport

along field lines from ionospheric regions (Coates et al. 2007). The signature characterizing these photoelectrons is the spectral line at 22–24 eV when corrected for spacecraft potential (Coates et al. 2007), which corresponds to ionization of N_2 due to solar He 304 nm line (Sittler et al. 2010b). It is very likely that the photoelectron signature is not associated to the IMB signatures mentioned above. Cassini measurements during the T5 flyby where a clear IMB but no photoelectron signature was observed seem to support this idea.

5 Comparisons and Conclusions

In spite of the differences in size, heliocentric distance, atmospheric composition, and plasma environment the induced magnetospheres of Mars, Venus and Titan present clear similarities and differences. In this comparison, it is important to include active comets, which represent a particular example based entirely on massloading (Szego et al. 2000 and references therein).

The first element to consider is the fact that induced magnetospheres are plasma structures which have been shown to be rather permanent over time. This has been unequivocally shown in the case of Mars, Venus and to some extent active comets. However, as this assertion applies to most of the in situ observations, it is worth mentioning that interesting transient alterations of the induced magnetospheres have been reported at Venus (Zhang et al. 2009), where incidentally, the IMF cone angle is small, leading to a negligible upstream convective electric field. In such a scenario, the coupling between the solar wind and the plasma population is likely to be achieved via acceleration processes involving electromagnetic plasma waves probably originating in field-aligned planetary ion beams.

In spite of the important variability of its environment (see Arridge et al., this issue), Cassini plasma measurements also reveal regular features around Titan. However, it is expected that upcoming flybys during the Solstice Mission improve not only the spatial coverage of observations around the moon, but also the range of regimes under which Titan interacts, including post-equinox observations. This will provide additional elements to conclude if the structures within the moon's induced magnetosphere are permanent.

Second, apart from the signatures deriving form the supermagnetosonic nature of the solar wind (bow shock and magnetosheath), the stages in which the momentum and energy transfer from the wind to the atmosphere occurs seem to be spatially ordered in a similar way at all these objects:

(i) Formation of an external boundary of the induced magnetosphere (IMB) with the following common signatures:

(a) A strong change (usually an increase, especially on ram side) in the magnetic field strength.
(b) Enhancement of the magnetic field draping.
(c) Decrease in the temperature of electrons.
(d) Decrease in the external ion density and energy.

These signatures, not exactly co-located but likely interdependent, mark the start of the obstacle to the flow. Both ionosphere and exosphere contribute to the obstacle, but the relative preponderance of these two actors varies from one object to the other. Active comets and Venus will likely be at each end of the spectrum as examples, respectively, of pure a exospheric interaction and an interaction where the ionospheric variability controls the induced magnetosphere.

However, the role that the cold and hot exospheres play in every one of these objects, and how their scale height and composition impacts on the ability to generate massloading is an

issue that remains to be investigated. Perhaps Titan is the most complex and least studied object in this matter, not only because of the different scenarios the interaction can occur, but also because of the complex chemistry that governs its upper atmosphere.

(ii) The induced magnetosphere represents the region where most of the momentum and energy is transferred between the external and the local plasma population. This is the place where local ion acceleration processes operate and for that reason this region is key in the study of planetary ion escape. Some of these acceleration mechanisms have been studied and tested at Mars, Venus, and more recently at Titan. In the case of Mars, agreement has been found between estimates of the forces exerted on planetary charged particles and their energies, validating the presence of those mechanisms. However, this is still one of the aspects on which more advances are expected, and such advances will require multi-instrumental measurements with relatively high time resolution due to its limited size on the ram side.

The magnetic tails of Mars, Venus, Titan and active comets are similar in magnetic structure with two well-defined lobes of opposite magnetic field polarity, and whose orientation depends on that of the upstream field and plasma flow. However, the distribution of plasma populations within the tail seems to be differences probably based on the efficiency of upstream/downstream plasma transport mechanisms, but observations at Mars and Venus both suggest a non-negligible role played by the upstream convective electric field. At Titan, such a role has not been assessed yet, although simulations (Modolo and Chanteur 2008) suggest that more energetic particles would be found on the hemisphere where the convective electric field points outward.

(iii) On the dayside, an ionospheric boundary marks the lower edge of the induced magnetosphere. As for the IMB, the ionospheric boundary is characterized by common signatures:

(a) Appearance of local photoelectron population.
(b) Increase in the electron density.
(c) With the exception of Mars crustal fields, a usual decrease in the magnetic field strength.

Once again, these signatures are not always co-located.

The processes by which the external plasma and magnetic field are prevented from penetrating the ionospheric boundary are different for each object. At Mars, the crustal magnetic field should be considered in the local plasma pressure budget, at Titan collision rate increase with decreasing altitude, leading to diffusion below 1000 km altitude (Cravens et al. 2010b). At Venus, more or less efficient pressure balance occurs, depending on solar cycle phase.

The similarity in the properties found in the plasma regions and discontinuities within the induced magnetospheres of Mars, Venus, Titan and active comets suggest that all these interactions should rest upon basic common processes. One approach to a formulation of a theory of induced magnetospheres based on 'first principles' was explored by Dubinin et al. (2006d), who discussed the formation of 1-D plasma discontinuities in a stationary flow of a plasma consisting of two proton populations and massless and isothermal electrons streaming against a heavy ion cloud. Starting from the standard multifluid equations of continuity and momentum, this work concludes that in a non-magnetized plasma and under specific conditions, a 'heavy ion shock' accompanied by a proton rarefaction is formed. This 'heavy ion shock' has properties similar to the IMB. If a transverse magnetic field is introduced, the differential ion streaming becomes more 'rigid' and a deceleration of the collective plasma flow at superfast speeds is accompanied with an increase of the magnetic field strength. The collective flow stops when the critical loci are reached. This simple model shows that the differential streaming provides an inherent electromagnetic coupling mechanism that leads

to key features which are observed at induced magnetospheres, namely the IMB. Efforts in this type of analytical approach to the problem should be continued.

On the other hand, sophisticated global simulations are increasingly effective in reproducing and explaining many of the features observed around induced magnetospheres (Kallio et al., this issue). In particular, recent efforts to couple these global models with exospheric models are being undertaken. This will significantly improve the description of the interaction in the light of the important role played by the exosphere on these interactions.

On the other hand, efforts such as the SWIM Challenge (Brain et al. 2010b) have been important to test the capacity of models in reproducing these features and should be imitated for other objects.

In summary, in situ measurements around the induced magnetospheres of Mars, Venus, Titan and active comets have revealed common structures and processes. However, there is an urge for simultaneous measurements of basic plasma parameters in order to undertake proper assessments of the properties of their different regions and boundaries. In the near future, this will be hopefully possible with upcoming missions MAVEN and Rosetta. Similar initiatives should be imitated in the case of Venus. In the case of Titan, measurements during the Cassini Solstice Mission are being awaited in order to expand our knowledge on the range of upstream conditions the moon is immersed in as well as their consequences on its plasma environment.

Acknowledgements Authors thank the International Space Science Institute (ISSI) for supporting this work. CB is supported by the National Science and Technology Research Council (CONICET) and the Agency for the Promotion of Science and Technology of Argentina.

NJTE was supported by the Swedish Institute of Space Physics through a grant from the Swedish Science Council (Vetenskapsrådet).

References

N. Achilleos, C.S. Arridge, C. Bertucci, C.M. Jackman, M.K. Dougherty, K.K. Khurana, C.T. Russell, Large-scale dynamics of Saturn's magnetopause: observations by Cassini. J. Geophys. Res. **113**, A11209 (2008). doi:10.1029/2008JA013265

M.H. Acuña et al., Mars Observer magnetic fields investigation. J. Geophys. Res. **97**(E5), 7799–7814 (1992)

M.H. Acuña et al., Magnetic field and plasma observations at Mars: Initial results of the Mars Global Surveyor mission. Science **279**, 1676–1680 (1998)

K. Ågren et al., On magnetospheric electron impact ionization and dynamics in Titan's ram-side and polar ionosphere, a Cassini case study. Ann. Geophys. **25**, 2359 (2007)

A. Albee et al., Overview of the Mars Global Surveyor mission. J. Geophys. Res. **106**(E10), 23291–23316 (2001)

H. Alfven, On the theory of comet tails. Tellus **9**, 92 (1957)

C.S. Arridge, N. Achilleos, M.K. Dougherty, K.K. Khurana, C.T. Russell, Modeling the size and shape of Saturn's magnetopause with variable dynamic pressure. J. Geophys. Res. **111**, A11227 (2006). doi:10.1029/2005JA011574

C.S. Arridge, C.T. Russell, K.K. Khurana, N. Achilleos, S.W.H. Cowley, M.K. Dougherty, D.J. Southwood, E.J. Bunce, Saturn's magnetodisc current sheet. J. Geophys. Res. **113**, A04214 (2008a). doi:10.1029/2007JA012540

C.S. Arridge, N. Andre, N. Achilleos, K.K. Khurana, C.L. Bertucci, L.K. Gilbert, G.R. Lewis, A.J. Coates, M.K. Dougherty, Thermal electron periodicities at 20RS in Saturn's magnetosphere. Geophys. Res. Lett. **35**, L15107 (2008b). doi:10.1029/2008GL034132

H.U. Auster et al., ROMAP: Rosetta magnetometer and plasma monitor. Space Sci. Rev. **128**(1), 221–240 (2007)

H. Backes et al., Titan's magnetic field signature during the first Cassini encounter. Science **308**, 992 (2005)

S. Barabash et al., The analyzer of space plasmas and energetic atoms (ASPERA-3) for the Mars Express Mission. Space Sci. Rev. (2006). doi:10.1007/s11214-006-9124-8

S. Barabash et al., The analyser of space plasmas and energetic atoms (ASPERA-4) for the Venus express mission. Planet. Space Sci. **55**, 1772–1792 (2007)

C. Beghin et al., New insights on Titan's plasma-driven Schumann resonance inferred from Huygens and Cassini data. Planet. Space Sci. **57**(14–15), 1872–1888 (2009)
C. Bertucci, Characteristics and variability of Titan's magnetic environment. Philos. Trans. R. Soc. Lond. A **367**, 789–798 (2009). doi:10.1098/rsta.2008.02502009
C. Bertucci et al., Magnetic field draping enhancement at the Martian magnetic pileup boundary from Mars global surveyor observations. Geophys. Res. Lett. **30**(2), 1099 (2003a). doi:10.1029/2002GL015713
C. Bertucci et al., Magnetic field draping enhancement at Venus: Evidence for a magnetic pileup boundary. Geophys. Res. Lett. **30**(17), 1876 (2003b). doi:10.1029/2003GL017271
C. Bertucci et al., MGS MAG/ER ER observations at the magnetic pileup boundary of Mars: draping enhancement and low frequency waves. Adv. Space Res. **33**(11), 1938–1944 (2004)
C. Bertucci et al., Structure of the magnetic pileup boundary at Mars and Venus. J. Geophys. Res. **110**, A01209 (2005a). doi:10.1029/2004JA010592
C. Bertucci et al., Interaction of the solar wind with Mars from Mars Global Surveyor MAG/ER observations. Journal of Atmospheric and Terrestrial Physics **67**(17–18), 1797–1808 (2005b)
C. Bertucci et al., Titan's interaction with its plasma environment. American Geophysical Union, Fall Meeting 2005, abstract #P52A-02 (2005c)
C. Bertucci, F.M. Neubauer, K. Szego, J.-E. Wahlund, A.J. Coates, M.K. Dougherty, D.T. Young, W.S. Kurth, Structure of Titan's mid-range magnetic tail: Cassini magnetometer observations during the T9 flyby. Geophys. Res. Lett. **34**, L24S02 (2007). doi:10.1029/2007GL030865
C. Bertucci et al., The magnetic memory of Titan's ionized atmosphere. Science **321**(5895), 1475 (2008)
C. Bertucci et al., The variability of Titan's magnetic environment. Planet. Space Sci., 1813–1820 (2009)
L.H. Brace et al., The ionotail of Venus—Its configuration and evidence for ion escape. J. Geophys. Res. **92**(1), 15–26 (1987)
L.H. Brace et al., The dynamic behavior of the Venus ionosphere in response to solar wind interactions. J. Geophys. Res. **85**(A13), 7663–7678 (1980)
D.A. Brain et al., Observations of low-frequency electromagnetic plasma waves upstream from the Martian shock. J. Geophys. Res. **107**(A6), 1076 (2002). doi:10.1029/2000JA000416
D.A. Brain et al., Martian magnetic morphology: Contributions from the solar wind and crust. J. Geophys. Res. **108**(A12), 1424 (2003). doi:10.1029/2002JA009482
D.A. Brain et al., Variability of the altitude of the Martian sheath. Geophys. Res. Lett. **32**, L18203 (2005). doi:10.1029/2005GL023126
D.A. Brain et al., Episodic detachment of Martian crustal magnetic fields leading to bulk atmospheric plasma escape. Geophys. Res. Lett. **37**(14), L14108 (2010a)
D.A. Brain et al., A comparison of global models for the solar wind interaction with Mars. Icarus **206**, 139–151 (2010b)
J.C. Cain et al., An $n = 90$ internal potential function of the martian crustal magnetic field. J. Geophys. Res. **108**(E2), 5008 (2003). doi:10.1029/2000JE001487
L. Gan, T.E. Cravens, M. Horanyi, Electrons in the ionopause boundary layer of Venus. J. Geophys. Res. **95**(1), 19023–19035 (1990)
J.Y. Chaufray, J.L. Bertaux, F. Leblanc, E. Quémerais, Observation of the hydrogen corona with SPICAM on Mars Express. Icarus **195**(2), 598–613 (2008)
A. Chicarro et al., Mars express: a European mission to the red planet, in *Mars Express, The Scientific Payload, SP-1240*, ed. by A. Wilson (ESA Publication Division, Noordwijk, 2004), pp. 3–16
A.J. Coates et al., Ionospheric electrons in Titan's tail: Plasma structure during the Cassini T9 encounter. Geophys. Res. Lett. **34**(24), L24S05 (2007)
A.J. Coates et al., Ionospheric photoelectrons at Venus: initial observations by ASPERA-4 ELS. Planet. Space Sci. **56**(6), 802–806 (2008)
A.J. Coates et al., Ionospheric photoelectrons: comparing Venus, Earth, Mars and Titan planetary and space science. Planet. Space Sci. **59**(10), 1019–1027 (2011)
J.E.P. Connerney, M.H. Acuña, N.F. Ness, G. Kletetschka, D.L. Mitchell, R.P. Lin, H. Rème, Proc. Natl. Acad. Sci. USA **102**(42), 14970–14975 (2005)
T.E. Cravens et al., Model calculations of the dayside ionosphere of Venus: energetics. J. Geophys. Res. **85**, 7778–7786 (1980)
T.E. Cravens, R.V. Yelle, J.-E. Wahlund, D.E. Shemansky, A.F. Nagy, Composition and structure of the ionosphere and thermosphere, in *Titan From Cassini-Huygens*, chap. 11, p. 259. ed. by R.H. Brown, J.-P. Lebreton, J.H. Waite (Springer, Dordrecht, 2010b). ISBN:978-1-4020-9214-5
D.H. Crider et al., Evidence of electron impact ionization in the magnetic pileup boundary of Mars. Geophys. Res. Lett. **27**(1), 45–48 (2000)
D.H. Crider et al., Observations of the latitude dependence of the location of the martian magnetic pileup boundary. Geophys. Res. Lett. **29**(8), 1170 (2002) doi:10.1029/2001GL013860

D.H. Crider et al., Mars global surveyor observations of solar wind magnetic field draping around Mars. Space Sci. Rev. **111**(1), 203–221 (2004)
Sh. Dolginov et al., The magnetic field of Mars according to the data from the Mars 3 and Mars 5. J. Geophys. Res. **81**(19), 3353–3362 (1976)
Sh.Sh. Dolginov, E.M. Dubinin, Ye.G. Yeroshenko, P.L. Israilevich, I.M. Podgorny, S.I. Shkol'nikova, On the configuration of the field in the magnetic tail of Venus. Cosm. Res. **19**, 624 (1981)
M.K. Dougherty et al., The Cassini magnetic field investigation. Space Sci. Rev. **114**, 331–383 (2004). doi:10.1007/s11214-004-1432-2
J. Du, T.L. Zhang, C. Wang, M. Wolwerk, M. Delva, W. Baumjohann, Magnetosheath fluctuations at Venus for two extreme orientations of the interplanetary magnetic field. Geophys. Res. Lett. **36**(9), L09102 (2009)
E. Dubinin et al., Cold ions at the Martian bow shock—PHOBOS observations. J. Geophys. Res. **98**(A4), 5617–5623 (1993a)
E. Dubinin et al., Ion acceleration in the Martian tail: phobos observations. J. Geophys. Res. **98**(A3), 3991–3997 (1993b)
E. Dubinin et al., Plasma morphology at Mars. ASPERA 3 observations. Space Sci. Rev. (2006a). doi:10.1007/s11214-006-9039-4
E. Dubinin et al., Electric fields within the Martian magnetosphere and ion extraction: ASPERA-3 observations. Icarus **182**, 337–342 (2006b)
E. Dubinin et al., Solar wind plasma protrusion into the Martian magnetosphere: ASPERA-3 observations. Icarus **182**(2006), 343–349 (2006c)
E. Dubinin et al., Nonlinear 1-D stationary flows in multi-ion plasmas—sonic and critical loci—solitary and "oscillatory" waves. Ann. Geophys. **24**(11), 3041–3057 (2006d)
E. Dubinin et al., Structure and dynamics of the solar wind/ionosphere interface on Mars: MEX-ASPERA-3 and MEX-MARSIS observations. Geophys. Res. Lett. **35**, 11103 (2008a)
E.M. Dubinin et al., Access of solar wind electrons into the Martian magnetosphere. Ann. Geophys. **26**(11), 3511–3524 (2008b)
F. Duru et al., Magnetically controlled structures in the ionosphere of Mars. J. Geophys. Res. **111**, A11204 (2006). doi:10.1029/2006JA011975
F. Duru et al., Transient density gradients in the Martian ionosphere similar to the ionopause at Venus. J. Geophys. Res. **114**(A12), A12310 (2009) (JGRA Homepage)
F. Duru et al., A plasma flow velocity boundary at Mars from the disappearance of electron plasma oscillations. Icarus **206**, 74–82 (2010)
J.P. Eastwood, D.A. Brain, J.S. Halekas, J.F. Drake, T.D. Phan, M. Øieroset, D.L. Mitchell, R.P. Lin, M. Acuña, Evidence for collisionless magnetic reconnection at Mars. Geophys. Res. Lett. **35**(2), L02106 (2008)
N.J.T. Edberg et al., Statistical analysis of the location of the Martian magnetic pileup boundary and bow shock and the influence of crustal magnetic fields J. Geophys. Res. **113**(A8), A08206 (2008)
N.J.T. Edberg et al., Simultaneous measurements of Martian plasma boundaries by Rosetta and Mars Express. Planet. Space Sci. **57**(8–9), 1085–1096 (2009a)
N.J.T. Edberg, D.A. Brain, M. Lester, S.W.H. Cowley, R. Modolo, M. Fränz, S. Barabash, Plasma boundary variability at Mars as observed by Mars Global Surveyor and Mars Express. Ann. Geophys. **27**(9), 3537–3550 (2009b)
N.J.T. Edberg, M. Lester, S.W.H. Cowley, D.A. Brain, M. Fränz, S. Barabash, Magnetosonic Mach number effect of the position of the bow shock at Mars in comparison to Venus. J. Geophys. Res. **115**, A07203 (2010). doi:10.1029/2009JA014998
R.C. Elphic et al., Observations of the dayside ionopause and ionosphere of Venus. J. Geophys. Res. **85**, 7679 (1980)
R.C. Elphic et al., The Venus ionopause current sheet: thickness length scale and controlling factors. J. Geophys. Res. **86**(A13), 11430–11438 (1981)
J.R. Espley et al., Observations of low-frequency magnetic oscillations in the Martian magnetosheath, magnetic pileup region, and tail. J. Geophys. Res. **109**(A7), A07213 (2004)
A. Fedorov et al., Structure of the Martian Wake. Icarus **182**, 329–336 (2006)
A. Fedorov et al., Comparative analysis of Venus and Mars magnetotails. Planet. Space Sci. **56**, 812–817 (2008)
R.A. Frahm et al., Location of atmospheric photoelectron energy peaks within the Mars environment. Space Sci. Rev. **126**, 389 (2006)
R.A. Frahm et al., Estimation of the escape of photoelectrons from Mars in 2004 liberated by the ionization of carbon dioxide and atomic oxygen. Icarus **206**(1), 50–63 (2010)
M. Fränz, E. Dubinin, E. Roussos, J. Woch, J.D. Winningham, R. Frahm, A.J. Coates, A. Fedorov, S. Barabash, R. Lundin, Plasma moments in the environment of Mars. Mars Express ASPERA-3 observations. Space Sci. Rev. (2006a). doi:10.1007/s11214-006-9115-9

M. Fränz et al., Plasma intrusion above Mars crustal fields—Mars Express ASPERA-3 observations. Icarus (2006b). doi:10.1016/j.icarus.2005.11.016
J.L. Fox, A. Dalgarno, Ionization, luminosity, and heating of the upper atmosphere of Mars. J. Geophys. Res. **84**, 7315–7333 (1979)
P. Garnier, Titan's ionosphere in the magnetosheath: Cassini RPWS results during the T32 flyby. Ann. Geophys. **27**(11), 4257–4272 (2009)
R. Grard et al., First measurements of plasma waves near Mars. Nature **341**(19), 607–609 (1989)
K.I. Gringauz, V.V. Bezrukikh, T.K. Breus, T. Gombosi, A.P. Remizov, M.I. Verigin, G.I. Volkov, Plasma observations near Venus onboard Venera 9 and Venera 10 satellites by means of wide angle plasma detectors, in *Physics of Solar Planetary Environment*, ed. by D.J. Williams (AGU, Boulder, 1976), pp. 918–932
D.A. Gurnett, A. Bhattacharjee, *Introduction to Plasma Physics with Space and Laboratory Applications* (Cambridge University Press, Cambridge, 2005)
D.A. Gurnett et al., The Cassini radio and plasma wave investigation. Space Sci. Rev. **114**, 395–463 (2004)
D.A. Gurnett et al., Radar soundings of the ionosphere of Mars. Science **310**, 1929–1933 (2005)
J.S. Halekas et al., Current sheets at low altitudes in the Martian magnetotail. Geophys. Res. Lett. **33**(13), L13101 (2006)
J.S. Halekas, D.A. Brain, R.P. Lin, J.G. Luhmann, D.L. Mitchell, Distribution and variability of accelerated electrons at Mars. Adv. Space Res. **41**(9), 1347–1352 (2008)
R.E. Hartle et al., Titan's ion exosphere observed from Voyager 1. J. Geophys. Res. **87**, 1383–1394 (1982)
R. Hartle et al., Initial interpretation of Titan plasma interaction as observed by the Cassini plasma spectrometer: comparisons with Voyager 1. Planet. Space Sci. **54**(12), 1211–1224 (2006)
A. Hasegawa, *Plasma Instabilities and Non Linear Effects*, Phys. and in Chem. Space, vol. 8 (Springer, New York, 1975)
M.M. Hoppe, C.T. Russell, Particle acceleration at planetary bow shock waves. Nature **295**, 41–42 (1982)
K.K. Khurana et al., Sources of rotational signals in Saturn's magnetosphere. J. Geophys. Res. **114**(A2), A02211 (2009)
T. Knetter, F.M. Neubauer, T. Horbury, A. Balogh, Four-point discontinuity observations using Cluster magnetic field data: a statistical survey. J. Geophys. Res. **109**(A6), A06102 (2004)
W.C. Knudsen, K.L. Miller, K. Spenner, Improved Venus ionopause altitude calculation and comparison with measurement. J. Geophys. Res. **87**, 2246–2254 (1982)
W.C. Knudsen et al., Retarding potential analyzer for the Pioneer-Venus Orbiter Mission. Space Sci. Instrum. **4**, 351–372 (1979)
W.C. Knudsen et al., Suprathermal electron energy distribution within the dayside venus ionosphere. J. Geophys. Res. **85**(A13), 7754–7758 (1980). doi:10.1029/JA085iA13p07754
W.C. Knudsen et al., Solar cycle changes in the ionization sources of the nightside Venus ionosphere. J. Geophys. Res. **92**, 13391 (1987)
W.C. Knudsen, Solar cycle changes in the morphology of the Venus ionosphere. J. Geophys. Res. **93**, 8756 (1988)
W.S. Kurth et al., An update to a Saturnian longitude system based on kilometric radio emissions. J. Geophys. Res. **113**, A05222 (2008). doi:10.1029/2007JA012861
B. Lembège, P. Savoini, Formation of reflected electron bursts by the nonstationarity and nonuniformity of a collisionless shock front. J. Geophys. Res. **107**(A3), 1037 (2002). doi:10.1029/2001JA900128
J.G. Luhmann, A model of the ionospheric tail rays of Venus. J. Geophys. Res. **98**(A10), 17615–17622 (1993)
J.G. Luhmann et al., Magnetic field fluctuations in the Venus magnetosheath. Geophys. Res. Lett. **10**, 655–658 (1983)
R. Lundin et al., On the momentum transfer of the solar wind to the Martian topside ionosphere. Geophys. Res. Lett. **18**, 1059–1062 (1991)
R. Lundin, E.M. Dubinin, Phobos-2 results on the ionospheric plasma escape from Mars. Adv. Space Res. **12**(9), 255–263 (1992)
R. Lundin et al., Solar wind-induced atmospheric erosion at Mars: first results from ASPERA-3 on Mars Express. Science **305**(5692), 1933–1936 (2004)
R. Lundin, S. Barabash, M. Holmstrom, H. Nilsson, M. Yamauchi, E.M. Dubinin, M. Fraenz, Atmospheric origin of cold ion escape from Mars. Geophys. Res. Lett. **36**, L17202 (2009). doi:10.1029/2009GL039341
Y.J. Ma et al., Time-dependent global MHD simulations of Cassini T32 flyby: From magnetosphere to magnetosheath. J. Geophys. Res. **114**, A03204 (2009). doi:10.1029/2008JA013676
G.P. Mantas, W.B. Hanson, Photoelectron fluxes in the Martian ionosphere. J. Geophys. Res. **84**, 369–385 (1979)
C. Martinecz, The Venus plasma environment: a comparison of Venus Express ASPERA-4 measurements with 3D hybrid simulations. Ph.D. thesis, Uni. Braunschweig (2008)

C. Martinecz et al., Location of the bow shock and ion composition boundaries at Venus-initial determinations from Venus Express ASPERA-4. Planet. Space Sci. **56**, 780–784 (2008). doi:10.1016/j.pss.2007.07.007
C. Martinecz, A. Boesswetter, M. Fränz, E. Roussos, J. Woch, N. Krupp, E. Dubinin, U. Motschmann, S. Wiehle, S. Simon, S. Barabash, R. Lundin, T.L. Zhang, H. Lammer, H. Lichtenegger, Y. Kulikov, The plasma environment of Venus: comparison of Venus Express ASPERA-4 measurements with 3D hybrid simulations. J. Geophys. Res. **114**, E00B30 (2009). doi:10.1029/2008JE003174; Correction: J. Geophys. Res. **114**, E00B98 (2009). doi:10.1029/2009JE003377
C. Mazelle, H. Reme, G. Belmont et al., Ultra low frequency waves at the magnetic pile-up boundary of comet P/Halley. Adv. Space Res. **11**(9), 73–77 (1991)
C. Mazelle et al., Bow shock and upstream phenomena at Mars. Space Sci. Rev. **111**(1), 115–181 (2004)
H.J. McAndrews et al., Plasma in Saturn's nightside magnetosphere and the implications for global circulation. Planet. Space Sci. **57**(14–15), 1714–1722 (2009)
D.J. McComas, H.E. Spence, C.T. Russell, M.A. Saunders, The average magnetic field draping and consistent plasma properties of the Venus magnetotail. J. Geophys. Res. **91**, 7939–7953 (1986)
P.T. McCormick et al., On the energy deposition of photoelectrons in the atmosphere of Venus. J. Geophys. Res. **81**, 5196–5200 (1976)
D.L. Mitchell, Probing Mars' crustal magnetic field and ionosphere with the MGS Electron Reflectometer. J. Geophys. Res. **106**(E10), 23419–23428 (2001)
R. Modolo, G.M. Chanteur, A global hybrid model for Titan's interaction with the Kronian plasma: Application to the Cassini Ta flyby. J. Geophys. Res. **113**, A01317 (2008). doi:10.1029/2007JA012453
R. Modolo et al., Simulated solar wind plasma interaction with the Martian exosphere: influence of the solar EUV flux on the bow shock and the magnetic pile-up boundary. Ann. Geophys. **24**(12), 3403–3410 (2006)
S.L. Moses, F.V. Coroniti, F.L. Scarf, Expectations for the microphysics of the Mars-solar wind interaction. Geophys. Res. Lett. **15**(5), 429–432 (1988). doi:10.1029/GL015i005p00429
A.F. Nagy, D. Winterhalter, K. Sauer, T.E. Cravens, S. Brecht, C. Mazelle, D. Crider, E. Kallio, A. Zakharov, E. Dubinin, M. Verigin, G. Kotova, W.I. Axford, C. Bertucci, J.G. Trotignon, The plasma environment of Mars. Space Sci. Rev. **111**, 33–114 (2004)
N.F. Ness, M.H. Acuna, K.W. Behannon, The induced magnetosphere of Titan. J. Geophys. Res. **87**(1), 1369–1381 (1982)
F.M. Neubauer et al., Titan's magnetospheric interaction, in *Saturn*, ed. by T. Gehrels, M.S. Matthews (University of Arizona Press, Tucson, 1984), pp. 760–787
F.M. Neubauer et al., Titan's near magnetotail from magnetic field and plasma observations and modelling: Cassini flybys TA, TB and T3. J. Geophys. Res. **111**, A10220 (2006). doi:10.1029/2006JA011676
H. Pérez-de-Tejada, Distribution of plasma and magnetic fluxes in the Venus near wake. J. Geophys. Res. **91**, 8039 (1986)
J.L. Phillips, D.J. McComas, The magnetosheath and magnetotail of Venus. Space Sci. Rev. **55**, 1–80 (1991)
G. Picardi et al., Mars Express: a European mission to the red planet. ESA SP **SP-1240**, 51 (2004)
J. Raeder et al., Macroscopic perturbations of the IMF by P/Halley as seen by the Giotto magnetometer. Astron. Astrophys. **187**, 61–64 (1987)
H. Rosenbauer et al., The relationship between the magnetic field in the Martian magnetotail and upstream solar wind parameters. J. Geophys. Res. **99**(A9), 17,199–17,204 (1994)
L. Rosenqvist et al., Titan ionospheric conductivities from Cassini measurements. Planet. Space Sci. **57**(14–15), 1828–1833 (2009)
C.T. Russell, The magnetic field of Mars—Mars 3 evidence re-examined. Geophys. Res. Lett. **5**, 81–84 (1978a)
C.T. Russell, The magnetic field of Mars—Mars 5 evidence re-examined. Geophys. Res. Lett. **5**, 85–88 (1978b)
C.T. Russell et al., Initial Pioneer-Venus magnetic field results: dayside observations. Science **203**, 745–748 (1979)
C.T. Russell et al., Pioneer-Venus flux gate magnetometer. IEEE Trans. Geosci. Electron. **GE-18**, 32–35 (1980)
C.T. Russell, O. Vaisberg, The interaction of the solar wind with Venus, in *Venus*, ed. by D.M. Hunton, L. Colin, T.M. Donahue, V.I. Moroz (University of Arizona Press, Tucson, 1983), pp. 873–940
C.T. Russell, E. Chou, J.G. Luhmann, P. Gazis, L.H. Brace, W.R. Hoegy, Solar and interplanetary control of the location of the Venus bow shock. J. Geophys. Res. **93**, 5461–5469 (1988)
C.T. Russell, J.G. Luhmann, R.J. Strangeway, The solar wind interaction with Venus through the eyes of the Pioneer Venus Orbiter. Planet. Space Sci. **54**, 1482–1495 (2006a)
C.T. Russell, S.S. Mayerberger, X. Blanco-Cano, Proton cyclotron waves at Mars and Venus. Adv. Space Res. **38**, 745–751 (2006b)

A.M. Rymer et al., Discrete classification and electron energy spectra of Titan's varied magnetospheric environment. Geophys. Res. Lett. **36**, L15109 (2009). doi:10.1029/2009GL039427
M.A. Saunders, C.T. Russell, Average dimension and magnetic structure of the distant Venus magnetotail. J. Geophys. Res. **91**, 5589–5604 (1986)
K. Sauer, T. Roatsch, U. Motschmann, K. Schwingenschuh, R. Lundin, H. Rosenbauer, S. Livi, Observations of plasma boundaries and phenomena around Mars with Phobos 2. J. Geophys. Res. **97**, 6227–6233 (1992)
R.W. Schunk, A.F. Nagy, *Ionospheres: Physics, Plasma Physics, and Chemistry* (Cambridge University Press, Cambridge, 2000)
K. Schwingenschuh, W. Riedler, T.-L. Zhang, H. Lichtenegger, H. Rosenbauer, S. Livi, G. Gevai, K. Gringauz, M. Verigin, E. Eroshenko, The Martian magnetic field environment—induced or dominated by an intrinsic magnetic field? Adv. Space Res. **12**(9), 213–219 (1992)
S. Simon et al., Titan's highly dynamic magnetic environment a systematic survey of Cassini magnetometer observations from flybys TA–T62. Planet. Space Sci. **58**(10), 1230–1251 (2010a)
S. Simon et al., Dynamics of Saturn's magnetodisk near Titan's orbit Comparison of Cassini magnetometer observations from real and virtual Titan flybys. Planet. Space Sci. **58**(12), 1625–1635 (2010b)
S. Simon, U. Motschmann, G. Kleindienst, K.-H. Glassmeier, C. Bertucci, M.K. Dougherty, Titan's magnetic field signature during the Cassini T34 flyby: comparison between hybrid simulations and MAG data. Geophys. Res. Lett. **35**, L04107 (2008). doi:10.1029/2007GL033056
S. Simon et al., Titan's plasma environment during a magnetosheath excursion:Real-time scenarios for Cassini's T32 flyby from a hybrid simulation. Ann. Geophys. **27**, 669–685 (2009)
E. Sittler, R.E. Hartle, C. Bertucci, A. Coates, T. Cravens, I. Dandouras, D. Shemansky, Energy deposition processes, in *Titan from Cassini-Huygens*, ed. by R. Brown, J.P. Lebreton, H. Waite (Springer, Dordrecht, 2010a), pp. 393–453. ISBN978-1-4020-9214-5
E.C. Sittler et al., Saturn's magnetospheric interaction with Titan as defined by Cassini encounters T9 and T18: New results. Planet. Space Sci. **58**(3), 327–350 (2010b)
J.A. Slavin, R.C. Elphic, C.T. Russell, F.L. Scarf, J.H. Wolfe, J.D. Mihalov, D.S. Intriligator, L.H. Brace, H.A. Taylor, R.E. Daniell, The solar wind interaction with Venus—Pioneer Venus observations of bow shock location and structure. J. Geophys. Res. **85**, 7625–7641 (1980)
J.A. Slavin, R.E. Holzer, Solar wind flow about the terrestrial planets. I—Modeling bow shock position and shape. J. Geophys. Res. **86**(11), 11401–11418 (1981)
J.A. Slavin, R.E. Holzer, J.R. Spreiter, S.S. Stahara, Planetary Mach cones—theory and observation. J. Geophys. Res. **89**, 2708–2714 (1984)
J.A. Slavin et al., The solar wind interaction with Mars: Mariner 4, Mars 2, Mars 3, Mars 5 and Phobos 2 observations of bow shock position and shape. J. Geophys. Res. **96**, 11235–11241 (1991)
K. Szego et al., Physics of mass loaded plasmas. Space Sci. Rev. **94**(3/4), 429–671 (2000) 2000
B.U.Ö. Sonnerup, M. Scheible, Minimum and maximum variance analysis, in *Analysis Methods for Multi-Spacecraft Data*, ed. by G. Paschmann, P. Daly. ISSI Scientific Reports Series, ESA/ISSI, vol. 1 (1998), pp. 185–220. ISBN1608-280X
K. Spenner, W.C. Knudsen, K.L. Miller, V. Novak, C.T. Russell, R.C. Elphic, Observation of the Venus mantle, the boundary region between solar wind and ionosphere. J. Geophys. Res. **85**, 7655–7662 (1980)
K. Spenner et al., Photoelectron fluxes in the Venus dayside ionosphere. J. Geophys. Res. **102**, 2577–2583 (1997)
K. Szego, Z. Bebesi, C. Bertucci, A.J. Coates, F. Crary, G. Erdos, R. Hartle, E.C. Sittler, D.T. Young, Charged particle environment of Titan during the T9 flyby. Geophys. Res. Lett. **34**(24), L24S03 (2007)
M. Tátrallyay et al., Magnetic field overshoots in the Martian bow shock. J. Geophys. Res. **102**(A2), 2157–2164 (1997)
J.G. Trotignon et al., Position and shape of the martian bow shock: the Phobos 2 plasma wave system observations. Planet. Space Sci. **41**, 189–198 (1993)
J.-G. Trotignon, E. Dubinin, R. Grard, S. Barabash, R. Lundin, Martian planetopause as seen by the plasma wave system onboard Phobos 2. J. Geophys. Res. **101**(A11), 24965–24977 (1996)
J.G. Trotignon, C. Mazelle, C. Bertucci, M.H. Acuña, Martian shock and magnetic pile-up boundary positions and shapes determined from the Phobos 2 and Mars Global Surveyor data sets. Planet. Space Sci. **54**, 357–369 (2006)
B. Tsurutani, G.S. Lakhina, E.J. Smith et al., Mirror mode structures and ELF plasma waves in the Giacobini–Zinner magnetosheath. Nonlinear Process. Geophys. **6**, 229–234 (1999)
O.L. Vaisberg, Mars-plasma environment, in *Physics of Solar Planetary Environment*, ed. by D.J. Williams (AGU, Boulder, 1976), pp. 854–871
O.L. Vaisberg, A.V. Bogdanov, Flow of the solar wind around Mars and Venus—general principles. Cosm. Res. **12**, 253–257 (1974)

O.L. Vaisberg, S.A. Romanov, V.N. Smirnov, I.P. Karpinsky, B.I. Khazanov, B.V. Polenov, A.V. Bogdanov, N.M. Antonov, Ion flux parameters in the solar wind-venus interaction region, in *Physics of Solar Planetary Environment*, ed. by D.J. Williams (AGU, Boulder, 1976), pp. 904–917
O.L. Vaisberg, L.M. Zeleny, Formation of the plasma mantle in the Venusian magnetosphere. Icarus **58**, 412–430 (1984)
O.L. Vaisberg, A.V. Bogdanov, N.F. Borodin, A.A. Zertzalov, B.V. Polenov, S.A. Romanov, Solar plasma interaction with Mars: preliminary results. Icarus **18**, 59–63 (1973)
O. Vaisberg, A. Fedorov, F. Dunjushkin, A. Kozhukhovsky, V. Smirnov, L. Avanov, C.T. Russell, J.G. Luhmann, Ion populations in the tail of Venus. Adv. Space Res. **16**(4), 105–118 (1995)
S. Vennerstrom, N. Olsen, M. Purucker, M.H. Acuña, J.C. Cain, The magnetic field in the pile-up region at Mars, and its variation with the solar wind. Geophys. Res. Lett. **30**(7), 1369 (2003). doi:10.1029/2003GL016883
M.I. Verigin, K.I. Gringauz, T. Gombosi, T.K. Breus, V.V. Bezrukikh, A.P. Remizov, G.I. Volkov, Plasma near Venus from the Venera 9 and 10 wide-angle analyzer data. J. Geophys. Res. **83**, 3721–3728 (1978)
D. Vignes et al., The solar wind interaction with Mars: locations and shapes of the Bow Shock and the magnetic pile-up boundary from the observations of the MAG/ER experiment onboard Mars Global Surveyor. Geophys. Res. Lett. **27**, 49–52 (2000). doi:10.1029/1999GL010703
D. Vignes, M.H. Acuña, J.E.P. Connerney, D.H. Crider, H. Rème, C. Mazelle, Factors controlling the location of the Bow Shock at Mars. Geophys. Res. Lett. **29**(9), 1328 (2002). doi:10.1029/2001GL014513
M. Volwerk et al., Mirror-mode-like structures in Venus' induced magnetosphere. J. Geophys. Res. **113**(15), E0B016 (2008)
M. Volwerk, M. Delva, Y. Futaana, A. Retinò, Z. Vörös, T.L. Zhang, W. Baumjohann, S. Barabash, Substorm activity in Venus's magnetotail. Ann. Geophys. **27**(6), 2321–2330 (2009)
Z. Vörös et al., Intermittent turbulence, noisy fluctuations, and wavy structures in the Venusian magnetosheath. J. Geophys. Res. **113**(A12), E00B21 (2008)
J.E. Wahlund et al., Cassini measurements of cold plasma in the ionosphere of titan. Science **308**(5724), 986–989 (2005)
H.Y. Wei, C.T. Russell, Proton cyclotron waves at Mars: exosphere structure and evidence for a fast neutral disk. Geophys. Res. Lett. **33**(23), L23103 (2006)
H.Y. Wei et al., Cold ionospheric plasma in Titan's magnetotail. Geophys.Res. Lett. **34**, L24S06 (2007). doi:10.1029/2007GL030701
H.Y. Wei et al., Comparative study of ion cyclotron waves at Mars, Venus and Earth. Planet. Space Sci. **59**(10), 1039–1047 (2011). doi:10.1016/j.pss.2010.01.004
D.A. Wolf, F.M. Neubauer, Titan's highly variable plasma environment. J. Geophys. Res. **87**, 881–885 (1982)
Y. Yeroshenko et al., The magnetotail of Mars—PHOBOS observations. Geophys. Res. Lett. **17**, 885–888 (1990)
D.T. Young et al., Cassini plasma spectrometer investigation. Space Sci. Rev. **114**, 1–112 (2004)
L.M. Zelenyi, O.L. Vaisberg, Venusian interaction with the solar wind plasma flow as a limiting case of the cometary type interaction, in *Advances of Space Plasma Physics*, ed. by B. Buti (World Scientific, Singapore, 1985), pp. 59–76
T.-L. Zhang, J.G. Luhmann, C.T. Russell, The solar cycle dependence of the location and shape of the Venus bow shock. J. Geophys. Res. **95**, 14961–14967 (1990)
T.L. Zhang, J.G. Luhmann, C.T. Russell, The magnetic barrier at Venus. J. Geophys. Res. **96**(11), 11145–11153 (1991)
T.-L. Zhang et al., The flaring of the Martian magnetotail observed by the PHOBOS 2 spacecraft. Geophys. Res. Lett. **21**(12), 1121–1124 (1994)
T.L. Zhang, K.K. Khurana, C.T. Russell, M.G. Kivelson, R. Nakamura, W. Baumjohann, On the Venus bow shock compressibility. Adv. Space Res. **33**, 1920–1923 (2004)
T.L. Zhang et al., Magnetic field investigation of the Venus plasma environment: expected new results from Venus Express. Planet. Space Sci. **54**, 1336–1343 (2006)
T.L. Zhang et al., Initial Venus Express magnetic field observations of the Venus bow shock location at solar minimum. Planet. Space Sci. **56**, 785–789 (2008a)
T.L. Zhang et al., Induced magnetosphere and its outer boundary at Venus. J. Geophys. Res. **113**, E00B20 (2008b). doi:10.1029/2008JE003215
T.L. Zhang et al., Disappearing induced magnetosphere at Venus: Implications for close-in exoplanets. Geophys. Res. Lett. **36**(20), L20203 (2009)
T.L. Zhang, W. Baumjohann, J. Du, R. Nakamura, R. Jarvinen, E. Kallio, A.M. Du, M. Balikhin, J.G. Luhmann, C.T. Russell, Hemispheric asymmetry of the magnetic field wrapping pattern in the Venusian magnetotail. Geophys. Res. Lett. **37**(14), L14202 (2010)
B.J. Zwan, R.A. Wolf, Depletion of solar wind plasma near a planetary boundary. J. Geophys. Res. **81**, 1636–1648 (1976)